



## 저작자표시-비영리-변경금지 2.0 대한민국

이용자는 아래의 조건을 따르는 경우에 한하여 자유롭게

- 이 저작물을 복제, 배포, 전송, 전시, 공연 및 방송할 수 있습니다.

다음과 같은 조건을 따라야 합니다:



저작자표시. 귀하는 원저작자를 표시하여야 합니다.



비영리. 귀하는 이 저작물을 영리 목적으로 이용할 수 없습니다.



변경금지. 귀하는 이 저작물을 개작, 변형 또는 가공할 수 없습니다.

- 귀하는, 이 저작물의 재이용이나 배포의 경우, 이 저작물에 적용된 이용허락조건을 명확하게 나타내어야 합니다.
- 저작권자로부터 별도의 허가를 받으면 이러한 조건들은 적용되지 않습니다.

저작권법에 따른 이용자의 권리는 위의 내용에 의하여 영향을 받지 않습니다.

이것은 [이용허락규약\(Legal Code\)](#)을 이해하기 쉽게 요약한 것입니다.

[Disclaimer](#)

공학박사학위논문

오그제틱 패턴의 변형 모드를 이용한  
구조 강성 설계

Designing structural stiffness  
using deformation modes of auxetic patterns

2023년 8월

서울대학교 대학원

기계항공공학부

허 정 민

# 오그제틱 패턴의 변형 모드를 이용한 구조 강성 설계

Designing structural stiffness  
using deformation modes of auxetic patterns

지도교수 김 도 년

이 논문을 공학박사 학위논문으로 제출함

2023년 4월

서울대학교 대학원

기계항공공학부

허 정 민

허정민의 공학박사 학위논문을 인준함

2023년 6월

위 원 장 : 김 윤 영 (인)

부위원장 : 김 도 년 (인)

위 원 : 양 진 규 (인)

위 원 : 이 호 원 (인)

위 원 : 노 건 우 (인)

# Abstract

Auxetic metamaterials have garnered great interests of researchers due to their counter-intuitive property, a negative Poisson's ratio. When an auxetic material is tensioned, the entire volume expands, whereas a conventional material contracts along its sides. This unique characteristic of auxetic metamaterial arises from auxetic deformation, where void spaces in unit cells expand under tension. When subjected to shear load, however, the materials undergo non-auxetic deformation mode that is similar to that of continuum. We focused on these distinct deformation modes of auxetic metamaterials to control two mechanical properties. A tension-related property would be adjusted by the auxetic deformation mode, whereas the other shear-dominant property could be controlled by the non-auxetic deformation mode.

For the rotating rigid auxetic unit, we presented a design principle to simultaneously control in-plane tensile and shear stiffness of the auxetic pattern by analyzing the deformation mechanisms. The key design variables are the hinge thickness ratio (HR) and the aspect ratio (AR). They play different roles depending on the applied load, which enables simultaneous design of the two stiffnesses.

Based on the design principle, we developed two additional design principles for meta-structures, auxetic meta-tube and auxetic meta-disk. The auxetic meta-tube was designed to be able to adjust bending and torsional stiffness of tubular structure. The numerical and experimental results confirm that the tube stiffness values can be independently controlled in a wide area. It can be used to improve the stability and performance of a concentric tube robot for minimal invasive surgery. The auxetic meta-disk is capable of simultaneous design of the flexural and torsional natural frequencies of disk structures, which is crucial in manipulating elastic wave propagation. Comprehensive finite element analyses verified that the wave propagation in pipes could be controlled over a broadband frequency range. An elastic wave mode filter was suggested as an application, which may be useful in non-destructive testing.

The contribution of this work lies in its intuitiveness and applicability across various field. The proposed design principles can be easily extended to diverse mechanical properties and geometries, and we expect to enable the design of novel mechanical metamaterials through this approach.

**Keyword:** Metamaterial, Auxetic material, Stiffness, Wave propagation

**Student Number:** 2015-22727

# Table of Contents

Abstract.....	1
Table of Contents.....	2
List of Figures.....	6
List of Tables .....	1 7
<b>Chapter 1. Introduction .....</b>	<b>1 8</b>
1.1. Background.....	1 8
1.2. Key idea.....	2 1
1.3. Objectives .....	2 3
1.4. Research outline .....	2 4
<b>Chapter 2. Simultaneous adjustment of in-plane stiffness of auxetic metamaterials.....</b>	<b>2 6</b>
2.1. Rotating rigid auxetic unit cell .....	2 6
2.1.1. Conversion to slit-type rotating rigid auxetics .....	2 7
2.1.2. Unit cell definition .....	3 0
2.2. Definition of in-plane stiffness .....	3 2
2.3. Deformation mechanism analysis.....	3 4
2.3.1. Auxetic deformation mode under tension .....	3 4
2.3.2. Non-auxetic deformation mode under shear .....	3 8
2.4. Finite element analysis .....	4 1
2.5. Design principle for simultaneous control of in-plane stiffness.....	4 3
2.5.1. In-plane tensile stiffness control.....	4 3
2.5.2. In-plane shear stiffness control.....	4 6
2.5.3. Results of tilted rotating rigid auxetic pattern .....	5 0

2.6. Conclusion .....	5	5
-----------------------	---	---

### **Chapter 3. Simultaneous adjustment of tube stiffness: Auxetic meta-tube**

.....	5	6
3.1. Introduction .....	5	6
3.2. Auxetic meta-tube.....	5	8
3.2.1. Definition of auxetic meta-tube.....	5	8
3.2.2. Study for other design variables.....	6	0
3.3. Finite element analysis .....	6	2
3.3.1. Analysis model .....	6	2
3.3.2. Definition of tube stiffness .....	6	3
3.3.3. Convergence test .....	6	3
3.4. Experimental verification .....	6	5
3.4.1. Fabrication.....	6	5
3.4.2. Modal testing.....	6	6
3.5. Design principle for simultaneous control of stiffness of auxetic meta-tube .....	6	9
3.5.1. Bending stiffness (B) control .....	6	9
3.5.2. Torsional stiffness (C) control.....	7	0
3.5.3. Designable stiffness area .....	7	2
3.5.4. Independent stiffness control.....	7	3
3.6. Results with triangular and hexa-triangular pattern .....	7	5
3.6.1. Definition of triangular and hexa-triangular unit cell.....	7	5
3.6.2. Stiffness control result.....	7	7
3.7. Results with tilted rectangular patterns .....	8	0
3.8. Conclusion .....	8	4

## Chapter 4. Simultaneous control of elastic wave propagation: Auxetic

<b>meta-disk .....</b>	<b>8 5</b>
4.1. Introduction .....	8 5
4.2. Auxetic meta-disk .....	8 8
4.2.1. Definition of auxetic meta-disk.....	8 8
4.2.2. Study for other design variables.....	9 0
4.3. Finite element analysis model .....	9 1
4.3.1. Analysis model .....	9 1
4.3.2. Normal mode analysis .....	9 1
4.3.3. Validity of sector model .....	9 2
4.3.4. Dispersion analysis.....	9 3
4.3.5. Transmission analysis.....	9 6
4.3.6. Mesh convergence test .....	9 7
4.3.7. Mesh for perfectly matched layers .....	9 8
4.4. Design principle for simultaneous control of elastic wave propagation	1 0 0
4.4.1. Flexural mode natural frequency control .....	1 0 0
4.4.2. Torsional mode natural frequency control.....	1 0 1
4.4.3. Effect of mass variation of auxetic meta-disk .....	1 0 3
4.4.4. Bandgap formation.....	1 0 3
4.4.5. Designable range of bandgaps.....	1 0 5
4.5. Numerical validation .....	1 0 9
4.5.1. Transmission analysis result.....	1 0 9
4.5.2. Investigation of attenuation efficiency .....	1 1 0
4.6. Application: Elastic wave mode filter .....	1 1 3
4.7. Conclusion .....	1 1 5

<b>Chapter 5. Concluding remarks.....</b>	<b>1 1 6</b>
Appendix. ....	1 1 7
Bibliography .....	1 3 2
Abstract in Korean.....	1 3 5



## List of Figures

Figure 1-1. Deformed configuration of materials subjected to tensile load. (a) Positive Poisson's ratio, and (b) negative Poisson's ratio.

Figure 1-2. Auxetic deformation modes of three representative auxetic patterns. Deformed configurations of (a) reentrant, (b) rotating rigid unit, and (c) chiral auxetic patterns are shown under tensile loading. In auxetic deformation mode, the internal void space expands when subjected to tensile load to exhibit a negative Poisson's ratio.

Figure 1-3. Non-auxetic deformation mode of three representative auxetic patterns. Deformed configurations of (a) reentrant, (b) rotating rigid unit, and (c) chiral auxetic patterns are shown under shear loading. The unit cells are deformed similar to a continuum.

Figure 2-1. Auxetic and non-auxetic deformation modes of rotating rigid auxetic patterns. Auxetic deformation modes of (a) rectangular, (b) triangular, and (c) hexa-triangular patterns and non-auxetic deformation modes of (d) rectangular, (e) triangular, and (f) hexa-triangular patterns are shown.

Figure 2-2. Point hinge and slit-pattern auxetics. The hinges are applied by a certain width by perforating narrow slit holes.

Figure 2-3. Auxetic deformation of slit-pattern auxetics. The auxetic deformation mode is sustained in the slit-pattern auxetics, where the rectangles rotate alternatively due to their geometrical connectivity under tension.

Figure 2-4. Non-auxetic deformation of slit-pattern auxetics. The deformed configuration confirms that the non-auxetic deformation mode of the point hinge auxetics remains. A continuum-like shear deformation appear in both point hinge pattern and slit-pattern auxetics.

Figure 2-5. Definition of slit-pattern auxetic unit cell. Four subunits consist in a auxetic unit cell, and each subunits are defined by two design variables, HR and AR. Slit thickness ratio is constant in this study as 0.1. The slit thickness is uniform so that the changes in the design variables do not affect the slit thickness.

Figure 2-6. Unit cell variation with changing design variables. (a) HR variation, and (b) AR variation. The unit length ( $w$ ) is set as constant, so AR affects only its height.

Figure 2-7. Definition of in-plane stiffness. (a) Tensile and (b) shear stiffness. In tensile case, the bottom edge is constrained and normal displacements are applied at the top of the material. In shear case, the outer edges are subjected to a shear displacement to represent pure shear deformation.

Figure 2-8. Mechanism of auxetic and non-auxetic deformation modes of rotating rigid auxetic pattern. (a) Auxetic deformation mode, and (b) non-auxetic deformation mode. In the auxetic deformation mode, the rectangles rotate in the opposite direction with the adjacent rectangles, and in the non-auxetic deformation mode, the rectangles do not rotate but themselves deform.

Figure 2-9. Schematics and unit cell shape according to the variation in HR in auxetic deformation mode. As HR increases, the rotational hinges become stiff. Example unit cell designs of (a)  $HR = 0.3$ , (b)  $HR = 0.5$ , and (c)  $HR = 0.7$  are shown.

Figure 2-10. Illustration of relation between aspect ratio AR and rotation angle  $\theta$ . Left figure represents the variables when the unit cell rotates. Each curve in the right figure shows the relations of AR and  $\theta$ .  $AR^*$  located on the lateral axis is an example of the limit aspect ratio of unit cell to generate specific elongation rate.

Figure 2-11. Schematics and unit cell shape according to the variation in AR in auxetic deformation mode. As AR increases, larger rotation angle is required to reach a certain displacement. Example unit cell designs of (a)  $AR = 2^{-1}$ , (b)  $AR = 2^0$ , and (c)  $AR = 2^1$  are shown.

Figure 2-12. Schematics and unit cell shape according to the variation in HR in non-auxetic deformation mode. HR represents the length of connectors rather than rotational rigidity. Example unit cell designs of (a)  $HR = 0.3$ , (b)  $HR = 0.5$ , and (c)  $HR = 0.7$  are shown

Figure 2-13. Deformed shapes with the variation in AR. (a) As AR increases, the overall deformed shape of the unit cells becomes bending-like

configuration, which is flexible than pure shear deformation. (b) Clear difference of the side edges of the unit cells is observed in the scale-down configurations.

Figure 2-14. Schematics and unit cell shape according to the variation in AR in non-auxetic deformation mode. AR determines the deformed shape of subunits. As AR value is apart from  $2^0$  further, subunits experience beam-like flexural shear deformation. Example unit cell designs of (a)  $AR = 2^{-2}$ , (b)  $AR = 2^{-1}$ , and (c)  $AR = 2^0$  are shown.

Figure 2-15. Mesh convergence test. (a) Strain energy graph as a function of the minimum mesh size ratio. (b) Mesh resolution. The minimum mesh ratio of 0.01 was enough for a converged solution.

Figure 2-16. In-plane tensile stiffness adjustment by changing HR. Each curve corresponds to a constant AR value. The lateral and vertical axes represent the design variable HR and the normalized tensile stiffness, respectively. As HR increases, higher rigidity of rotational hinges is assumed, therefore the tensile stiffness increases.

Figure 2-17. Schematics and normal stress distribution with the change in HR. Relative normal stress distribution in the y-direction is plotted next to schematic figure. (a)  $HR = 0.1$ , (b)  $HR = 0.3$ , and (c)  $HR = 0.5$ . The color map is ranged from blue for a negative stress, and to red for a positive stress.

Figure 2-18. In-plane tensile stiffness adjustment by changing AR. Each curve corresponds to a constant HR value. As AR increases, larger rotational angle is required, therefore the tensile stiffness increases.

Figure 2-19. Schematics and normal stress distribution with the change in AR. Relative normal stress distribution in the y-direction is plotted next to schematic figure. (a)  $AR = 2^{-2}$ , (b)  $AR = 2^{-1}$ , and (c)  $AR = 2^0$ . The color map is ranged from blue for a negative stress, and to red for a positive stress.

Figure 2-20. In-plane shear stiffness adjustment by changing HR. Each curve corresponds to a constant AR value. As HR increases, longer connector width occupies, therefore the shear stiffness increases.

Figure 2-21. Schematics and shear stress distribution with the change in HR. Relative shear stress distribution is plotted next to schematic figure. (a)  $HR = 0.1$ , (b)  $HR = 0.3$ , and (c)  $HR = 0.5$ . The color map is ranged from blue for a negative stress, and to red for a positive stress.

Figure 2-22. In-plane tensile stiffness adjustment by changing AR. Each curve corresponds to a constant HR value. As AR value is closer to  $2^0$ , shear-dominant deformation appears resulting a higher shear stiffness.

Figure 2-23. Schematics and shear stress distribution with the change in AR. Relative shear stress distribution is plotted next to schematic figure. (a)  $AR = 2^{-2}$ , (b)  $AR = 2^{-1}$ , and (c)  $AR = 2^0$ . The color map is ranged from blue for a negative stress, and to red for a positive stress.

Figure 2-24. 45-degree rectangular pattern. (a) The original pattern. (b) 45-degree rectangular pattern.

Figure 2-25. Force state of 45-degree pattern under tension. (a) In the original coordinate. (b) In the rotated coordinate.

Figure 2-26. Force state of 45-degree pattern under shear. (a) In the original coordinate. (b) In the rotated coordinate.

Figure 2-27. In-plane tensile stiffness adjustment of 45-degree pattern. The tensile stiffness adjustment according to the variation of (a) HR and (b) AR, and the shear stiffness adjustment according to the variation of (c) HR and (d) AR.

Figure 2-28. Explanation of shear stiffness variation of 45-degree pattern. The variation of the normal stiffness in (a) y-direction and (b) x-direction of the original pattern. (c) the variation of  $C_{33}$  component of elasticity matrix of the tilted patterns.

Figure 2-29. Explanation of tensile stiffness variation of 45-degree pattern. (a) The variation of the averaged normal stiffness, (b) the shear stiffness variation of the original pattern, and (c) the variation of  $C_{22}$  component of elasticity matrix of the tilted patterns.

Figure 3-1. Loading status of cross-section of auxetic meta-tube. The deformed configuration of auxetic meta-tubes and the loading status of the cross-

section are present for (a) bending, and (b) torsional deformation.

Figure 3-2. Consisting of auxetic meta-disk. Six auxetic unit cell is arranged in the circumferential direction to build a auxetic unit layer, and the layers are stacked axially to form an auxetic meta-tube.

Figure 3-3. Various examples of auxetic meta-tube.

Figure 3-4. Convergence test on the number of unit cell in circumferential direction,  $n$ . The lateral axes represent  $n$ , which is double of the value of the number of the unit cells.  $n$  of 12 (six unit cells) was enough to minimize the curvature effect of the auxetic meta-tube.

Figure 3-5. Convergence test on the number of unit cell layers,  $m$ . The lateral axis represent  $m$ , which is double of the value of the number of the unit layers.  $m$  of 80 (40 unit layers) for 1 m length tube was enough to ignore the boundary effect in the case of AR equal to  $2^0$ .

Figure 3-6. Analysis model of auxetic meta-disk. (a) Tie constraint connecting the master node and the top edges, (b) mesh resolution, and (c) six-node shell element. The bottom edges of the meta-tube were fixed, and small prescribed bending and torsional rotations are applied at the master node.

Figure 3-7. Convergence test on the mesh size with varying the maximum element size. The left figure represents stiffness value convergence and the right figure shows the stiffness difference between the mesh sizes. 0.08 for the minimum mesh size was enough for a converged solution.

Figure 3-8. Auxetic meta-tube specimens. The auxetic meta-tubes are fabricated by high-resolution laser cutting.

Figure 3-9. Bending modal test. An auxetic tube specimen is hung by two free-end hooks to produce free-end boundary condition. An accelerometer located at the center of the tube measures the responses produced by an impact hammer.

Figure 3-10. Torsional modal test. The specimen is placed on two supports located at the end of the tube. Two magnetostrictive patch transducers are installed at one-third and two-thirds points along the tube length, one of which generates torsional impact pulses and the other one measures responses.

Figure 3-11. Adjustment of bending stiffness of auxetic meta-tube. Each curve represents a constant the other design variable. (a) HR variations, and (b) AR variations. X-markers denote the experimental results, and the color curve indicate the corresponding numerical results.

Figure 3-12. Schematics and normal stress distribution with the change in design variables. (a) HR variations, and (b) AR variations. High level of stress occurs in the large HR unit cell and in the large AR unit cell.

Figure 3-13. Adjustment of torsional stiffness of auxetic meta-tube. Each curve represents a constant the other design variable. (a) HR variations, and (b) AR variations. X-markers denote the experimental results, and the color curve indicate the corresponding numerical results.

Figure 3-14. Schematics and shear stress distribution with the change in design variables. (a) HR variations, and (b) AR variations. High level of stress occurs in the large HR unit cell and in the unit cell of AR equal to  $2^0$ .

Figure 3-15. Designable tube stiffness area. Solid and dotted lines represent the constant HR and AR values, respectively. A wide designable stiffness area is achieved.

Figure 3-16. Independent torsional stiffness control. (a) Bending stiffness contour, and (b) the examples of meta-tube designs, where the bending stiffness values are constant but the torsional stiffness values vary.

Figure 3-17. Independent bending stiffness control. (a) Torsional stiffness contour, and (b) the examples of meta-tube designs, where the torsional stiffness values are constant but the bending stiffness values vary.

Figure 3-18. Triangular and hexa-triangular rotating rigid unit cell. Eight triangular subunits compose (a) triangular unit cell, and two triangular and one hexagonal subunits constitute (b) hexa-triangular unit cell. Two design variables, HR and AR, define the unit cells. In both figures, the unit length was assumed to be 1 for simplicity.

Figure 3-19. Independent torsional stiffness control with triangular pattern. (a) Bending stiffness contour, and (b) the examples of triangular pattern meta-tube designs.

Figure 3-20. Independent bending stiffness control with triangular pattern. (a)

Torsional stiffness contour, and (b) the examples of triangular pattern meta-tube designs.

Figure 3-21. Independent torsional stiffness control with hexa-triangular pattern. (a) Bending stiffness contour, and (b) the examples of hexa-triangular pattern meta-tube designs.

Figure 3-22. Independent bending stiffness control with hexa-triangular pattern. (a) Torsional stiffness contour, and (b) the examples of hexa-triangular pattern meta-tube designs.

Figure 3-23. Construction of auxetic meta-tube with tilted auxetic unit cell.

Figure 3-24. Uncontinuity of hinges.

Figure 3-25. Auxetic meta-tube with 45-degree pattern. (a)  $AR = 2^{-1}$ , (b)  $AR = 2^0$ , and (c)  $AR = 2^1$ .

Figure 3-26. Normalized bending and torsional stiffness adjustment of 45-degree pattern. The bending stiffness adjustment according to the variation of (a) HR and (b) AR, and the torsional stiffness adjustment according to the variation of (c) HR and (d) AR.

Figure 4-1. Utilizing load-dependent deformation modes in vibration of disk structure. The displacement fields of the flexural and torsional mode shapes of a disk structure are illustrated with quivers. Each colored square in the mode shapes denotes the unit cell showing its deformation type.

Figure 4-2. Auxetic meta-disk composition. Two auxetic unit cell form a unit sector, which is arranged circumferentially to establish an auxetic meta-disk. The auxetic meta-disks are placed on a host pipe to form the entire meta-structure.

Figure 4-3. Definition of auxetic meta-disk. (a) Dimensions for the definition, the unit cell variation by the change in (b) AR, and (c) HR. Note that the height of a subunit ( $h$ ) is set constant, so the circumferential length of the unit cell decreases as AR increases.

Figure 4-4. FE model for normal mode analysis. (a) Finite element model of the auxetic meta-disk sector, (b) ten-node tetrahedral element, and (c)

resolution of the mesh. At the red-colored faces in both sides, cyclic symmetry condition is applied, and the inner faces are constrained.

Figure 4-5. Mode shapes and natural frequency comparison between the full disk model and the sector disk model. The normalized total displacement distribution is plotted. The natural frequencies of the full and the sector models are almost coincident which ensures the validity of the usage of the sector model.

Figure 4-6. FE model for dispersion analysis. The sector model of auxetic meta-disk is attached on a sector host pipe. Floquet periodic boundary condition for dispersion analysis is applied at the pink-colored faces at the front and the back of the sector pipe.

Figure 4-7. Forming dispersion curves via dispersion analysis. (a) The results of dispersion analysis are obtained as eigenfrequencies and corresponding mode shapes for a given wavenumber. (b) The points whose mode is the same are connected to draw dispersion curves.

Figure 4-8. Calculated mode shapes for an example wavenumber,  $0.2 \pi$  (rad/m). Each point which lies vertically is corresponding to each mode. (a) Out-of-phase mode, (b) 2nd torsional mode, (c) 1st flexural mode, (d) out-of-phase mode, (e) and (f) coupled mode. Note that the azimuthal mode number was set as one, so the mode shape of the entire disk has phase variance of  $2 \pi$  along to the circumferential direction.

Figure 4-9. FE model for transmission analysis. From four to twelve auxetic meta-disks with the host pipe are arranged. Waveguides are attached at the front and back of the meta-disk array. At the end of the waveguides, perfectly matched layer (PML) was applied to inhibit reflected wave.

Figure 4-10. Convergence test on the minimum mesh size. The vertical and lateral axis represent the solution (reaction force) and  $1/\gamma$  and corresponding the number of the used elements.

Figure 4-11. Convergence test on the minimum mesh size. The vertical and lateral axis represent the solution (reaction force) and  $1/\gamma$  and corresponding the number of the used elements.

Figure 4-12. Adjustment of flexural natural frequency of auxetic meta-disk. Each



curve represents a constant the other design variable. (a) HR variations, and (b) AR variations. As HR and AR values increase, the flexural natural frequencies increase.

Figure 4-13. Schematics and radial stress distribution with the change in design variables. (a) HR variations, and (b) AR variations. Higher level of stress occurs when HR and AR increase.

Figure 4-14. Adjustment of torsional natural frequency of auxetic meta-disk. Each curve represents a constant the other design variable. (a) HR variations, and (b) AR variations. As HR increase and AR is closer to  $2^0$ , the torsional natural frequencies increase.

Figure 4-15. Schematics and shear stress distribution with the change in design variables. (a) HR variations, and (b) AR variations. Higher level of stress occurs when HR increase or AR is closer to  $2^0$ .

Figure 4-16. Bandgap formation. Band structures for (a) flexural and (b) torsional modes of an example meta-disk ( $AR=2^0$  and  $HR=0.3$ ). The blue and yellow areas correspond to the bandgaps.

Figure 4-17. Mode shapes for the points located in the bandgaps. (a) Flexural, and (b) torsional modes. (iii) is the out-of-phase mode and (iv) is the radial mode which do not affect forming bandgaps.

Figure 4-18. Designable bandgap range. The bandgaps in the two modes are denoted with blue and yellow color bar, respectively. The lower and upper frequencies of each bar represent the bandgap opening and closing frequency. The lateral axis represents the variation of AR and the values of HR are set constant in each subfigure as (a) 0.1, (b) 0.3, (c) 0.5, and (d) 0.7, respectively.

Figure 4-19. Bandgap variation with the changes in the distance of auxetic meta-disks. Band structures are plotted with bandgaps denoted with colored area for (a) flexural and (b) torsional mode. As the distance between the meta-disks increases, the mass ratio is reduced, resulting the bandgap closing frequency goes down.

Figure 4-20. Bandgap comparison between the double distance model and the half thickness model. In the double distance model, the starting and ending

frequency of the bandgaps are (212 Hz, 270 Hz) and (120 Hz, 193 Hz) for flexural and torsional modes, respectively, and in the half thickness model, the bandgap frequencies are (211 Hz, 267 Hz) and (120 Hz, 192 Hz) for flexural and torsional modes, respectively.

Figure 4-21. Wave transmission in bandgaps. (a) Flexural and (b) torsional wave. It was observed that the transmission values were sharply reduced in the bandgaps, especially near the bandgap opening frequency. The out-of-phase or radial mode existing in the bandgap do not significantly reduce the attenuation efficiency.

Figure 4-22. FRF of the different number of meta-disks. (a) Flexural and (b) torsional responses calculated by transmission analysis are plotted. Larger number of the meta-disks produces lower transmission values.

Figure 4-23. Elastic wave mode filtering application. (a) The meta-disk unit cell designs of the samples with the design parameters represented as a set of (AR, HR) and the bandgap formation of the samples are displayed, and (b) the deformed configurations with the normalized displacement distribution are illustrated.

Figure A-1. Frequency Response Functions (FRFs) of the auxetic tubes imposed an impact force. The marked frequencies indicate the first mode bending natural frequencies of the tubes. The vertical axis refers magnitude in decibel unit.

Figure A-2. Frequency Response Functions (FRFs) of the auxetic tubes imposed a torsional impact force. The marked frequencies indicate the first mode torsional natural frequencies of the tubes.

Figure A-3. Normal stress distribution in auxetic tube unit cell under bending load. The sizes of the unit cells are normalized to be the same to the unit cell with  $AR = 2^0$ .

Figure A-4. Normal stress distribution in auxetic tube unit cell under bending load (continued).

Figure A-5. Shear stress distribution in auxetic tube unit cell under torsional load.

Figure A-6 Shear stress distribution in auxetic tube unit cell under torsional load

(continued).

Figure A-7. Frequency comparison between FE static, normal mode analysis and experiment. a) 1<sup>st</sup> bending mode frequencies, and b) 1<sup>st</sup> torsional mode frequencies.

Figure A-8. Feasible stiffness region of rectangular unit auxetic tube. The solid and dashed lines indicate constant AR, and HR respectively.

Figure A-9. Feasible stiffness region of triangular unit auxetic tube.

Figure A-10. Feasible stiffness region of hexa-triangular unit auxetic tube.

## List of Tables

Table 3-1. Comparison of numerical and experimental result of the natural frequencies of auxetic tubes. The subscripts B and T indicate the bending and torsional modes, respectively, and FE and EXP denote the numerical and experimental data, respectively.

Table 3-2. Normalized tube stiffness and stiffness ratio.

Table 4-1. Notated, actual AR values and corresponding the number of the unit cell in circumferential direction,  $n_c$ .

Table 4-2. Minimum and average transmission values in the bandgap. The design parameters are set as AR is equal to  $2^0$  and HR is 0.3.

Table A-1. Normalized bending stiffness of rectangular pattern.

Table A-2. Normalized torsional stiffness of rectangular pattern.

Table A-3. Normalized bending stiffness of triangular pattern.

Table A-4. Normalized torsional stiffness of triangular pattern.

Table A-5. Normalized bending stiffness of hexa-triangular pattern.

Table A-6. Normalized torsional stiffness of hexa-triangular pattern.

Table A-7. Natural frequency and bandgap frequencies of the auxetic disk. HR is constant as 0.1.

Table A-8. Natural frequency and bandgap frequencies of the auxetic disk. HR is constant as 0.3.

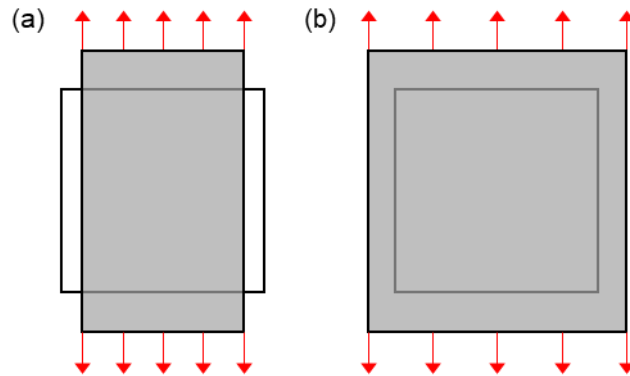
Table A-9. Natural frequency and bandgap frequencies of the auxetic disk. HR is constant as 0.5.

Table A-10. Natural frequency and bandgap frequencies of the auxetic disk. HR is constant as 0.7.

# Chapter 1. Introduction

## 1.1. Background

Auxetic material refers to a metamaterial that has been designed to possess a negative Poisson's ratio. This ratio is defined as the ratio of the displacement perpendicular to an applied force to the displacement in the direction of the force. While typical materials with a positive Poisson's ratio contract in the direction perpendicular to the applied force, auxetic materials with a negative Poisson's ratio expand in all directions, including the perpendicular direction. (Figure 1-1) This unique property of auxetic materials arises from the widening of empty spaces inside the material under tension<sup>1</sup>.



**Figure 1-1. Deformed configuration of materials subjected to tensile load. (a)** Positive Poisson's ratio, and (b) negative Poisson's ratio.

The special properties of auxetic materials have garnered the interest of many researchers. Since the first report of a foam structure with a negative Poisson's ratio<sup>2</sup>, materials with a negative Poisson's ratio have been named "auxetic materials"<sup>3</sup>, and various auxetic materials and fabrication methods have been reported<sup>4-10</sup>. In the scope of metamaterials, much research has been conducted to design auxetic unit

cell which are artificially designed to have a negative Poisson's ratio. Representative auxetic unit cells of auxetic materials include reentrant, rotating rigid unit, and chiral structures, each with a different deformation mechanism under tensile loading as shown in Figure 1-2. For the reentrant structures, thin ribs are unfolded. Masters and Evans predicted elastic constants of reentrant honeycombs<sup>11</sup>, Theocaris et al. analytically investigated negative Poisson's ratio of star-shaped reentrants<sup>12</sup>, and Smith et al. introduced reentrant model to explain a negative Poisson's ratio of auxetic foams<sup>13</sup>. The rotating rigid units show polygonal unit cells rotating alternatively by point hinges. Grima et al. proposed analytical models of rotating rigid units for squares<sup>14</sup>, rectangles<sup>15</sup>, and triangles<sup>16</sup>, and a semi-rigid rotating unit was proposed by Grima<sup>17</sup>. Chiral structures have ligaments attached at cores, which bent under tensile load. Prall et al. proposed two dimensionally chiral honeycomb having a Poisson's ratio of -1 in a wide strain range<sup>18</sup>, Grima et al. presented tetra-chiral structure that has a negative Poisson's ratio and investigated the variation of Poisson's ratio while adjusting the unit cell design<sup>19</sup>, and Spadoni et al. analytically investigated elasto-static micropolar behavior of a chiral structure<sup>20</sup>.

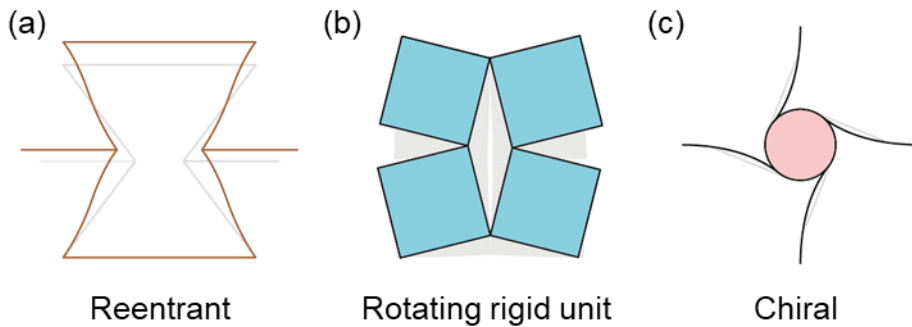


**Figure 1-2. Auxetic deformation modes of three representative auxetic patterns.** Deformed configurations of (a) reentrant, (b) rotating rigid unit, and (c) chiral auxetic patterns are shown under tensile loading. In auxetic deformation mode, the internal void space expands when subjected to tensile load to exhibit a negative Poisson's ratio.

The utilization of the auxetic deformation mode to enhance various material properties has been explored in numerous applications. Analytical and numerical simulations of truss-like structures were carried out by Scarpa et al., investigating their mechanical properties in the context of structural stiffness adjustment<sup>21</sup>. Fu et al. put forward the concept of a reinforced reentrant unit cell with a rhombic honeycomb insert<sup>22</sup>, and Ren et al. developed metallic auxetic tubes with adjustable mechanical and buckling properties<sup>23</sup>. Rossiter et al. employed a shape memory polymer in auxetic structures to regulate their stiffness<sup>24</sup>, while Zhu et al. utilized composite materials for similar purposes<sup>25</sup>. A proposition for hierarchical auxetic meta-structures to reinforce the stiffness of auxetic lattices was made by Rayneau-Kirkhope et al<sup>26</sup>.

In terms of modulating dynamic characteristics, Javid et al. suggested the use of rotating rigid auxetic metamaterials with minimal porosity for vibration control, a concept which was experimentally verified<sup>27</sup>. A numerical study by Imbalzano et al. on the blast loading of an auxetic composite panel showed a reduction in impact energy by up to 70% in comparison to a monolithic panel<sup>28</sup>. Scarpa proposed a reentrant sandwich panel that demonstrated enhanced dynamic performance<sup>29</sup>.

Auxetic deformation mode has also been employed to regulate wave propagation. Liu et al. put forward a chiral meta-composite that exhibited a low-frequency bandgap<sup>30</sup>, while Deng et al. created a rotating rigid auxetic structure with copper inclusions to achieve non-dispersive elastic wave propagation<sup>31</sup>. Tee et al. proposed tetra-chiral auxetic structures with the ability to adjust the formation of bandgaps<sup>32</sup>.

## 1.2. Key idea

Auxetic metamaterials have been designed to exhibit specific behaviors under tensile and compressive loads. They are extensively researched as a means of controlling structural rigidity using these specific behaviors. However, in many practical applications, besides tensile and compressive loads, shear deformation due to shear loads is also often required to be considered. Objects such as airplane airfoils, car suspensions, and robot arms are subjected to a combination of loads, including tension, compression, shear, bending, and twisting. Therefore, the consideration of the shear stiffness of auxetic metamaterials is an essential part of their design.

While auxetic units are not designed to be deformed by shear loads, non-auxetic deformation similar to that of the continuum occurs during shear. For example, the auxetic deformation of the rotating rigid unit during tension is that the polygon of the unit is rigidly rotated to widen the internal space. However, during shear, the unit itself is deformed similar to the continuum, rather than undergoing auxetic deformation as shown in Figure 1-3. This deformation mode of the auxetic pattern shows load-dependent behavior in which the deformation mode varies depending on the direction of the load.

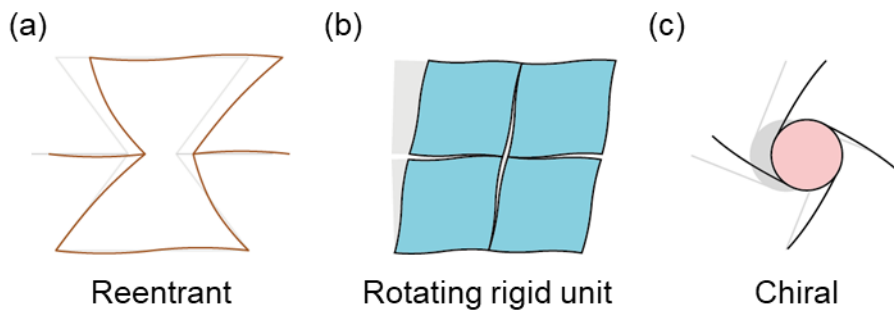


**Figure 1-3. Non-auxetic deformation mode of three representative auxetic patterns.** Deformed configurations of (a) reentrant, (b) rotating rigid unit, and (c) chiral auxetic patterns are shown under shear loading. The unit cells are deformed similar to a continuum.



Utilizing this feature, the mechanical properties of auxetic metamaterials in both directions can be adjusted simultaneously using each deformation mode. Thus, the deformation mode of the auxetic pattern may play a crucial role in controlling the mechanical properties of auxetic metamaterials under combined loads. The consideration of the shear stiffness and load-dependent behavior of auxetic metamaterials may be crucial for their practical application in various fields.

### 1.3. Objectives

In this study, the first objective is to derive a design principle that allows the simultaneous control of the mechanical properties in two directions of a structure using the load-dependent deformation mode of auxetic patterns. Two key design variables, HR and AR, were defined for the rotating rigid unit cell, taking into consideration the auxetic deformation. The deformation mechanism of the unit cell under tensile and shear load were investigated for adjustment of the stiffness.

The second objective of this study is to design two meta-structures, auxetic meta-tubes and auxetic meta-disks, that can solve actual engineering problems based on the design methodology for independent control of mechanical properties. The auxetic meta-tube is made by perforating the surface of a tube with auxetic patterns, which allows for simultaneous control of its bending and torsional stiffness. The bending and torsional stiffness of the tube are known to play a crucial role in the stability and performance of concentric tube robots used in minimally invasive surgery. The auxetic meta-disk is a disk-shaped structure with holes in the axial direction of the auxetic pattern, allowing for simultaneous control of the natural frequencies of its flexural and torsional modes. It functions as a local resonator by being attached a host structure to form a bandgap which is a frequency range where wave cannot propagate. Independent adjustment of natural frequencies in the two modes enables to control the wave propagation in each mode, therefore, the meta-disk can selectively control the transmission of elastic waves depending on the mode that excites in the host structure, functioning as a filter.

## 1.4. Research outline

In Chapter 2, we propose the design principle of rotating rigid auxetic pattern for simultaneous control of its in-plane tensile and shear stiffness. We investigate the load-dependent deformation characteristics of the rotating rigid pattern, and suggest the definition of the slit-type auxetic unit cell. The auxetic and non-auxetic deformation modes are analyzed, and the design principle of the auxetic unit cell was proposed for each mode. We performed finite element analysis to validate the feasibility of the idea, and the results confirmed wide controllability of the two in-plane stiffness values.

In Chapter 3, the load-dependent deformation modes of auxetic pattern is utilized to simultaneously adjust bending and torsional stiffness of tubular structure. The necessity of controlling tube stiffness for biomedical devices is present. We suggest auxetic meta-tube which is composed by perforating auxetic pattern onto tube surface. Finite element analysis and modal test were employed to verify the concept, and a wide designable stiffness area was obtained and the design principle for independent tube stiffness control was presented. The generality of this design concept is demonstrated with additional tube designs utilizing other rotating rigid units.

In Chapter 4, the concept of using load-dependent deformation modes is applied to manipulate elastic wave propagating in pipes. With the limitation of the existing previous research, we propose auxetic meta-disk which behaves as a local resonator on a pipe and enables to simultaneously control propagation of the elastic wave in flexural and torsional wave by generating forbidden bands, bandgaps. Background theory is present to understand the physics of wave propagation in a pipe with local resonators. The definition of the unit cell of the auxetic meta-disk is present, and the design principle to adjust the wave propagation characteristics is suggested. Finite element analysis result shows that the two wave modes can be effectively manipulated to be propagated or to be blocked. The factor to affect attenuation efficiency in a bandgap was also investigated. For a practical application, we suggest

an elastic wave mode filter and some examples are demonstrated.

## **Chapter 2. Simultaneous adjustment of in-plane stiffness of auxetic metamaterials**

### **2.1. Rotating rigid auxetic unit cell**

The auxetic deformation mode of auxetic patterns is designed to arise under tensile load. When an auxetic pattern is subjected to shear load, non-auxetic deformation mode which is similar to the behavior of continuum appear. Three representative auxetic patterns - reentrant, rotating rigid unit, and chiral - exhibit auxetic and non-auxetic deformations, as shown in Figures 1-2 and 1-3. Among them, the rotating rigid unit undergoes rigid body rotation of polygonal subunits due to hinge connectivity in auxetic deformation, while in non-auxetic deformation, the polygon itself deforms rather than the rigid body rotating. The other two patterns are connected by thin ligaments, which pose difficulties in achieving high stiffness or practical fabrication. However, the rotating rigid unit, with its interconnected polygons with areas, offers the advantage of achieving relatively high stiffness and ease of fabrication.

The hinges connecting the polygons of the unit cell are basically point hinges, but the unit cell shape can be modified by applying a certain width to create a slit-type auxetic pattern. In this case, auxetic pattern formation is possible by machining thin slit-shaped holes. Therefore, this study sets the rotating rigid unit as the basic auxetic unit cell. Rotating rigid units are formed by connecting the same or two or more types of polygons via hinges, and various auxetic patterns exist depending on the type of polygon. Figure 2-1 displays the auxetic and non-auxetic deformation modes of rectangular, triangular, and hexa-triangular patterns.

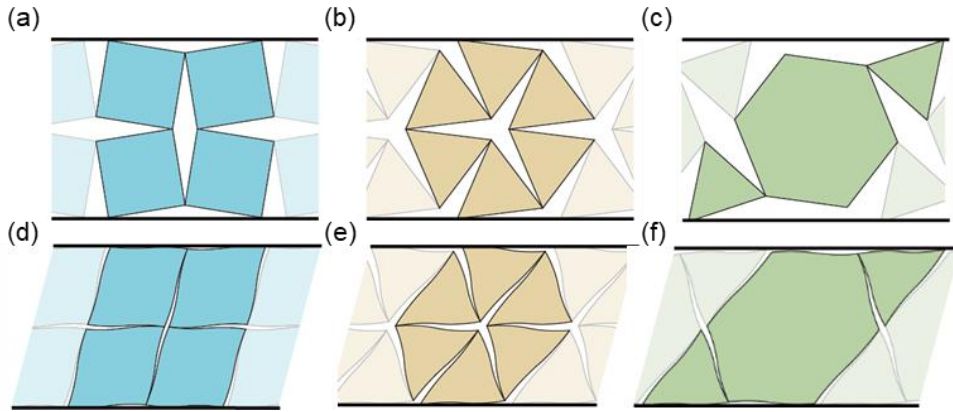


**Figure 2-1. Auxetic and non-auxetic deformation modes of rotating rigid auxetic patterns.** Auxetic deformation modes of (a) rectangular, (b) triangular, and (c) hexa-triangular patterns and non-auxetic deformation modes of (d) rectangular, (e) triangular, and (f) hexa-triangular patterns are shown.

### 2.1.1. Conversion to slit-type rotating rigid auxetics

The basic auxetic pattern consists of point hinges, which can be challenging to implement. Therefore, in this study, a certain width is applied to the hinge portion, and the space between the polygons is assumed to be a thin slit shape, utilizing slit pattern auxetics (Figure 2-2). The shape of the space between the polygons can be determined in various forms, including the slit shape hole used in this study, elliptical shape<sup>33</sup>, and peanut shape<sup>34</sup>. The slit shape hole has a lower porosity compared to other patterns, allowing for relatively higher stiffness. Additionally, its simple form and reduced cutting amount during drilling make fabrication relatively easier.

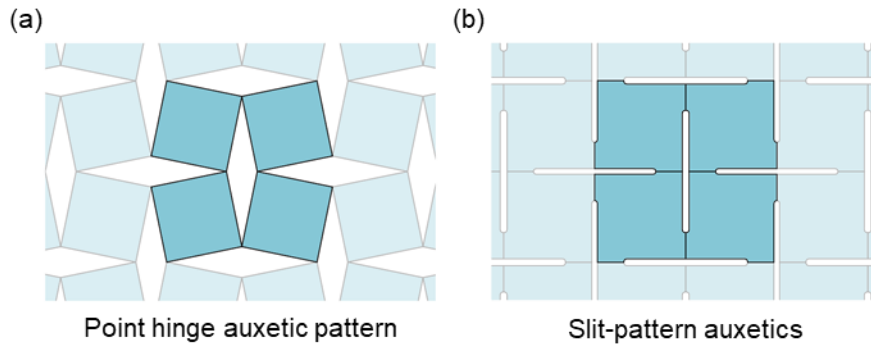


**Figure 2-2. Point hinge and slit-pattern auxetics.** The hinges are applied by a certain width by perforating narrow slit holes.

The auxetic and non-auxetic deformation shapes of point hinge auxetics and slit-type auxetics are shown in Figures 2-3 and 2-4 below. It can be observed that the auxetic deformation mode, in which the polygon units rotate rigid-like around the hinge, is also present in slit pattern auxetics. In the non-auxetic deformation mode, the deformation of the polygons themselves can also be seen, similar to point hinge auxetics. Thus, it can be confirmed that the load-dependent deformation mode of auxetic patterns remain valid in the slit pattern auxetics.

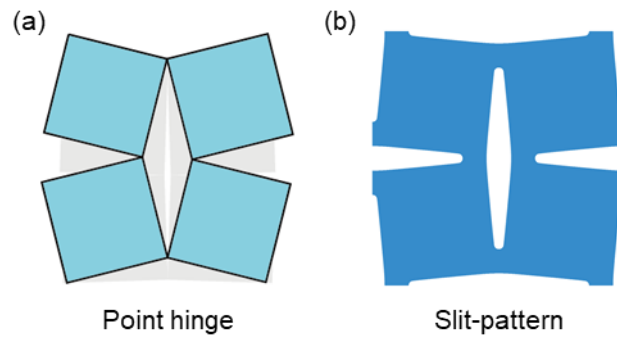


**Figure 2-3. Auxetic deformation of slit-pattern auxetics.** The auxetic deformation mode is sustained in the slit-pattern auxetics, where the rectangles rotate alternatively due to their geometrical connectivity under tension.

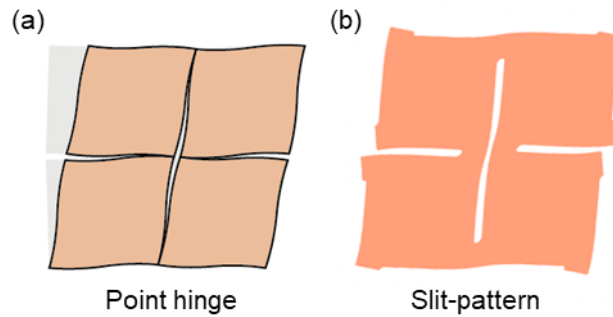


**Figure 2-4. Non-auxetic deformation of slit-pattern auxetics.** The deformed configuration confirms that the non-auxetic deformation mode of the point hinge auxetics remains. A continuum-like shear deformation appear in both point hinge pattern and slit-pattern auxetics.



### 2.1.2. Unit cell definition

Considering the behavior of the unit cell during auxetic deformation, two key design variables, HR (hinge thickness ratio) and AR (aspect ratio), were defined as shown in Figure 2-5. During auxetic deformation, the rectangles within the unit cell rotate due to the rotational hinge, and the rotational rigidity of this hinge plays a crucial role in determining the stiffness of the auxetic deformation mode. The design variable HR is defined as  $t_w/w$  or  $t_h/h$ , and as this value increases, the thickness of the hinge increases, leading to an increase in rotational rigidity. The definition of design variable HR and the changes in the unit cell shape due to variations in HR are shown in Figure 2-6a.

The rotation angle of the rectangles within the unit cell will also determine the stiffness of the auxetic deformation mode. Even if two arbitrary unit cells have the same rotational rigidity, their stiffness will be proportional to the difference in rotation angles required to reach a certain displacement depending on the rectangle shape. The design variable AR determines the shape of the rectangle and is defined as  $h/w$ . The definition of AR and the changes in the unit cell shape due to variations in AR are shown in Figure 2-6b.

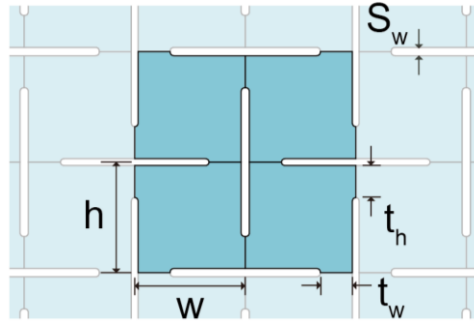


**Figure 2-5. Definition of slit-pattern auxetic unit cell.** Four subunits consist in a auxetic unit cell, and each subunits are defined by two design variables, HR and AR. Slit thickness ratio is constant in this study as 0.1. The slit thickness is uniform so that the changes in the design variables do not affect the slit thickness.

$$AR = \frac{h}{w} \quad (1)$$

$$HR = \frac{t_w}{w} = \frac{t_h}{h} \quad (2)$$

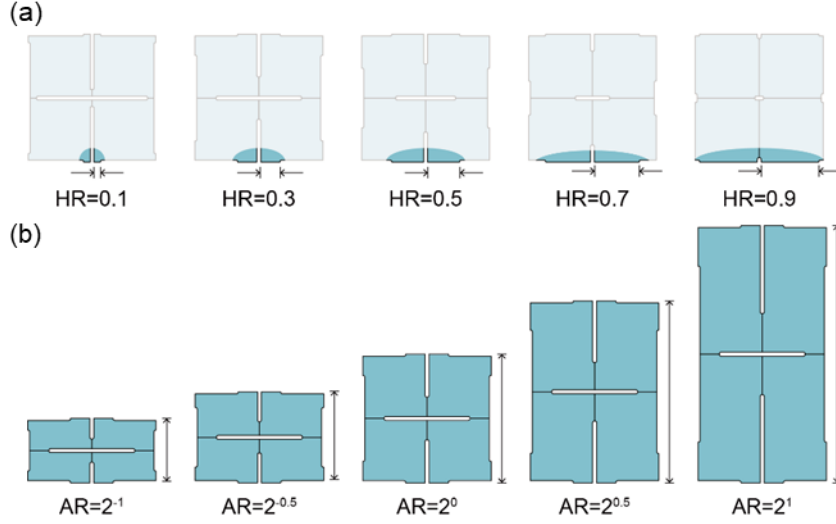


**Figure 2-6. Unit cell variation with changing design variables.** (a) HR variation, and (b) AR variation. The unit length (w) is set as constant, so AR affects only its height.

The design variable determining the width of the narrow-slit holes is SR (slit thickness ratio). This variable may affect the rotational rigidity because the width of the slit is equal to the width of the hinges. Therefore, increasing SR may reduce the rotational rigidity of the hinge resulting lower tensile stiffness, however, we use the constant value of 0.1, so that the rotational rigidity would have been only affected by one design parameter, HR.

## 2.2. Definition of in-plane stiffness

Rotating rigid auxetic unit cell is a 2D pattern formed in planes or curved planes. The in-plane tensile stiffness is defined as the effective normal stress divided by the effective normal strain when the top of the unit cell is subjected a small prescribed displacement in y-direction and the bottom are fixed, as shown in Figure 2-7a. We considered small displacement to limit the scope of this study as the linear regime, and further research can be followed to investigate nonlinear stiffness variation. The in-plane shear stiffness is defined by the effective shear stress divided by the effective shear strain when the unit cell is under pure shear state as shown in Figure 2-7b. We utilized the homogenization method which applies periodic boundary condition with shear strain at a pair of edges of the unit cell. The displacements of the edges are assumed as the below Equations,

$$u_{src} - u_{dst} = u_{pre} \quad (3)$$

$$v_{src} - v_{dst} = v_{pre} \quad (4)$$

where  $u$  and  $v$  denote the displacement of nodes in the global x- and y-direction and the subscripts 'src' and 'dst' represent source and destination nodes, respectively, and 'pre' denotes the prescribed displacement calculated by the applied strain multiplied by the distance between the source and the destination as shown below,

$$u_{pre} = \gamma \cdot d_{TB} \text{ (for the top and bottom pair)} \quad (5)$$

$$v_{pre} = \gamma \cdot d_{LR} \text{ (for the left and right pair)} \quad (6)$$

where  $\gamma$  represents the applied shear strain and  $d_{TB}$  and  $d_{LR}$  denote the distance between the top-bottom and left-right nodes, respectively.

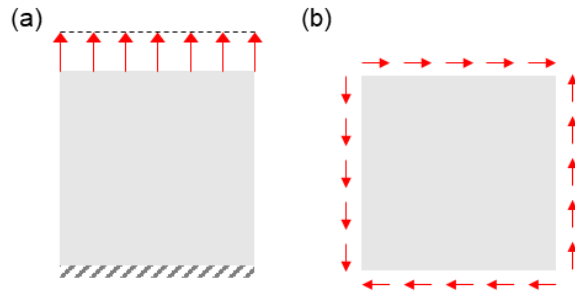


**Figure 2-7. Definition of in-plane stiffness.** (a) Tensile and (b) shear stiffness. In tensile case, the bottom edge is constrained and normal displacements are applied at the top of the material. In shear case, the outer edges are subjected to a shear displacement to represent pure shear deformation.

## 2.3. Deformation mechanism analysis

In this section, the deformation mechanism of the auxetic unit cell under tension and shear is analyzed for the original point-hinge rotating rigid auxetic pattern. Tensile loading induces auxetic deformation and shear loading causes non-auxetic deformation as shown in Figure 2-8. Firstly, we investigated the characteristics of each deformation mode under each loading condition, then we suggested a design direction for slit-pattern auxetics to adjust the two stiffness values.

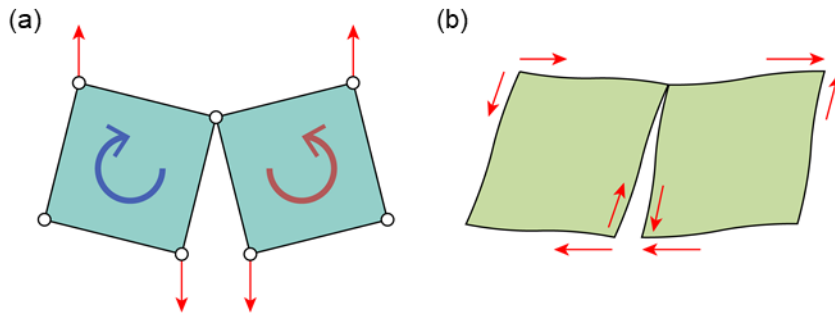


**Figure 2-8. Mechanism of deformation modes of rotating rigid auxetic pattern.**

(a) Auxetic deformation mode, and (b) non-auxetic deformation mode. In the auxetic deformation mode, the rectangles rotate in the opposite direction with the adjacent rectangles, and in the non-auxetic deformation mode, the rectangles do not rotate but themselves deform.

### 2.3.1. Auxetic deformation mode under tension

When a tensile load is applied to the rotating rigid auxetic pattern, rotation moments occur in the squares inside the unit cell due to the connectivity of the hinges, causing them to rotate in opposite directions (Figure 2-8a). The rotation of the squares expands the empty space inside the unit cell, which is the auxetic deformation mode resulting in a negative Poisson's ratio. The stiffness in the auxetic deformation mode will be determined by the rotational rigidity of the point hinges

and the rotation angle of the squares within the unit cell.

In the design of slit pattern auxetic unit cells, the design parameter corresponding to the stiffness of the point hinge is the thickness of the hinge connecting the squares, i.e., HR. Increasing HR corresponds to increasing the thickness of the hinge and the rotational rigidity of the point hinge, so a larger HR value should be set for high tensile stiffness (Figure 2-9).

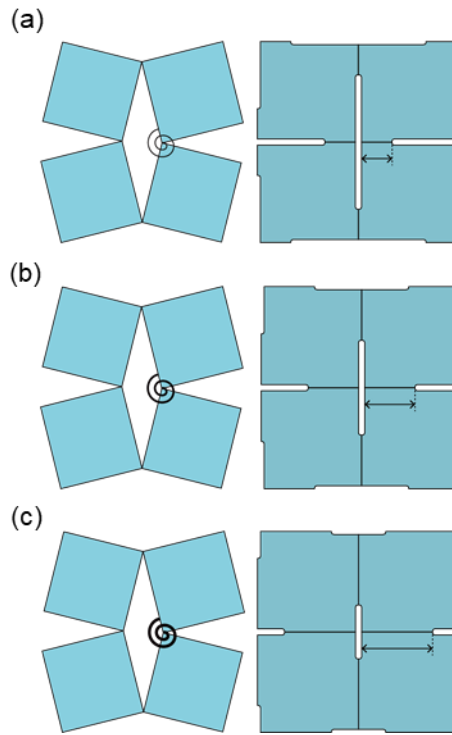


**Figure 2-9. Schematics and unit cell shape according to the variation in HR in auxetic deformation mode.** As HR increases, the rotational hinges become stiff. Example unit cell designs of (a)  $HR = 0.3$ , (b)  $HR = 0.5$ , and (c)  $HR = 0.7$  are shown.

The rotation angle of the inner rectangular is determined by the design variable, AR. We establish an analytical model to explain it. Figure 2-10 shows the variance in the required rotation angle for a constant displacement according to the change in AR.  $h$  and  $h'$  represent the un-deformed and deformed height, respectively,  $\theta$  denotes the required angle, and  $\epsilon$  indicates the strain calculated by the displacement divided by the height in original configuration, as shown in below Equation.

$$\epsilon = \frac{h' - h}{h} \quad (7)$$

For the constant strain  $\epsilon$ , the required rotational angle  $\theta$  is increased. Therefore, AR value should be set larger for a higher tensile stiffness, as shown in Figure 2-11.

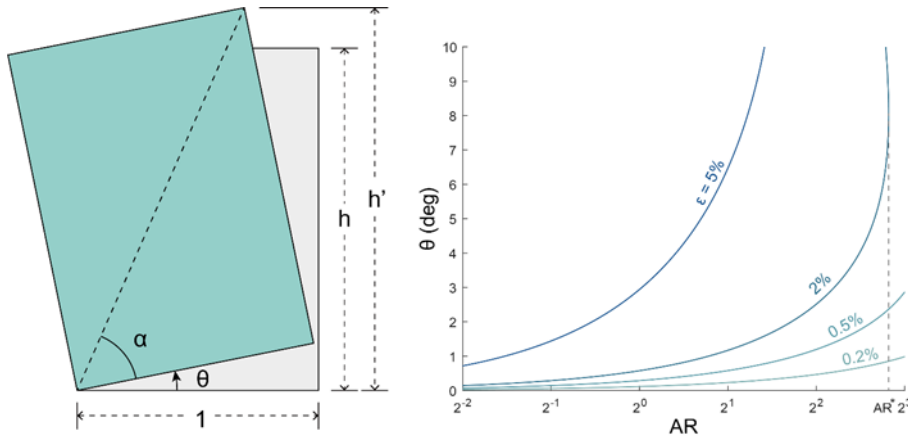


**Figure 2-10. Illustration of relation between aspect ratio AR and rotation angle  $\theta$ .** Left figure represents the variables when the unit cell rotates. Each curve in the right figure shows the relations of AR and  $\theta$ .  $AR^*$  located on the lateral axis is an example of the limit aspect ratio of unit cell to generate specific elongation rate.

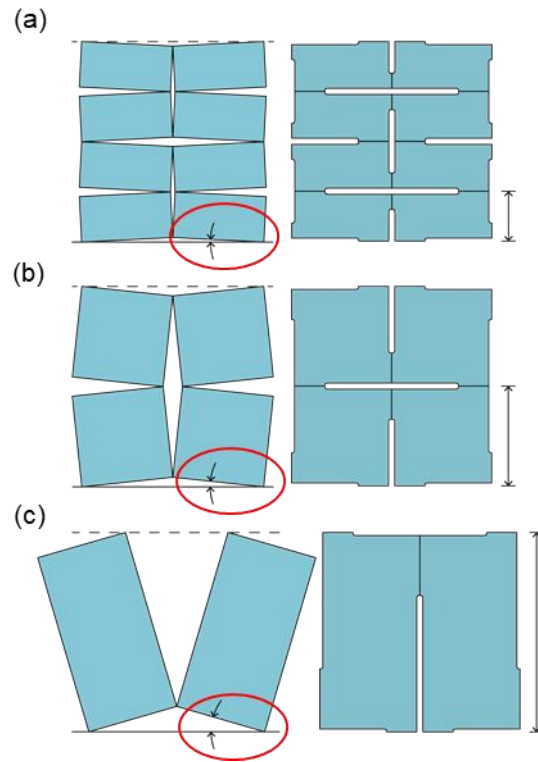


**Figure 2-11. Schematics and unit cell shape according to the variation in AR in auxetic deformation mode.** As AR increases, larger rotation angle is required to reach a certain displacement. Example unit cell designs of (a)  $AR = 2^{-1}$ , (b)  $AR = 2^0$ , and (c)  $AR = 2^1$  are shown.



### 2.3.2. Non-auxetic deformation mode under shear

Tensile loading activated the auxetic deformation mode of the rotating rigid unit, so this unique deformation mode does not appear when the unit cell is subjected to shear load, instead, non-auxetic deformation which is similar to the deformation of continuum occurs. Therefore, the way to control stiffness with changing the design parameters in the non-auxetic deformation is distinct. Design parameter HR does not represent rotational rigidity anymore, but indicates the length of connector linking the rectangle subunits. The shear stiffness will be increased with the longer connectors, so for high shear stiffness, the value of HR should be set large (Figure 2-12).

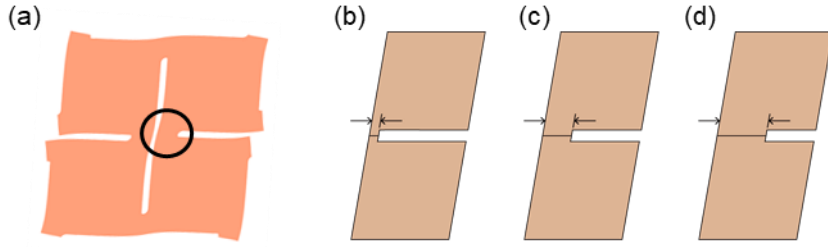


**Figure 2-12. Schematics and unit cell shape according to the variation in HR in non-auxetic deformation mode.** HR represents the length of connectors rather than rotational rigidity. Example unit cell designs of (a)  $HR = 0.3$ , (b)  $HR = 0.5$ , and (c)  $HR = 0.7$  are shown

In the non-auxetic deformation mode, the rectangles within the unit cell do not exhibit rigid-like behavior, but rather undergo deformation themselves. The design variable AR determines the shape of these deforming rectangles. The shape of the rectangle is similar for unit cells with  $AR=2^{-x}$  and  $AR=2^x$ , where  $x$  is greater than or equal to 0, with  $AR=2^0$  as the reference point. Since a pure shear state is assumed, the shear stiffness of the two unit cells is the same. Therefore, the mechanism description can be applied equally to unit cells when AR is greater or smaller than

$2^0$ . In this section, we will only discuss cases where AR is greater than or equal to  $2^0$ .

As AR becomes larger than  $2^0$ , the unit cell takes on a vertically elongated shape. As the unit cell becomes closer to an elongated rectangle, the deformation that occurs when subjected to shear force will resemble the bending of a beam, resulting in a lower stiffness compared to the shear-like deformation of a square unit cell. Figure 2-13 below shows the change in the deformation shape of the unit cell with respect to the change in AR value under the same strain. For a clear comparison, each unit cell is scaled in the y-direction. As the unit cell becomes vertically elongated, bending-like deformation occurs on the side faces of the unit cell, indicating that the structure will become more flexible.

Therefore, to increase the shear stiffness, the shape of the unit cell should be closer to a square, and the AR value should be closer to  $2^0$  (see Figure 2-14).

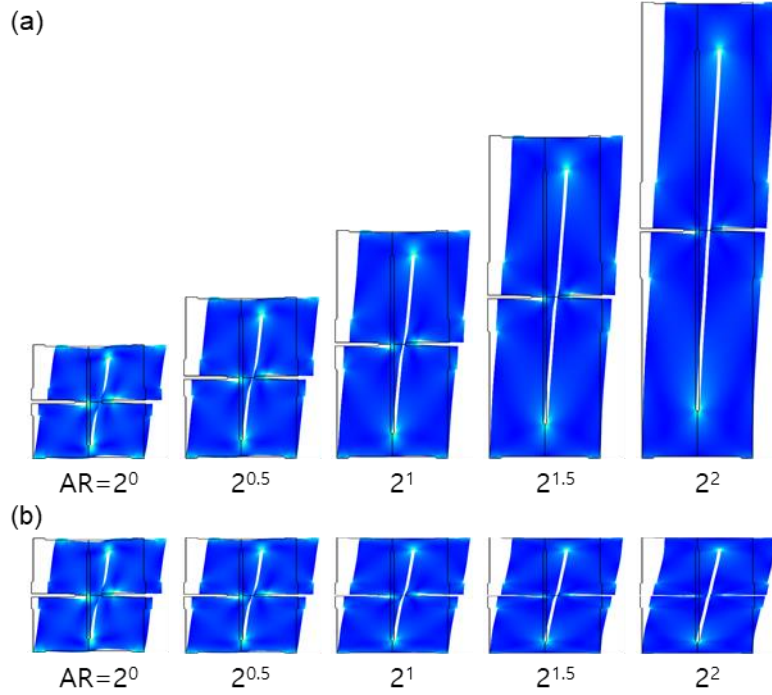


**Figure 2-13. Deformed shapes with the variation in AR.** (a) As AR increases, the overall deformed shape of the unit cells becomes bending-like configuration, which is flexible than pure shear deformation. (b) Clear difference of the side edges of the unit cells is observed in the scale-down configurations.

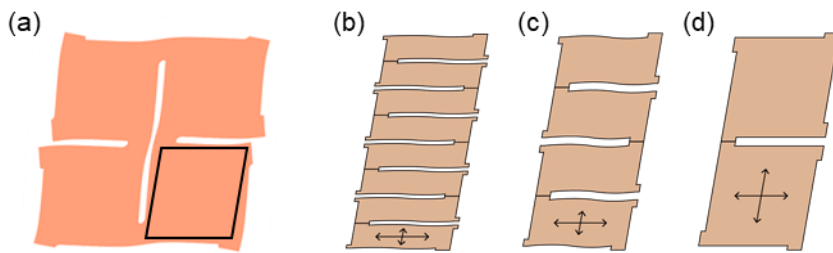


**Figure 2-14. Schematics and unit cell shape according to the variation in AR in non-auxetic deformation mode.** AR determines the deformed shape of subunits. As AR value is apart from  $2^0$  further, subunits experience beam-like flexural shear deformation. Example unit cell designs of (a)  $AR = 2^{-2}$ , (b)  $AR = 2^{-1}$ , and (c)  $AR = 2^0$  are shown.

## 2.4. Finite element analysis

We utilized a commercial multi-physics software, COMSOL 5.3, to investigate the in-plane tensile and shear stiffness of the auxetic pattern. We performed a comprehensive parametric study for the two design parameters HR and AR. HR is ranged from 0.1 to 0.7 with the interval of 0.1, and AR is distributed from  $2^{-2}$  to  $2^2$  with the interval of 0.2 in the exponent.

The 2D auxetic pattern is discretized with six-node triangular plane-stress elements. We performed a study for the mesh size for a converged solution. For the ratio of the minimum size mesh divided by the unit length  $a$ , 0.01 was enough for the ratio for a converged solution as shown in Figure 2-15.

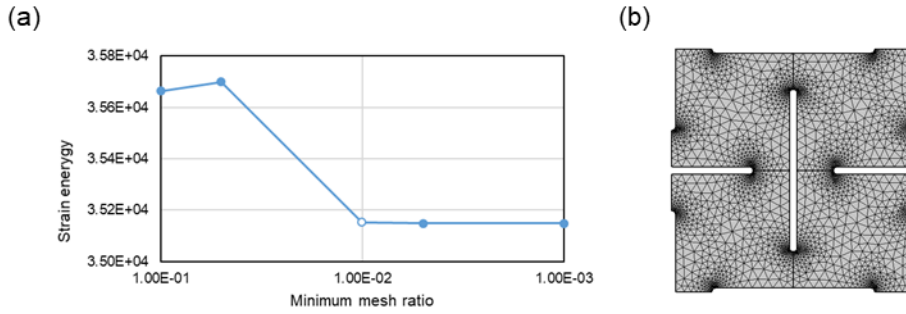


**Figure 2-15. Mesh convergence test.** (a) Strain energy graph as a function of the minimum mesh size ratio. (b) Mesh resolution. The minimum mesh ratio of 0.01 was enough for a converged solution.

For the boundary condition to calculate the tensile stiffness of auxetic patterns, the bottom edges are fixed, and the top edges are subjected to prescribed displacement in y-direction. In the case of shear stiffness, we imposed a periodic boundary condition for the top-bottom edges pair and left-right edges pair as shown in Equations 1 and 2. We obtained resultant strain energy, SE, and calculated the two stiffness  $K_T$  and  $K_S$  with the below Equation,

$$SE = \frac{1}{2}K\epsilon^2 \quad (8)$$

where  $\epsilon$  represents the applied strain. The two stiffness values are then normalized by dividing them by the stiffness of a non-patterned solid unit, resulting dimensionless stiffness  $K_T^*$  and  $K_S^*$ .

## 2.5. Design principle for simultaneous control of in-plane stiffness

This section includes the results of design of in-plane tensile and shear stiffness of the auxetic pattern. We investigated the effect of the design parameters on the stiffness of the corresponding deformation modes, based on the result of FE analysis. Then, we provide the design principle of the in-plane auxetic pattern by adjusting the key design variables.

### 2.5.1. In-plane tensile stiffness control

Design variable HR is a determining factor for the rigidity of the rotational hinge in the auxetic deformation mode. As a result, it was expected that a higher value of HR should be set for higher tensile stiffness in the previous section. Figure 2-16 illustrates the change in dimensionless tensile stiffness,  $K_T^*$ , as a function of HR. Each curve corresponds to a different value of design variable AR. It can be observed that as HR increases,  $K_T^*$  also increases. Examining the y-direction normal stress distribution for the unit cells corresponding to the three black dots in the figure, as shown in Figure 2-17, it is evident that stress is concentrated at the hinge rather than the rectangles inside the unit cell. This indicates that the hinge acts as a rotational spring, while the internal rectangles undergo minimal deformation and rotate like rigid bodies.

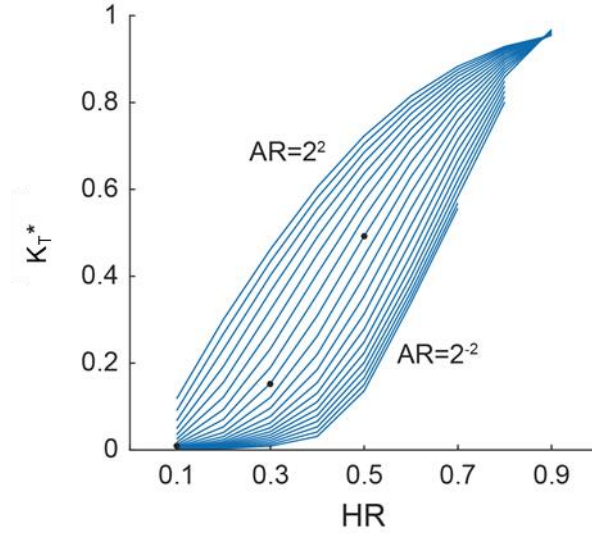


**Figure 2-16. In-plane tensile stiffness adjustment by changing HR.** Each curve corresponds to a constant AR value. The lateral and vertical axes represent the design variable HR and the normalized tensile stiffness, respectively. As HR increases, higher rigidity of rotational hinges is assumed, therefore the tensile stiffness increases.

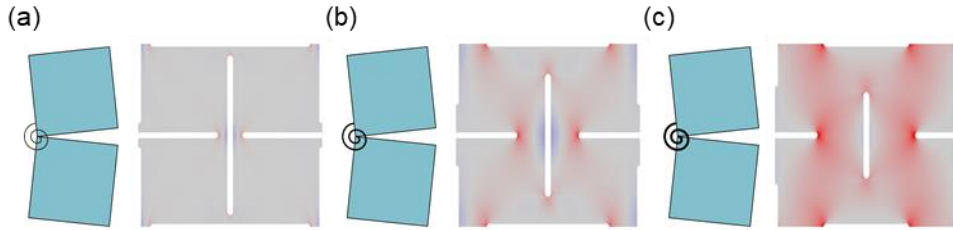
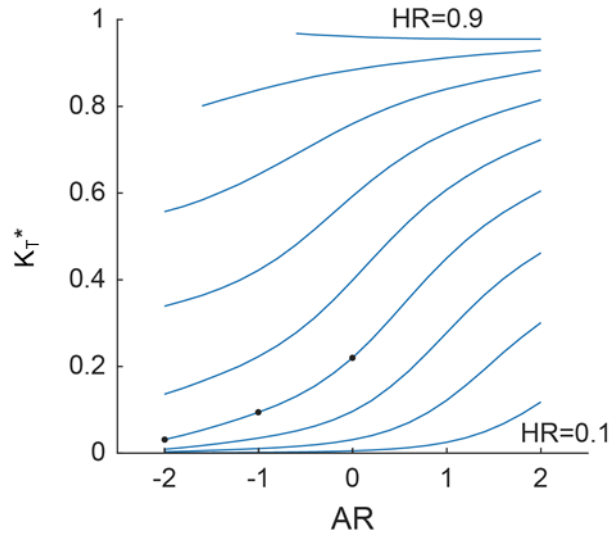


**Figure 2-17. Schematics and normal stress distribution with the change in HR.** Relative normal stress distribution in the y-direction is plotted next to schematic figure. (a)  $HR = 0.1$ , (b)  $HR = 0.3$ , and (c)  $HR = 0.5$ . The color map is ranged from blue for a negative stress, and to red for a positive stress.

Design variable AR is a parameter that determines the shape of the rectangles within the unit cell and is related to the required rotation angle of the rectangles in the auxetic deformation mode. As the shape of the rectangle becomes taller, the

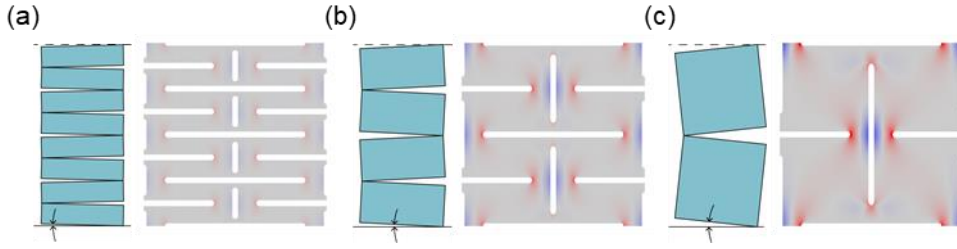
required rotation angle to achieve a certain displacement increases. Consequently, it was anticipated in the previous section that for higher tensile stiffness, the value of AR should be set higher.

Figure 2-18 depicts the change in dimensionless tensile stiffness,  $K_T^*$ , as a function of AR, with each curve corresponding to a single value of HR. It can be observed that as AR increases, tensile stiffness monotonically increases. The normal stress distribution for the unit cells corresponding to the three black dots in the figure is shown in Figure 2-19. As AR increases, the stress magnitude occurring in the hinge part also increases. Since the hinge thickness for all three unit cells is the same, the cause of the increased stress is likely due to the increase in the rotation angle.



**Figure 2-18. In-plane tensile stiffness adjustment by changing AR.** Each curve corresponds to a constant HR value. As AR increases, larger rotational angle is required, therefore the tensile stiffness increases.





**Figure 2-19. Schematics and normal stress distribution with the change in AR.**

Relative normal stress distribution in the y-direction is plotted next to schematic figure. (a)  $AR = 2^{-2}$ , (b)  $AR = 2^{-1}$ , and (c)  $AR = 2^0$ . The color map is ranged from blue for a negative stress, and to red for a positive stress.

The design parameters HR and AR play crucial roles in determining the tensile stiffness of the auxetic pattern. HR, which affects the rotational rigidity of the hinges, should be set higher to achieve increased tensile stiffness. Similarly, AR, which influences the shape of the rectangles within the unit cell and the required rotation angle in the auxetic deformation mode, should also be set higher to enhance tensile stiffness.

### 2.5.2. In-plane shear stiffness control

Under shear loading conditions that induce non-auxetic deformation modes, the design parameter HR determines the length of the connectors. As the length of the connectors increases, the shear stiffness of the unit cell also increases, as shown in Figure 2-20. The vertical axis of the graph represents the dimensionless shear stiffness  $K_s^*$ . The unit cell shapes and shear stress distributions corresponding to the three black points on the graph are illustrated in Figure 2-21. As HR increases, higher levels of stress occur in the connectors and internal rectangles due to the larger forces generated during the same shear deformation.

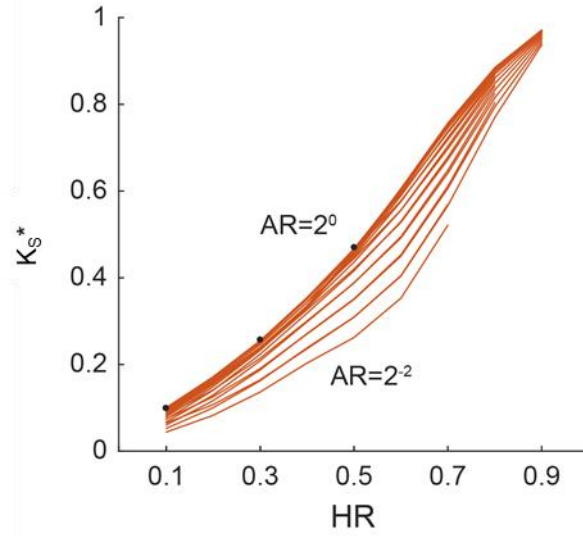


**Figure 2-20. In-plane shear stiffness adjustment by changing HR.** Each curve corresponds to a constant AR value. As HR increases, longer connector width occupies, therefore the shear stiffness increases.

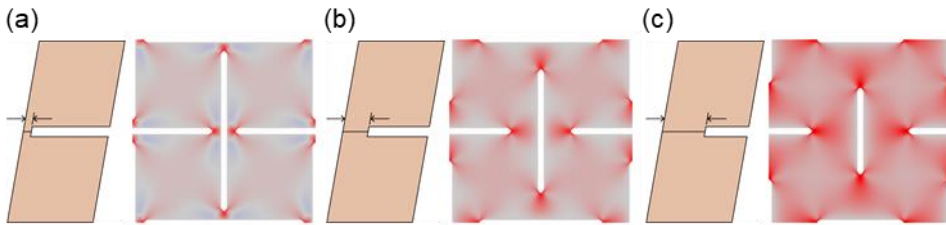


**Figure 2-21. Schematics and shear stress distribution with the change in HR.** Relative shear stress distribution is plotted next to schematic figure. (a)  $HR = 0.1$ , (b)  $HR = 0.3$ , and (c)  $HR = 0.5$ . The color map is ranged from blue for a negative stress, and to red for a positive stress.

The change in shear stiffness due to variations in the design parameter AR exhibits a different pattern compared to previous results. As discussed in the mechanism analysis, when the unit cell becomes a flatter or elongated shape in the vertical direction, bending-like shear deformation occurs, making shear deformation easier. Therefore, the highest stiffness is observed when AR is  $2^0$ , as shown in Figure

2-22. The unit cell shapes and shear stress distributions for the three points on the graph are presented in Figure 2-23. As AR decreases, negative shear stresses occur near the edges of the unit cell, indicating that the edges of the unit cell deform with flexure. The negative shear stress distribution diminishes as AR approaches  $2^0$ .

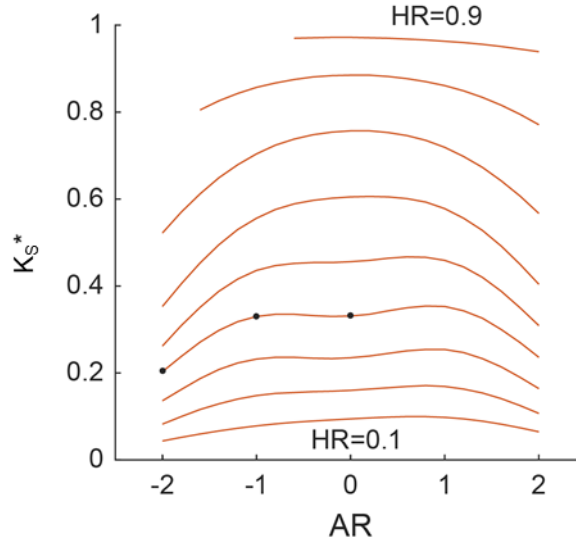


**Figure 2-22. In-plane tensile stiffness adjustment by changing AR.** Each curve corresponds to a constant HR value. As AR value is closer to  $2^0$ , shear-dominant deformation appears resulting a higher shear stiffness.

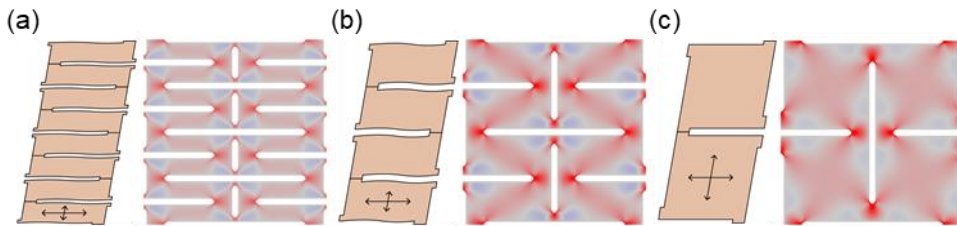


**Figure 2-23. Schematics and shear stress distribution with the change in AR.** Relative shear stress distribution is plotted next to schematic figure. (a)  $AR = 2^{-2}$ , (b)  $AR = 2^{-1}$ , and (c)  $AR = 2^0$ . The color map is ranged from blue for a negative stress, and to red for a positive stress.

However, the analytical results reveal that the shear stiffness for the case of AR being  $2^{-1}$  is similar to that when AR is  $2^0$ . This similarity appears to originate from the definition of the unit cell in this study. Both horizontal and vertical hinge thicknesses are defined through a single design parameter, HR. As AR increases, the vertical length of the unit cell grows, and the length of the vertical hinges increases as well. This increase appears to enhance the stiffness of the unit cell due to the combined influence of these factors.

The design parameters HR and AR significantly influence the shear stiffness of the unit cell, but in a different manner from the case of tension. An increase in HR, which determines the length of the connectors, leads to higher shear stiffness, as it results in larger forces during shear deformation and higher levels of stress in the connectors and internal rectangles. On the other hand, the shear stiffness is affected by AR in a non-linear manner; the highest stiffness is observed when AR is  $2^0$ . This is due to the bending-like shear deformation that occurs when the unit cell takes a flatter or elongated shape in the vertical direction, making shear deformation easier. The combined effect of HR and AR plays a crucial role in controlling the in-plane shear stiffness of the unit cell.

### 2.5.3. Results of tilted rotating rigid auxetic pattern

To confirm the potential for expanding the stiffness range achievable with a rotating rigid unit (RRU) pattern, we examined the feasibility using a model that rearranges the rectangular RRU pattern. Figure 2-24 shows the configuration of a rectangular pattern that has been rotated by 45 degrees. The 45-degree rectangular pattern was defined by the same design variables, hinge thickness ratio (HR), and aspect ratio (AR).

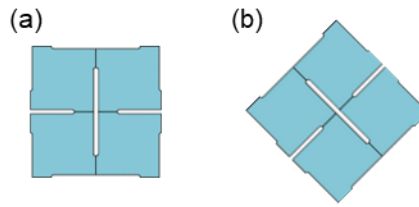


**Figure 2-24. 45-degree rectangular pattern.** (a) The original pattern. (b) 45-degree rectangular pattern.

The force experienced by the 45-degree tilted rectangular pattern under tensile and shear loading conditions can be easily understood through coordinate transformation. Firstly, when tensile loading is applied, the state of the force experienced by the original unit is transformed into a rotated coordinate system, resulting in the state of force shown in Figure 2-25. In this state, both shear stress and normal stress are experienced simultaneously. Therefore, the tensile stiffness change of the 45-degree tilted unit would depend on the changes in the normal and shear stiffness of the original unit.

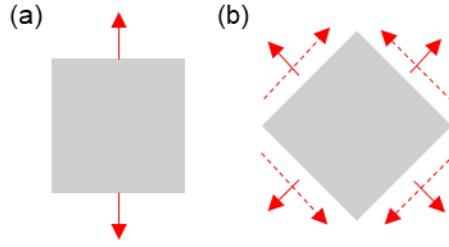


**Figure 2-25. Force state of 45-degree pattern under tension.** (a) In the original coordinate. (b) In the rotated coordinate.

When shear loading is applied to the tilted pattern, the principal axes are determined in the 45-degree direction, causing only normal stress as shown in Figure 2-26. Thus, the shear stiffness change in the tilted pattern will be dependent on the normal stiffness change in the original rectangular pattern. Note that both stiffnesses of the tilted pattern are related to the normal stiffness in both x- and y-directions of the original pattern. Therefore, unlike the previous section that only considered normal stiffness (tensile stiffness) in the y-direction, both stiffnesses must be considered.

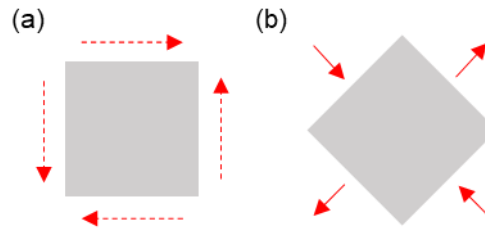


**Figure 2-26. Force state of 45-degree pattern under shear.** (a) In the original coordinate. (b) In the rotated coordinate.

To investigate the stiffness changes of the tilted pattern, a periodic boundary condition was applied to the 45-degree rectangular unit, and the two in-plane stiffnesses were computed via simulation. For the two design variables, HR ranged from 0.3 to 0.7, and AR ranged from  $2^{-2}$  to  $2^2$ . As shown in Figure 2-27, both the tensile and shear stiffness increase as HR increases. This aligns with the result from the original pattern where stiffness increases with HR, regardless of the type of

stiffness.

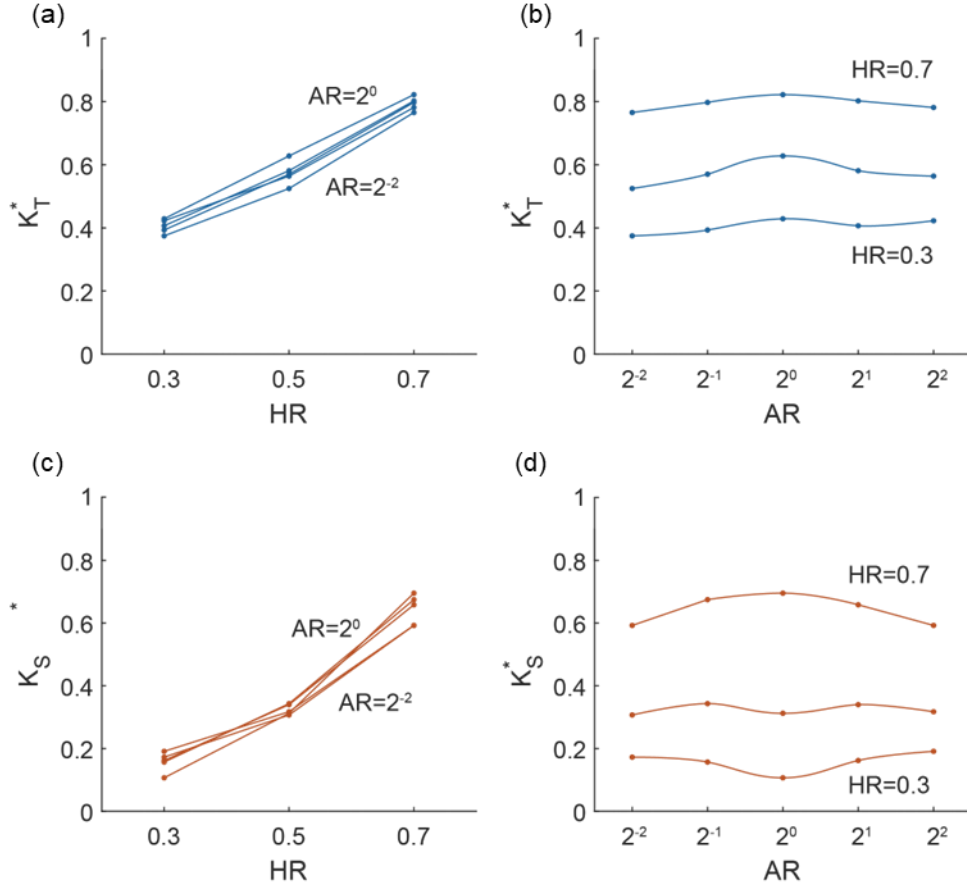


**Figure 2-27. In-plane tensile stiffness adjustment of 45-degree pattern.** The tensile stiffness adjustment according to the variation of (a) HR and (b) AR, and the shear stiffness adjustment according to the variation of (c) HR and (d) AR.

However, an increase in AR displays a different pattern for both types of stiffness compared to the results from the original pattern. The shear stiffness of the tilted pattern changes symmetrically around  $AR = 2^0$ . When a pure shear load is applied, the principal axes are determined in the direction rotated by 45 degrees. Therefore, the shear stress  $\tau$  in the global coordinate leads to the occurrence of normal stress of  $+\tau$  and  $-\tau$  on each face of the tilted unit. The changes in the normal stiffness in the x and y directions of the original pattern are inversely related to changes in AR. For

example, the x-direction stiffness at  $AR=2^{-1}$  is identical to the y-direction stiffness at  $AR=2^1$ . Therefore, the shear stiffness of the tilted pattern varies symmetrically around  $AR = 2^0$  as shown in Figure 2-28a, and 28b. The variation of  $C_{33}$  component of the elasticity matrix of the tilted patterns is shown in Figure 2-28c. It can be calculated by transforming the elasticity matrix of the original pattern by 45 degrees, or by directly performing analysis about the tilted pattern.

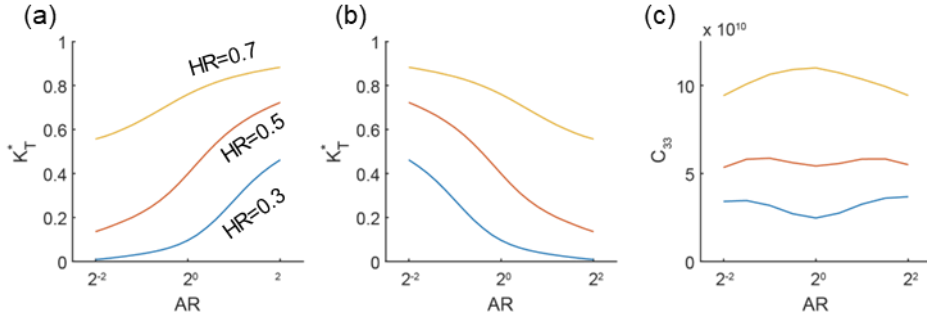


**Figure 2-28. Explanation of shear stiffness variation of 45-degree pattern.** The variation of the normal stiffness in (a) y-direction and (b) x-direction of the original pattern. (c) the variation of  $C_{33}$  component of elasticity matrix of the tilted patterns.

In the case of tensile loading applied to the tilted pattern, the 45-degree tilted unit simultaneously receives normal and shear forces. Therefore, the tensile stiffness of the tilted pattern would be determined by the normal stiffness and shear stiffness of the original pattern. The changes in these two stiffnesses of the original patterns according to the AR values are shown in Figure 2-29a and 29b. Their variation is symmetry around  $AR = 2^0$ , so the tensile stiffness of the tilted pattern varies with symmetry. The variation of  $C_{33}$  component of the elasticity matrix of the tilted pattern is shown in Figure 2-29c. It also can be obtained by transforming the elasticity matrix of the original pattern by 45 degrees, or by directly performing analysis about the tilted pattern.



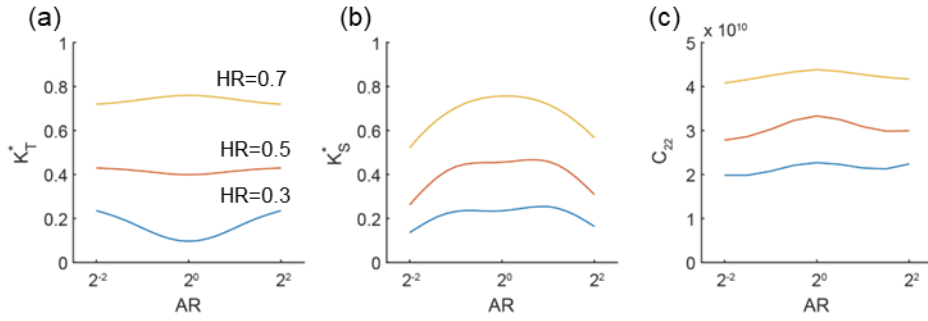


**Figure 2-29. Explanation of tensile stiffness variation of 45-degree pattern.** (a) The variation of the averaged normal stiffness, (b) the shear stiffness variation of the original pattern, and (c) the variation of  $C_{22}$  component of elasticity matrix of the tilted patterns.

## 2.6. Conclusion

In this chapter, we have presented a design methodology for the rotating rigid auxetic pattern that utilizes the load-dependency in the deformation modes of auxetic patterns, allowing the simultaneous design of two inherently coupled in-plane stiffness values (tensile and shear stiffness). We have selected the rotating rigid auxetic pattern as the basic design unit cell due to its ease of fabrication and broad stiffness tuning capability. Design parameters HR (hinge thickness ratio) and AR (aspect ratio) were defined to design the stiffness for the distinct auxetic and non-auxetic deformation modes that occur under tensile and shear loads. Analytical and numerical approaches confirmed that the roles of the design variables differ depending on each deformation mode, and the two stiffness values can be adjusted simultaneously.

The results discussed here concern the design of auxetic unit cells, which may have a broad applicability in creating various structures by arranging them in different geometry. Although only rectangular pattern unit cells have been discussed in this chapter, it is expected that stiffness control would be possible in a similar manner for rotating rigid unit cells composed of other polygonal shapes. Although the slit thickness ratio, one of the unit cell definitions, also seems to be involved in the stiffness control mechanism for adjusting both stiffness values, it has been set to a fixed value in this study for the sake of clarity in the stiffness control design methodology. Utilizing the slit thickness ratio as an additional design variable could expand the designable stiffness range.

## Chapter 3. Simultaneous adjustment of tube stiffness: Auxetic meta-tube

### 3.1. Introduction

Utilizing the load-dependent behavior of auxetic patterns for the simultaneous control of tensile and shear stiffness allows for the design of meta-structures to address various real-world engineering problems. In this study, the first meta-structure proposed is the auxetic meta-tube. The auxetic meta-tube is a tube with auxetic patterned holes, designed to enable the simultaneous control of the tube's bending and torsional stiffness.

Simultaneous control of stiffnesses in the bending and torsional directions can be particularly useful in the field of biomedical robotics. One such application is the concentric tube robot, which consists of multiple pre-curved, thin tubes stacked together. By controlling the rotation of these tubes, the robot can achieve complex movements within the body. One critical issue that needs to be addressed for the effective use of this robot is instability. As rotation is applied to the tube, elastic energy accumulates, and when this energy reaches a certain level, a snap-through phenomenon occurs, causing a sudden release of energy. This instability can pose serious risks during operation, and to prevent it, the stability criterion is as follows<sup>35</sup>:

$$L\kappa \sqrt{\frac{EI}{GJ}} < \frac{\pi}{2} \quad (9)$$

where  $L$  denotes the tube length,  $\kappa$  indicates the tube curvature, and  $EI$  and  $GJ$  denote the bending and torsional rigidity of the tube, respectively.

Analyzing the cross-sectional state of the tube when subjected to bending and torsional loads, as shown in Figure 3-1, tensile and compressive forces are applied on the top and bottom parts of the cross-section in bending. In contrast, the entire

cross-section is subjected to shear forces in torsional case. Therefore, we can design the bending stiffness of the tube by utilizing the auxetic deformation mode, and torsional stiffness with the non-auxetic deformation mode. Through the design of auxetic meta-tubes, we aim to explore ways to improve the stability of concentric tube robots.

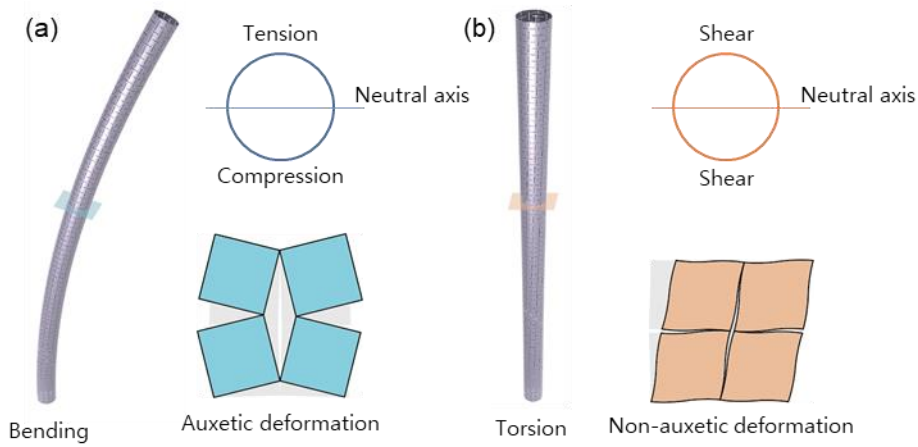


**Figure 3-1. Loading status of cross-section of auxetic meta-tube.** The deformed configuration of auxetic meta-tubes and the loading status of the cross-section are present for (a) bending, and (b) torsional deformation.

## 3.2. Auxetic meta-tube

We present the definition of auxetic meta-tube in this section. The in-plane auxetic unit cell is transformed to form a tubular structure. The main design variables of the auxetic meta-tube are the same as the in-plane unit cell. We also investigated the effect of the other design variables.

### 3.2.1. Definition of auxetic meta-tube

The main design parameter of the auxetic meta-tube is the same with the in-plane auxetic unit cell; AR and HR. Note that AR only affects the unit cell height, and the unit cell width is always decided by the diameter of the tube. The other design parameter, slit thickness ratio (SR), was set at 0.062 considering the fabrication resolution of the actual auxetic tube. HR is ranged from 0.1 to 0.9 with the interval of 0.1 and AR is distributed from  $2^{-2}$  to  $2^3$  with the interval of 0.2 in the exponent.

Regarding the main design parameters, AR and HR, a geometrical constraint exists when determining the auxetic meta-tube due to slit thickness, which limits the maximum value of the hinge thickness ratio (HR) as expressed in below Equations. The relatively short sides in a unit cell create the restriction, resulting in two conditions based on AR. In the design space, 12 cases do not meet the restriction, including  $AR=2^{-2}$  and  $2^{-1.8}$  for  $HR=0.8$ , and  $AR=2^{-2}$ ,  $2^{-1.8}$ , ...,  $2^0$  for  $HR=0.9$ .

$$HR < 1 - SR \quad (\text{for } AR \geq 1) \quad (10)$$

$$HR < 1 - \frac{SR}{AR} \quad (\text{for } AR < 1) \quad (11)$$

Six auxetic unit cells is arranged in the circumferential direction to form a unit cell layer many of which are stacked to form an auxetic meta-tube as shown in Figure 3-2. As mentioned before, the unit cell width is constant and the number of the unit layers varies depending on the design parameters AR for a given tube length. Various

design examples of auxetic meta-tubes are shown in Figure 3-3.

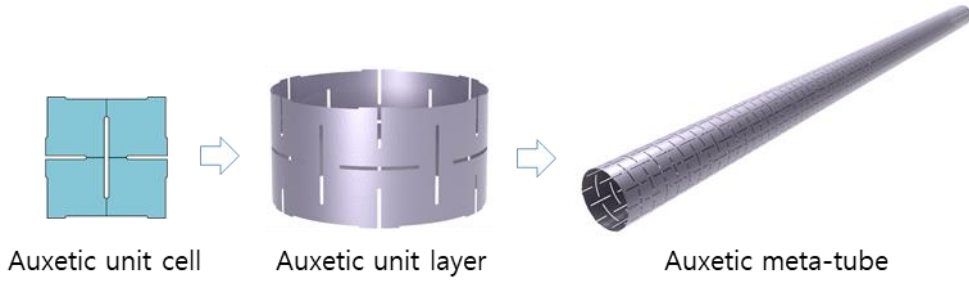


**Figure 3-2. Consisting of auxetic meta-disk.** Six auxetic unit cell is arranged in the circumferential direction to build a auxetic unit layer, and the layers are stacked axially to form an auxetic meta-tube.

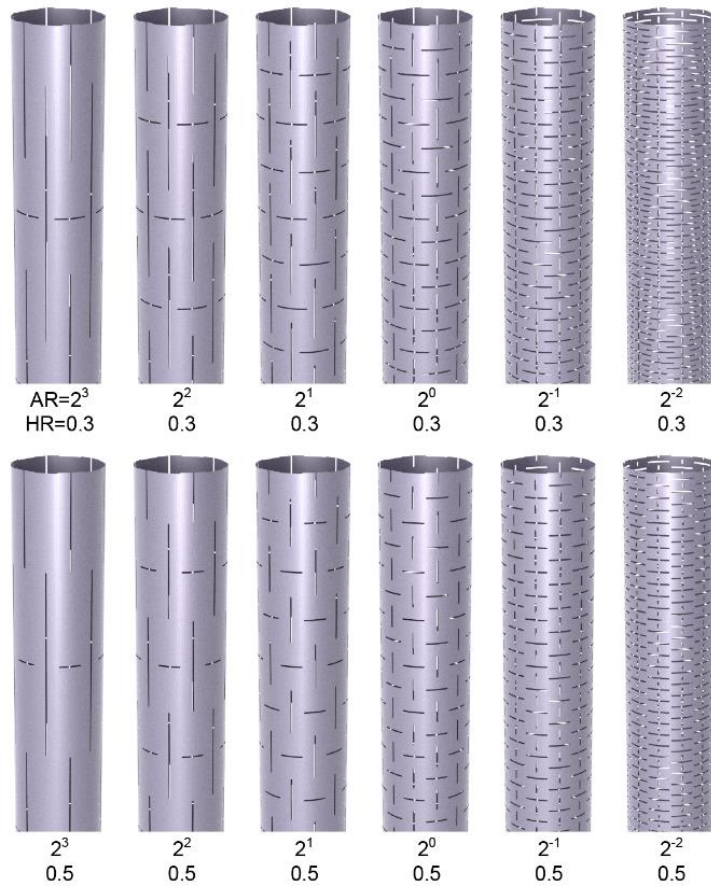


**Figure 3-3. Various examples of auxetic meta-tube.**

### 3.2.2. Study for other design variables

The auxetic meta-tube has seven design variables in total: tube length ( $L$ ), tube thickness ( $t$ ), unit cell aspect ratio (AR), unit cell hinge thickness ratio (HR), unit cell slit thickness ratio (SR), the number of unit cells in a unit layer ( $n$ ), and the number of unit cell layers ( $m$ ). The tube dimensions, with a height of 1 meter and thickness of 1 millimeter, determine  $L$  and  $t$ .

The number of the unit cells in a unit layer ( $n$ ) is determined by considering the curvature effect which comes from arranging the unit cells into the curved surface of tubes. We performed a convergence test for the number of unit cells in a layer to ensure little curvature effect, as shown in Figure 3-4. The vertical axis represents bending stiffness of meta-tubes, which will be introduced in the next section. We found the  $n$  value of six (or 12 subunits) would be enough for a converged solution. For the number of the unit layers in an auxetic meta-disk, a convergence test was performed to minimize an end effect, and the result confirmed that adequate number of the unit layer is 80 for the unit cell with AR of 2<sup>0</sup>.

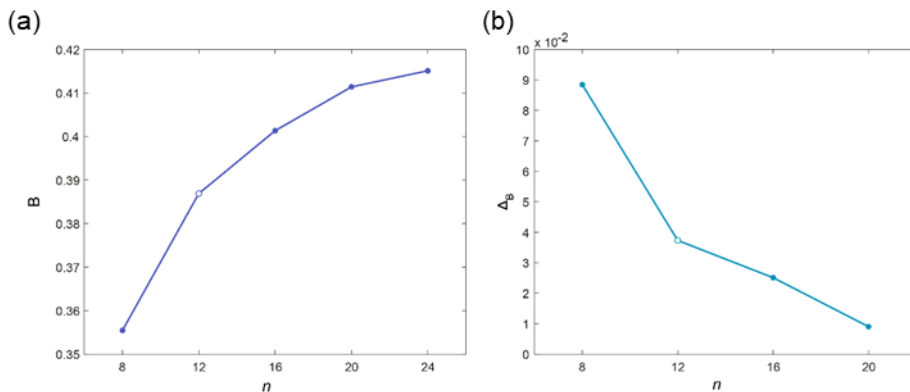


**Figure 3-4. Convergence test on the number of unit cell in circumferential direction,  $n$ .** The lateral axes represent  $n$ , which is double of the value of the number of the unit cells.  $n$  of 12 (six unit cells) was enough to minimize the curvature effect of the auxetic meta-tube.

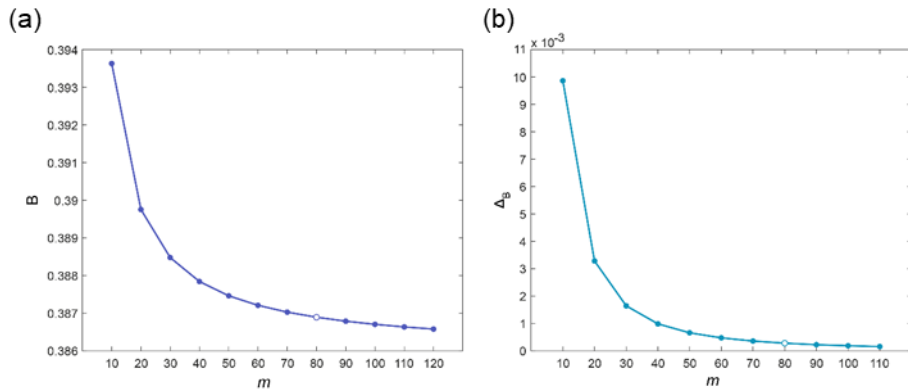


**Figure 3-5. Convergence test on the number of unit cell layers,  $m$ .** The lateral axis represent  $m$ , which is double of the value of the number of the unit layers.  $m$  of 80 (40 unit layers) for 1 m length tube was enough to ignore the boundary effect in the case of AR equal to  $2^0$ .



### 3.3. Finite element analysis

The simultaneous adjustment of bending and torsional stiffness of the auxetic meta-tube was numerically verified by FE analysis. In this section, the FE model information about auxetic meta-tubes is included and the definition of tube stiffness is represented. Additionally, a convergence study result of the minimum size of the mesh for a converged solution is also contained.

#### 3.3.1. Analysis model

We constructed a FE analysis model of the auxetic tubes by utilizing 6-node triangular shell elements. We conducted linear static analysis using the ADINA 9.0 software, a commercial finite element analysis tool, to determine the values of bending and torsional stiffness. The bottom nodes of the tube were subjected to a fixed boundary condition, while the top nodes were connected through a rigid link to represent the loading condition depicted in Figure 3-6. By applying a prescribed rotation in either the y- or z-directions at the master node of the rigid links, we conducted the static deformation analysis.

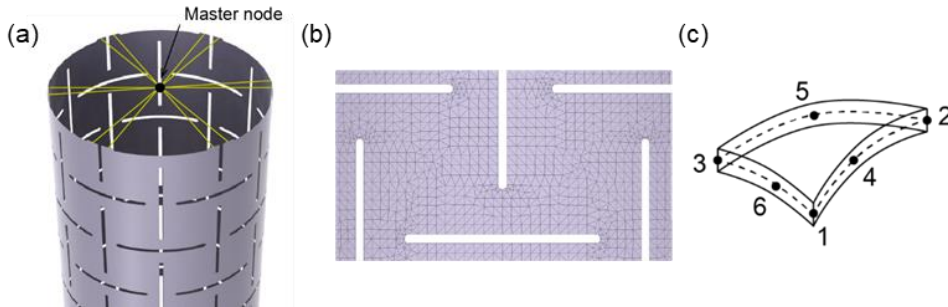


**Figure 3-6. Analysis model of auxetic meta-disk.** (a) Tie constraint connecting the master node and the top edges, (b) mesh resolution, and (c) six-node shell element. The bottom edges of the meta-tube were fixed, and small prescribed bending and torsional rotations are applied at the master node.

### 3.3.2. Definition of tube stiffness

The reaction moment at the master node was obtained, and the rigidities of a tube in the two directions (EI and GJ) were calculated using Equations 12 and 13.

$$EI = \frac{M_b L}{\theta_b} \quad (12)$$

$$GJ = \frac{M_t L}{\theta_t} \quad (13)$$

where  $M_b$  and  $M_t$  denote the reaction moment in the bending and torsional directions, and  $\theta_b$  and  $\theta_t$  indicate the prescribed rotation angle in the y- and z-direction, respectively.

The bending stiffness (B) and the torsional stiffness (C) of tubes are defined as below,

$$B = \frac{EI}{L} \quad (\text{N} \cdot \text{m}) \quad (14)$$

$$C = \frac{GJ}{L} \quad (\text{N} \cdot \text{m}) \quad (15)$$

and they are normalized by divided by the stiffness values of the non-patterned tube, resulting dimensionless bending and torsional stiffness  $B^*$ , and  $C^*$ .

### 3.3.3. Convergence test

We performed a convergence test for the size of the mesh to ensure a converged solution. We gradually reduced the minimum mesh size from 0.2 mm to 0.04 mm, and conclude that 0.08 mm was suitable for analysis, as shown in Figure 3-7. The applied mesh is shown in Figure 3-6. We applied a finer mesh around the hinges where stress concentration may occur.

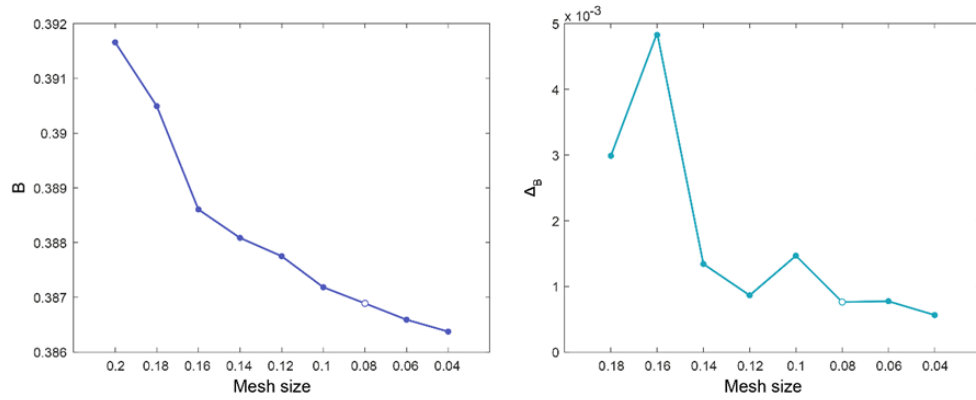


**Figure 3-7. Convergence test on the mesh size with varying the maximum element size.** The left figure represents stiffness value convergence and the right figure shows the stiffness difference between the mesh sizes. It was confirm that the minimum mesh size of 0.08 was enough for a converged solution.

### 3.4. Experimental verification

The information of fabrication of auxetic meta-tube, experimental procedure, and data processing method is presented in this section. For experimental validation, thirteen types of auxetic meta-tubes were fabricated. The design parameters of the specimens are shown in Table 3-1.

#### 3.4.1. Fabrication

Aluminum tubes were selected, featuring dimensions of 48 mm diameter, 1 mm thickness, and 995 mm length, with a Young's modulus of 70 GPa, density of 2700 kg/m<sup>3</sup>, and Poisson's ratio of 0.34. The auxetic patterns were engraved by high-resolution laser machining. To minimize thermal distortion during the laser processing and to account for device resolution, we set slit widths as 0.77 mm. The tube specimens can be seen in Figure 3-8.



**Figure 3-8. Auxetic meta-tube specimens.** The auxetic meta-tubes are fabricated by high-resolution laser cutting.

### 3.4.2. Modal testing

We employed a modal testing method to obtain the bending and torsional stiffnesses of the specimens. To conduct bending modal test, we applied an impact force with an impact hammer near the end of a tube. An accelerometer was affixed to the outer surface of the tube's center, as depicted in Figure 3-9, to capture the flexural vibratory signals. The output signals were processed to produce the frequency response function (FRF). The fundamental bending mode was identified as the frequency corresponding to the first peak in the FRF curves. The FRF curves for all specimens can be found in the Appendix.

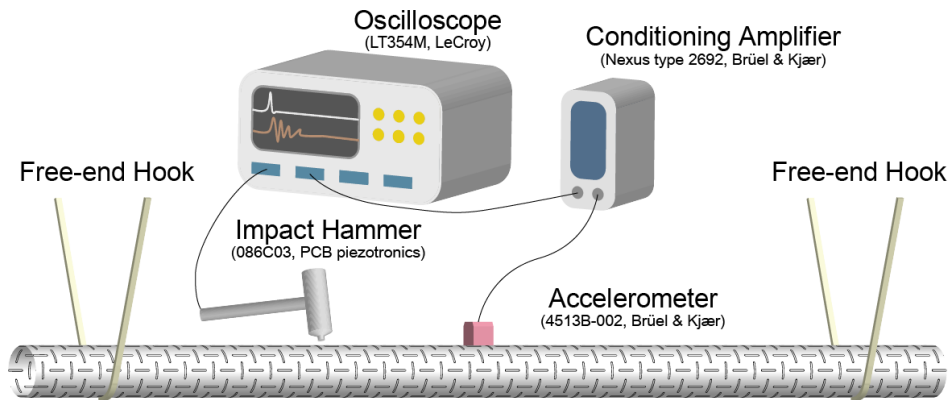


**Figure 3-9. Modal test setting (bending).** A meta-tube specimen is placed on free-end hooks to assign free-free boundary condition to the auxetic tube. Impact hammer generates impact load and the resultant responses are measured from the accelerometer located at the center of the tube.

We utilized magneto-strictive patch transducers in the testing of torsional modes to effectively induce and measure torsional vibrations in the tube. Two identical transducers were placed at locations that divide the length of the tube into thirds, as shown in Figure 3-10. One transducer converted an electronic impact signal into a mechanical torsional impact pulse, while the other transducer recorded the torsional vibratory signals. The resulting FRF was obtained, with the primary peak

frequency representing the fundamental torsional mode. In contrast to the modal testing for bending, smaller peaks were observed below the dominant peak frequency range during torsional modal testing. These smaller peaks corresponded to radial modes generated through coupling.

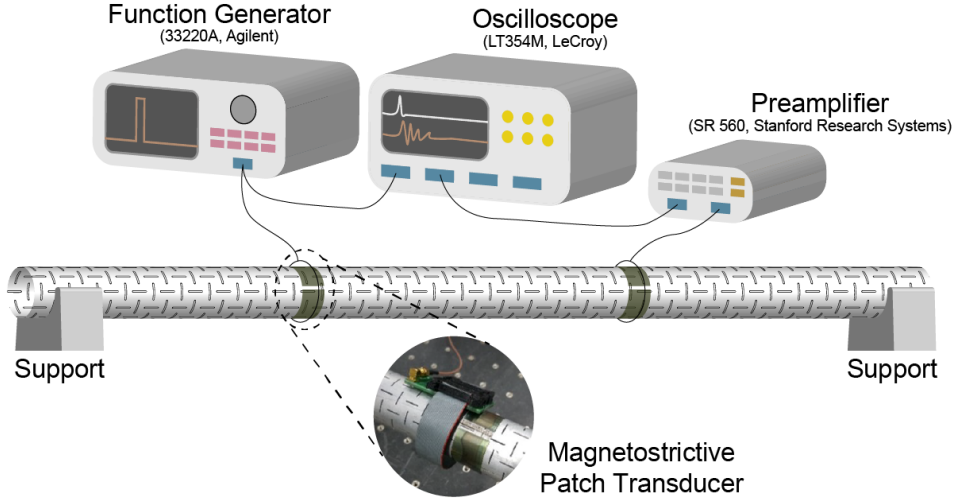


**Figure 3-10. Torsional modal test.** An auxetic meta-tube is positioned on the two supports placed at the end of the tube. At one-third and two-thirds points along the tube length, two magnetostrictive patch transducers are installed. One of them produces torsional impact and the other measures the signals.

In Table 3-1, we compared the numerical and experimental results of the modal frequencies. The numerically estimated frequencies ( $f_{B,FE}$  and  $f_{T,FE}$ ) can be calculated using Equations 16 and 17,

$$f_{B,FE} = \frac{\lambda_{n,b}\pi}{8L^2} \sqrt{\frac{EI}{\rho A}}, (\lambda_{n,B} = 3.011^2) \quad (16)$$

$$f_{T,FE} = \frac{1}{2L} \sqrt{\frac{GJ}{\lambda_{n,t}\rho J}}, (\lambda_{n,T} = 1) \quad (17)$$

where  $\rho$  denotes the density,  $A$  indicates the area of the cross-section, and  $\lambda_{n,B}$  and

$\lambda_{n,T}$  represent the constants for the first ( $n = 1$ ) bending and torsional mode, respectively. The experimental frequency results can also be converted to stiffness values using those equations.

Design case	1	2	3	4	5	6	7	8	9	10	11	12	13
HR	0.5	0.5	0.5	0.5	0.5	0.5	0.3	0.7	0.3	0.3	0.3	0.3	0.3
AR	$2^3$	$2^2$	$2^1$	$2^0$	$2^{-1}$	$2^{-2}$	$2^0$	$2^0$	$2^3$	$2^2$	$2^1$	$2^{-1}$	$2^{-2}$
$f_{B,FE}$ [Hz]	263	243	224	187	129	122	100	244	197	180	148	60	33
$f_{B,exp}$ [Hz]	250	250	229	185	135	106	101	240	164	190	133	51	28
$f_{T,FE}$ [Hz]	559	874	1049	1070	952	860	773	1343	384	621	765	735	625
$f_{T,exp}$ [Hz]	540	849	1039	1095	949	864	764	1364	355	655	773	736	636

**Table 3-1. Comparison of numerical and experimental result of the natural frequencies of auxetic meta-tubes.** The subscripts B and T indicate the bending and torsional modes, respectively, and FE and EXP denote the numerical and experimental data, respectively.

### **3.5. Design principle for simultaneous control of stiffness of auxetic meta-tube**

In this section, based on the mechanism analysis of the in-plane auxetic unit cell, we demonstrated a design principle for simultaneous control of bending and torsional stiffness of auxetic meta-tube. It was confirmed that a broadband controllability of the two stiffness can be accomplished by numerical and experimental verification. In the reachable stiffness range, independent control of one stiffness of the two can be possible and the design methodology for it and examples are provided.

#### **3.5.1. Bending stiffness (B) control**

When the auxetic tube is subjected to bending load, the auxetic deformation mode governs, and  $B^*$  consistently increases with both HR and AR (Figure 3-11). In this mode, rectangular subunits rotate rigid-likely around hinges, functioning as rotational springs, as represented with the axial stress distribution within the unit cell. As HR grows, these rotational springs become stiffened, enhancing the bending stiffness of the tube, as demonstrated in Figure 3-12a.

Using a larger AR causes the rectangular subunits of the unit cell to become taller along the tube axis. To achieve the same axial displacement, these taller subunits need to rotate more than their shorter counterparts, generating higher stresses around hinges (Figure 3-12b). Consequently, as AR increases, the unit cell becomes stiffer, making the bending stiffness of the tube increasing.



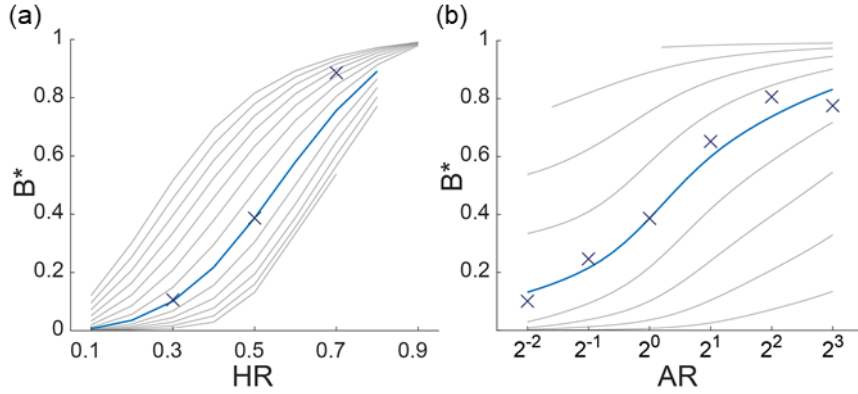


**Figure 3-11. Adjustment of bending stiffness of auxetic meta-tube.** Each curve represents a constant the other design variable. (a) HR variations, and (b) AR variations. X-markers denote the experimental results, and the color curve indicate the corresponding numerical results.

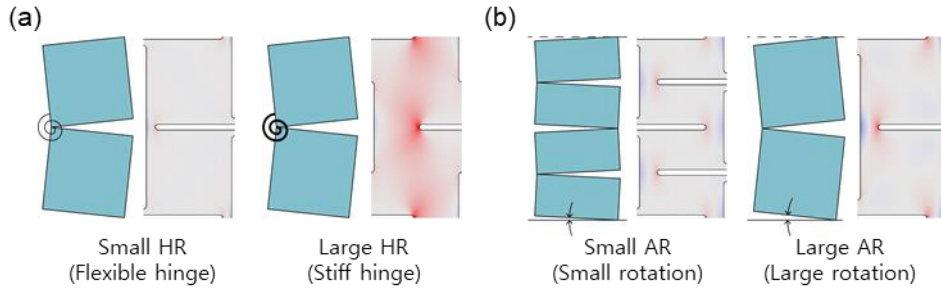


**Figure 3-12. Schematics and normal stress distribution with the change in design variables.** (a) HR variations, and (b) AR variations. High level of stress occurs in the large HR unit cell and in the large AR unit cell.

### 3.5.2. Torsional stiffness (C) control

The torsional stiffness variation according to the change in the design variables is different from the bending case, since the non-auxetic deformation mode is dominant in torsion. Under torsion, rectangular subunits primarily undergo shear deformation rather than rigid-body-like rotation. This shear deformation of subunits

appears easier in the unit cells with longer slits (or smaller HR values), resulting in larger HR values increasing the shear stiffness  $C^*$ , as shown in Figure 3-13a. The in-plane shear stress distribution in the unit cell also verifies this (Figure 3-14a).

However, the relationship with AR is non-monotonic.  $C^*$  is the maximum value when subunits are square ( $AR = 2^0$ ) and decreases as AR goes further from  $2^0$ , as shown in Figure 3-13b. The reason of this arises from the fact that the shear deformation of subunits is closer to the bending of a beam, rather than a pure shear of a planar material, as evidenced by the shear stress distribution. The subunits are more flexible near free edges formed by slits than around hinges. As the force required for a given flexural shear deformation decreases with the increase of slenderness of subunits (Figure 3-14b), the tube exhibits the maximum torsional stiffness in the case of the square subunit.

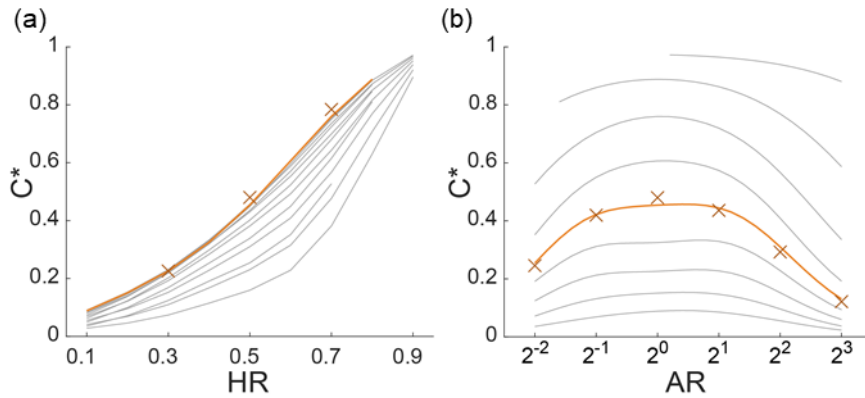


**Figure 3-13. Adjustment of torsional stiffness of auxetic meta-tube.** Each curve represents a constant the other design variable. (a) HR variations, and (b) AR variations. X-markers denote the experimental results, and the color curve indicate the corresponding numerical results.

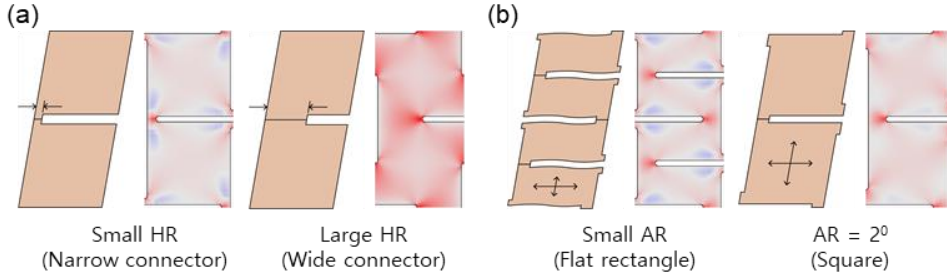


**Figure 3-14. Schematics and shear stress distribution with the change in design variables.** (a) HR variations, and (b) AR variations. High level of stress occurs in the large HR unit cell and in the unit cell of AR equal to  $2^0$ .

### 3.5.3. Designable stiffness area

Figure 3-15 shows the stiffness design area, with the horizontal and vertical axes representing normalized torsional and bending stiffness, respectively. As depicted in the figure, a wide variety of bending and torsional stiffness values can be achieved using auxetic patterns. The upper-left region, where bending stiffness is greater than torsional stiffness, is almost completely covered. However, the lower-right area is partially populated. This is due to the fact that torsional stiffness reaches its maximum value when  $AR = 2^0$ , while bending stiffness increases with AR in a monotonic manner. Consequently, it is simple to create a tube with  $B^*/C^* > 1$  but challenging to reach the area of  $B^*/C^* < 1$ . The lower boundary of the designable area can be bounded by the points of AR equal to  $2^{-1}$ , where constant HR lines (solid lines in Figure 3-15) experience deflection. Nonetheless, within the feasible range, tube stiffness values can be fully controlled.

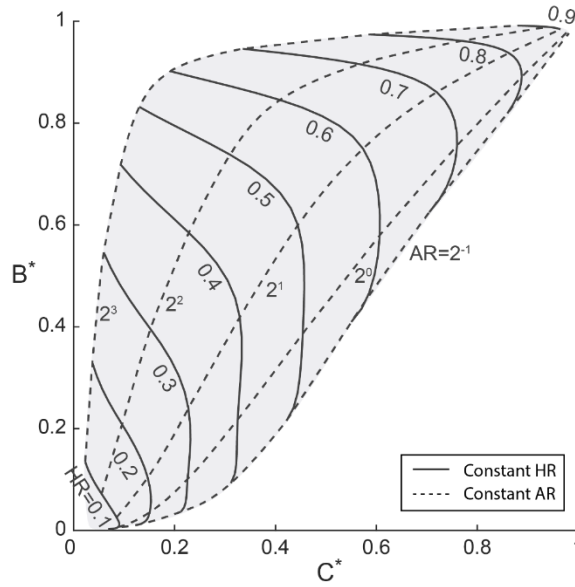


**Figure 3-15. Designable tube stiffness area.** Solid and dotted lines represent the constant HR and AR values, respectively. A wide designable stiffness area is achieved.

### 3.5.4. Independent stiffness control

In the designable stiffness area, both bending and torsional stiffness can be adjusted freely. An independent stiffness control can also be possible, which control one stiffness while the other stiffness is constant. Figures 3-16a and 3-17a show the bending and torsional stiffness contour according to the set of the design variables. When the tube properties of a constant bending stiffness ( $B^*$ ) and adjustment of torsional stiffness ( $C^*$ ) are required, we can easily find corresponding design variables. The examples of auxetic meta-tube for constant  $B^*$  are illustrated in Figure 16b. In order to design a higher torsional stiffness of meta-tube, the upper-left part of the set of design variables would be desirable. For a constant torsional stiffness while bending stiffness is required to be changed, an appropriate set of the design variables could be selected referring the  $C^*$  contour. Several examples are shown in Figure 17b. The upper-right parts in the contour corresponds to higher bending

stiffness.

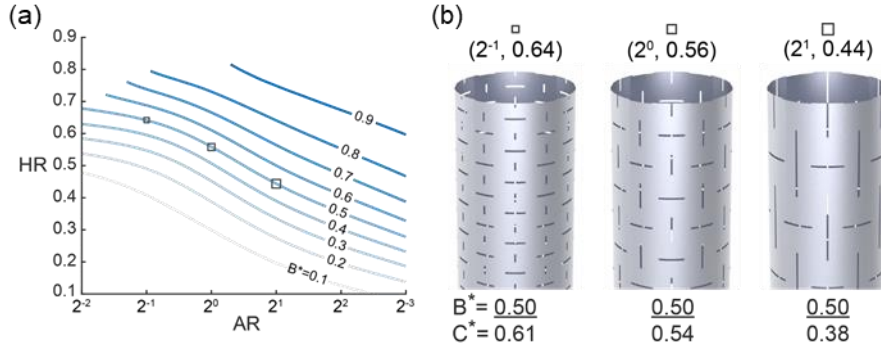


**Figure 3-16. Independent torsional stiffness control.** (a) Bending stiffness contour, and (b) the examples of meta-tube designs, where the bending stiffness values are constant but the torsional stiffness values vary.

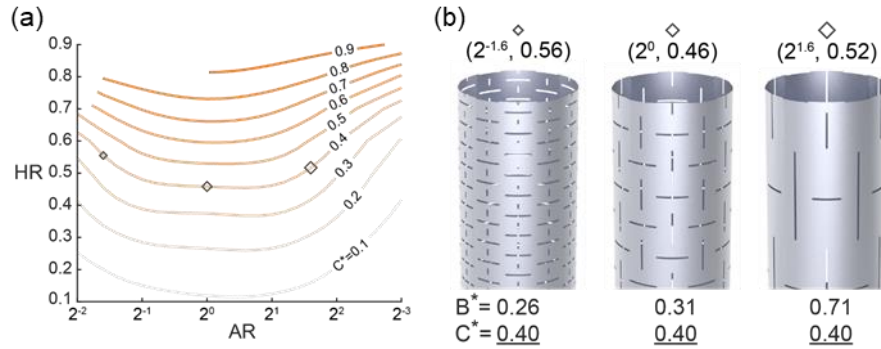


**Figure 3-17. Independent bending stiffness control.** (a) Torsional stiffness contour, and (b) the examples of meta-tube designs, where the torsional stiffness values are constant but the bending stiffness values vary.

### 3.6. Results with triangular and hexa-triangular pattern

The proposed design principle can be applied to other rotating rigid auxetic pattern. We represent a triangular rotating rigid unit and a hexa-triangular rotating rigid unit to demonstrate the generality of applying load-dependent deformation modes. This section includes the definition of the two unit cells, feasible stiffness area obtained with FE analysis, and independent stiffness control examples.

#### 3.6.1. Definition of triangular and hexa-triangular unit cell

One triangular unit cell is composed by eight triangular subunits and one hexa-triangular unit cell is constituted by one hexagonal and two triangular subunits (Figure 3-18). The unit cells are circumferentially arranged to form a unit layer, and the layers are stacked along the axial direction of tube.

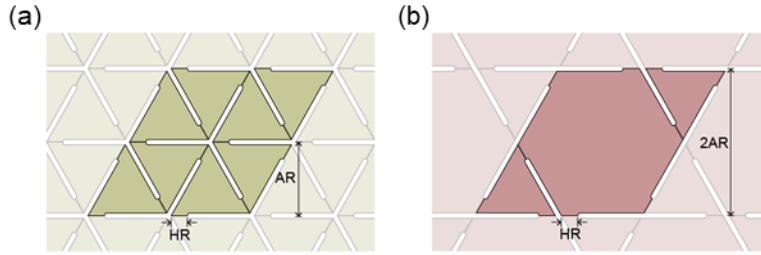


**Figure 3-18. Triangular and hexa-triangular rotating rigid unit cell.** Eight triangular subunits compose (a) triangular unit cell, and two triangular and one hexagonal subunits constitute (b) hexa-triangular unit cell. Two design variables, HR and AR, define the unit cells. In both figures, the unit length was assumed to be 1 for simplicity.

The design parameters of the unit cells are the same with the rectangular auxetic pattern: HR and AR. For convenience, the lateral width of a triangular subunit is assumed as 1 in this section. The actual width will be determined by the tube dimension. HR determines the thickness of hinges, and AR indicates the height of

the subunit as shown in Figure 3-18. Note that HR also determines the hinges at the legs of the triangles, so the thickness of the leg hinge is proportional to the leg length.

### 3.6.2. Stiffness control result

The stiffness control mechanisms in the auxetic and non-auxetic deformation modes of triangular patterns and hexagonal-triangular patterns are the same as those in the rectangular patterns. HR represents the stiffness of the rotational hinges in the auxetic deformation mode, while in the non-auxetic deformation mode, it signifies the length of the connector. AR determines the rotation angles of polygons in the auxetic deformation mode, and in the non-auxetic deformation mode, it decides whether the deformation shape is bending-like shear or continuum-like shear. A similar range of stiffness control areas can be achieved with both patterns, and within this area, independent stiffness design is also possible. Figures 3-19, 3-20, 3-21, and 3-22 show the bending and torsional stiffness contours for triangular and hexagonal-triangular patterns, respectively, as well as examples of auxetic meta-tubes with independently designed stiffness.



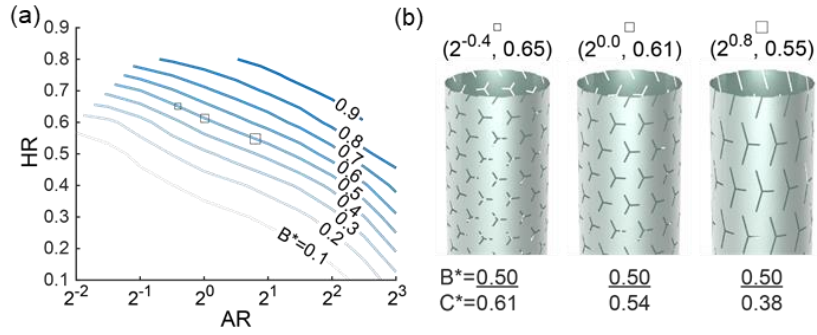


**Figure 3-19. Independent torsional stiffness control with triangular pattern.**

(a) Bending stiffness contour, and (b) the examples of triangular pattern meta-tube designs.

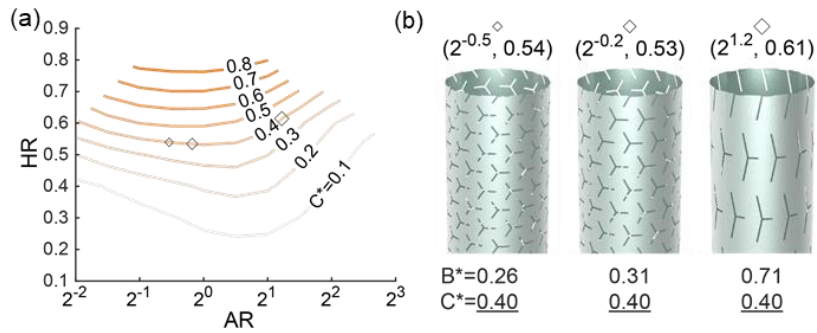


**Figure 3-20. Independent bending stiffness control with triangular pattern. (a)**

Torsional stiffness contour, and (b) the examples of triangular pattern meta-tube designs.

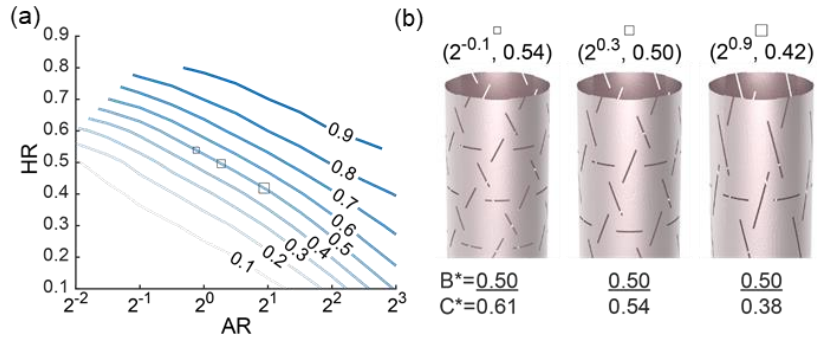


**Figure 3-21. Independent torsional stiffness control with hexa-triangular pattern.** (a) Bending stiffness contour, and (b) the examples of hexa-triangular pattern meta-tube designs.

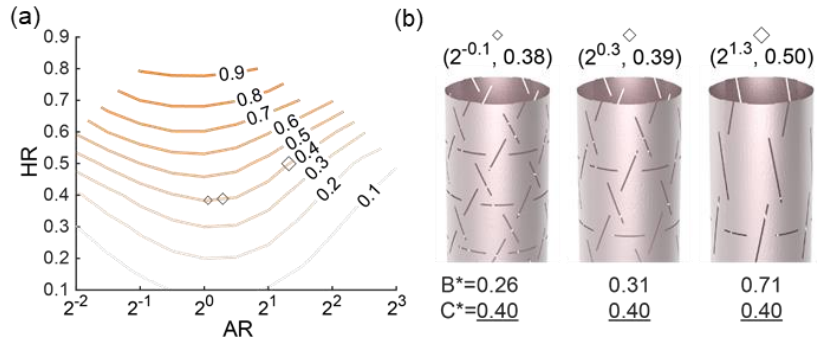


**Figure 3-22. Independent bending stiffness control with hexa-triangular pattern.** (a) Torsional stiffness contour, and (b) the examples of hexa-triangular pattern meta-tube designs.

### 3.7. Results with tilted rectangular patterns

Using a 45-degree tilted pattern allows for creating different stiffness variations while utilizing the distinct deformation modes of the auxetic pattern, as discussed in Section 2.5.3. The 45-degree tilted auxetic meta-tube can be created by arranging tilted unit cells along a 45-degree inclined axis to form a unit helix, which is then arranged in a tube form, as shown in Figure 3-23.

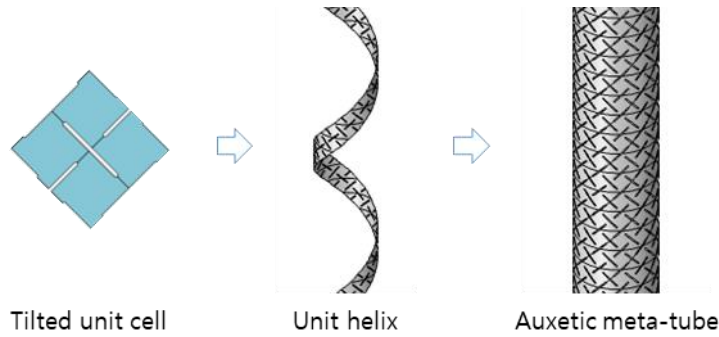


**Figure 3-23. Construction of auxetic meta-tube with tilted auxetic unit cell.**

One important consideration when forming the helix into a tube is to consider the connectivity between the hinges of the auxetic pattern. For example, with an AR value of  $2^{-2}$ , the connectivity between helices is not secured, and a complete tube form cannot be constructed, as shown in Figure 3-24. In this study, it was decided to arrange six unit cells (twelve subunits) in the circumferential direction. Thus, the study proceeded with three AR values ( $2^{-1}$ ,  $2^0$ ,  $2^1$ ) that allow for normal connection between the hinges when arranging six helices (Figure 3-25).

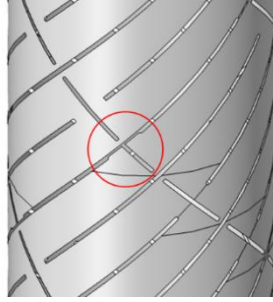


**Figure 3-24. Uncontinuity of hinges.**

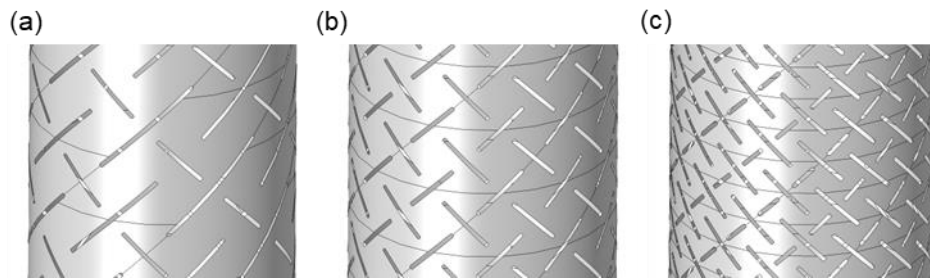


**Figure 3-25. Auxetic meta-tube with 45-degree pattern.** (a)  $AR = 2^{-1}$ , (b)  $AR = 2^0$ , and (c)  $AR = 2^1$ .

The next Figure 3-26 shows the results of calculating the bending and torsional stiffness of the tilted pattern auxetic meta-tube through simulation. Similar to the results of Section 2.5.3, the two stiffness values monotonically increase with HR, and for AR, both stiffness values change symmetrically, centered around AR=1.

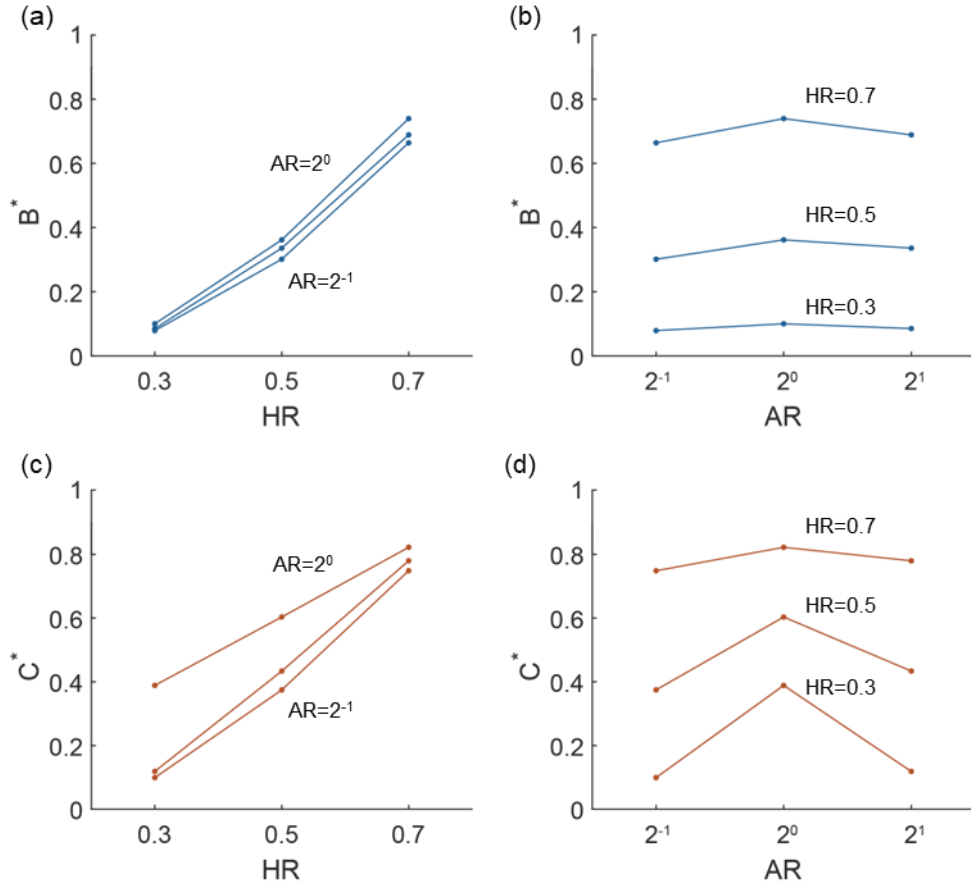


**Figure 3-26. Normalized bending and torsional stiffness adjustment of 45-degree pattern.** The bending stiffness adjustment according to the variation of (a) HR and (b) AR, and the torsional stiffness adjustment according to the variation of (c) HR and (d) AR.

The two dimensionless stiffness values of the tilted pattern are shown in Table 3-2. The stability criteria of the tube robot, the  $B^*/C^*$  value, can also be seen in the table. Considering that the minimum  $B^*/C^*$  value is 0.173 ( $AR = 2^{-1}$ ,  $HR = 0.3$ ) for the same range of the design variables, it would be more appropriate to use the original pattern from the aspect of the stiffness ratio.

	$B^*$			$C^*$			$B^*/C^*$		
HR/AR	$2^{-1}$	$2^0$	$2^1$	$2^{-1}$	$2^0$	$2^1$	$2^{-1}$	$2^0$	$2^1$
0.3	0.079	0.301	0.664	0.099	0.375	0.749	0.795	0.805	0.887
0.5	0.100	0.362	0.740	0.389	0.603	0.822	0.257	0.599	0.900
0.7	0.085	0.336	0.689	0.119	0.434	0.780	0.718	0.775	0.883

**Table 3-2. Normalized tube stiffness and stiffness ratio.**

### 3.8. Conclusion

In this chapter, based on the design principle of planar auxetic unit cells for simultaneous control of tensile and shear stiffness, we designed auxetic meta-tubes capable of controlling the bending and torsional stiffness of tubular structures. The results of analysis and experiments showed that tube stiffness can be controlled simultaneously in a wide range and that each tube stiffness can be freely designed within the designable area. By demonstrating that the same stiffness control mechanism can be implemented using various patterns, including rectangular, triangular, and hexa-triangular patterns, we confirmed that the application of load-dependent deformation modes has broad generality.

The research findings of this chapter can improve the stability of concentric tube robots in the field of minimally invasive surgery. By expanding the concept, it may enable the design of meta-structures capable of simultaneously controlling the stiffness of two structural components in shapes other than tubular structures (such as plates and shells) by applying the same stiffness control principles. In this study, we covered a linear problem assuming small displacements, but the applicability of the research can be expanded through follow-up studies on the nonlinear stiffness of auxetic meta-tubes.

## **Chapter 4. Simultaneous control of elastic wave propagation: Auxetic meta-disk**

### **4.1. Introduction**

In this chapter, we present the second meta-structure design using the load-dependent deformation modes of auxetic patterns, which is an auxetic meta-disk capable of simultaneously controlling the elastic wave propagation of bending and torsion modes in pipes.

One of the methods to control the propagation and blocking of elastic waves is to form a bandgap, a frequency region where waves do not propagate, through the design of metamaterials. The formation of bandgaps mainly occurs through two mechanisms: phononic crystals that use Bragg scattering by periodically arranging metamaterial unit cells, and locally resonant structures that use resonance within the metamaterial unit cells. The phononic crystal (PC) method utilizes the periodicity of unit cells, making it difficult to form bandgaps in the low-frequency range. However, the locally resonant (LR) method has the advantage of being able to control wave propagation characteristics in the low-frequency range because bandgaps form near the resonant frequency of locally resonant structures.

Since the introduction of the first locally resonant elastic metamaterial, which consisted of coated lead spheres<sup>36</sup>, numerous studies have focused on the formation of bandgaps in elastic metamaterials to manipulate elastic waves and vibrations in structures. Among these studies, significant attention has been devoted to wave propagation in slender structures like beams and pipes due to their wide-ranging applications. Analytical approaches have been employed to investigate the propagation of flexural wave in beams with periodic spring-mass resonators using the Euler-Bernoulli beam<sup>37-39</sup> and Timoshenko beam<sup>40-42</sup>. Furthermore, studies have explored longitudinal and torsional wave propagation<sup>43,44</sup>. These works revealed that



the resonant-based bandgap emerge near the natural frequency of the local resonators. Beyond the primary spring-mass local resonator, recent research has proposed intriguing designs to achieve unique properties of local resonators. For instance, an X-shaped local resonator with an internal spring that exhibits variable stiffness at different frequencies was employed to attenuate flexural waves<sup>45</sup>. Local resonators with quasi-zero stiffness were utilized to create extremely low-frequency bandgaps for flexural waves in a beam<sup>46</sup>. A metamaterial beam with periodically changing cross-sections was investigated to generate broadband flexural bandgaps by combining the mechanisms of Bragg scattering and local resonance<sup>47</sup>. Additionally, an origami resonator was proposed to control torsional bandgaps<sup>48</sup>.

A majority of prior studies focused on elastic metamaterials functioning where only a single wave mode is present. However, in real-world engineering applications, such as robot arms, airfoils, and pipe systems containing fluid, it is crucial to consider situations where two or more wave modes occur simultaneously. The inherent coupling of dynamic properties in resonant structures, as determined by material properties and structural configuration, poses a challenge to designing metamaterials that can effectively handle multiple wave modes simultaneously.

The load-dependent deformation mechanism may have the potential to adjust the two natural frequencies in the flexural and torsional modes of a local resonator. Considering the resonance of disk-shaped local resonators attached to a pipe, the mode shapes of the two modes manifest as depicted in Figure 4-1. In the flexural mode, the unit cells in the disk oscillate entirely in the normal direction, while the unit cells experience shear deformation in the torsional vibration. At this point, we can implement the load-dependent deformation modes of auxetic patterns by arranging the auxetic pattern into a disk structure, thus creating an auxetic meta-disk. The flexural and torsional natural frequencies can be fine-tuned using auxetic deformation and non-auxetic deformation modes, respectively.

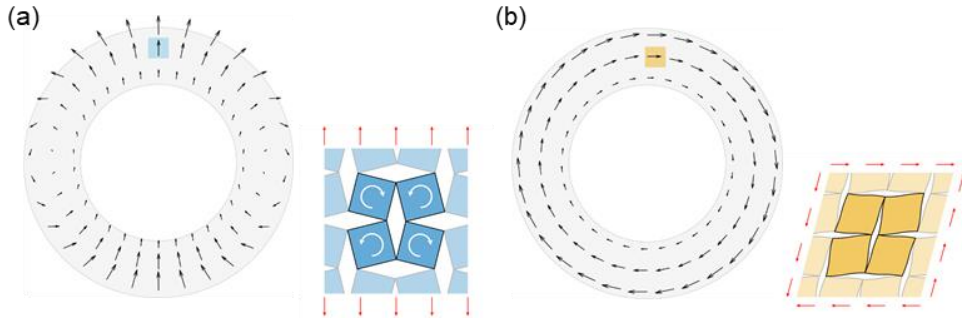


**Figure 4-1. Utilizing load-dependent deformation modes in vibration of disk structure.** The displacement fields of the flexural and torsional mode shapes of a disk structure are illustrated with quivers. Each colored square in the mode shapes denotes the unit cell showing its deformation type.

From this point, a background theory for bandgap generation in a bar with local resonant structures are introduced, and the design principle to manipulate the flexural and torsional wave propagation is present. It was discovered that the two frequencies could be designed in a wide range, and the bandgap for each mode was generated at those frequencies. We utilized finite element analysis to verify the results which confirms that wave transmission was significantly reduced in the bandgaps. Additionally, an application of elastic wave mode-filtering is proposed.

## 4.2. Auxetic meta-disk

In this chapter, we present the definition of auxetic meta-disk unit cell and the composition of the auxetic meta-disk by arranging the unit cells. The difference between the unit cells of in-plane, meta-tube, and meta-disk is also present, because the unit cell should be modified to be applied to auxetic meta-disk to form a disk shape. The main design variables in the definition of the auxetic meta-tube are the hinge thickness ratio (HR) and the aspect ratio (AR).

### 4.2.1. Definition of auxetic meta-disk

In Figure 4-2, the process of constructing an auxetic meta-disk is demonstrated. To create an auxetic meta-disk, the fundamental rotating rigid auxetic unit cell needs to be transformed. We designed an auxetic unit sector by vertically placing two auxetic unit cells and giving it a tapered shape. A unit sector consists of eight similarly shaped subunits, which are radially scaled down. These unit sectors are then arranged circumferentially to fill the entire disk. A host pipe, which is the target for wave manipulation, has several meta-disks placed on it.

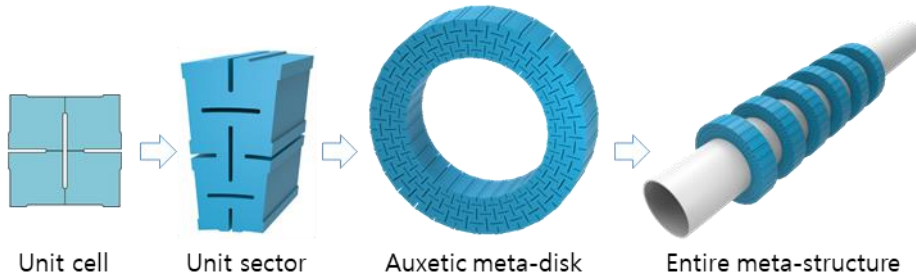


**Figure 4-2. Auxetic meta-disk composition.** Two auxetic unit cell form a unit sector, which is arranged circumferentially to establish an auxetic meta-disk. The auxetic meta-disks are placed on a host pipe to form the entire meta-structure.

Two design parameters define the subunit geometry: hinge thickness ratio (HR) and aspect ratio (AR). HR indicates the hinge thickness of the unit cell in the circumferential direction ( $t_c$ ) divided by the outer perimeter ( $c$ ). HR also determines the hinge thickness in the radial direction ( $t_h$ ) divided by the subunit height ( $h$ ) for simplicity. AR represents the aspect ratio which is defined by the height ( $h$ ) divided by the outer circumferential length of the subunit ( $c$ ). The dimension for the design variables is shown in Figure 4-3. We utilized normalized design parameters to apply the design principles into applications regardless of their scale.

We set constant inner and outer radii of the disk. Therefore, the unit cell height ( $h$ ) is a constant value, and the change in the design parameter AR determines only the outer perimeter of the unit cell ( $c$ ) and the number of unit cells in the circumferential direction. To fill the circumference without any gaps, AR must be determined by the condition where the number of unit cells in the circumferential direction should be a natural number.

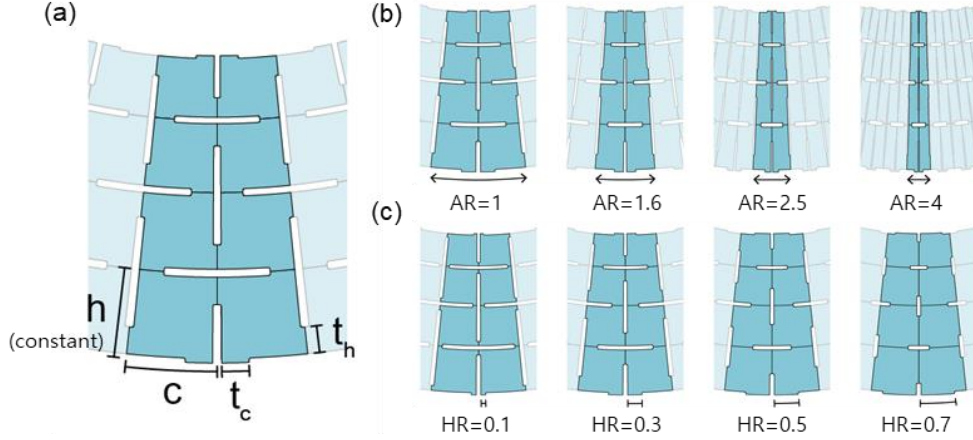


**Figure 4-3. Definition of auxetic meta-disk.** (a) Dimensions for the definition, the unit cell variation by the change in (b) AR, and (c) HR. Note that the height of a subunit ( $h$ ) is set constant, so the circumferential length of the unit cell decreases as AR increases.

#### 4.2.2. Study for other design variables

The actual number of the design variables in auxetic meta-disk is a seven: for disk dimensions, including the outer and inner radii and disk width, and for auxetic pattern geometry parameters, including aspect ratio (AR), hinge thickness ratio (HR), slit thickness ratio (SR), and the number of unit cells in the radial direction ( $n_r$ ). The outer and inner radii of the auxetic disk are set at 275 mm and 177.8 mm, respectively, with a width of 127 mm. The two primary design variables, AR and HR, are defined by the height and hinge thickness of the rectangular subunits divided by the circumferential length, respectively. SR, the ratio between the slit thickness and the circumferential length, has a fixed value of 0.1. The number of unit cells in the radial direction ( $n_r$ ) is selected as 4.

The aspect ratio AR determines the number of unit cells in the circumferential direction ( $n_c$ ), which must be a natural number to fill the entire disk circumference. For convenience, AR values are notated with an interval of 0.4 in the exponent of 2, however, the actual AR values ( $AR_a$ ) are smaller than the notated AR and are the largest appropriate values, as shown in Table 4-1.

AR	$2^{-1.6}$	$2^{-1.2}$	$2^{-0.8}$	$2^{-0.4}$	$2^0$	$2^{0.4}$	$2^{0.8}$	$2^{1.2}$	$2^{1.6}$	$2^{2.0}$
$AR_a$	$2^{-1.605}$	$2^{-1.342}$	$2^{-0.927}$	$2^{-0.467}$	$2^{-0.020}$	$2^{0.395}$	$2^{0.774}$	$2^{1.161}$	$2^{1.597}$	$2^{1.980}$
$n_c$	20	24	32	44	60	80	104	136	184	240

**Table 4-1. Notated, actual AR values and corresponding the number of the unit cell in circumferential direction,  $n_c$ .**

### **4.3. Finite element analysis model**

We conducted finite element analysis using COMSOL Multiphysics® 5.4, a commercial multiphysics simulation software, to confirm the variations of the elastic wave propagation characteristics. We performed three kinds of analysis: normal mode analysis to obtain the natural frequency of the meta-disks; dispersion analysis to investigate the bandgap formation; and transmission analysis to verify transmission of wave in bandgaps. This chapter contains the information of analysis model, boundary conditions, and the validity of the results of analyses.

#### **4.3.1. Analysis model**

We adopted polyurethane as the material for the disk in our analysis, considering its Young's modulus, density, and Poisson's ratio as 38.4 MPa, 1200 kg/m<sup>3</sup>, and 0.48, respectively. To minimize computational costs, we employed a sector model comprised of a single unit of the auxetic meta-disk sector, as depicted in Figure 4-4. The sector model featured cyclic symmetry conditions at the two boundary surfaces, highlighted in red, assuming circumferential periodicity. At those area, phase shifts were imposed based on the sector angle of the model. To discretize the analysis model, we utilized 3D ten-node tetrahedral elements, employing a finer mesh size near the end of the slits. The mesh resolutions are visually presented in Figure 4-4c.

#### **4.3.2. Normal mode analysis**

To determine the natural frequencies of the auxetic meta-disks, a normal mode analysis was conducted. Fixed boundary conditions were applied to the inner surfaces (highlighted in green in Figure 4-4a), assuming the meta-disks were mounted on a host pipe. The natural frequencies of the meta-disks were normalized by dividing them by the corresponding values of a solid disk without any pattern but

with identical dimensions. These normalized natural frequencies, denoted as  $f^*$ , were calculated using the equation  $f^* = f_{\text{meta}}/f_{\text{solid}}$ . In this study, the values of  $f_{\text{solid}}$  were found to be 525 Hz and 202 Hz for flexural and torsional modes, respectively.

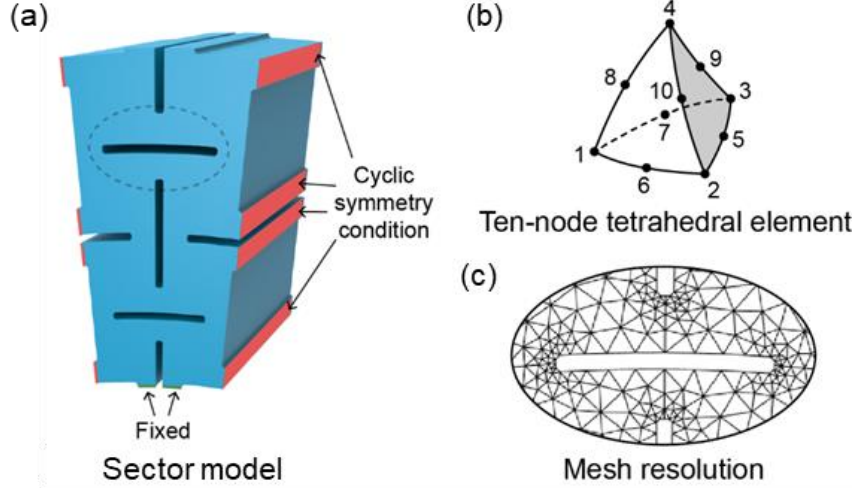


**Figure 4-4. FE model for normal mode analysis.** (a) Finite element model of the auxetic meta-disk sector, (b) ten-node tetrahedral element, and (c) resolution of the mesh. At the red-colored faces in both sides, cyclic symmetry condition is applied, and the inner faces are constrained.

#### 4.3.3. Validity of sector model

For analysis with the sector model, a cyclic boundary condition that imposed phase shift and rotation of displacements to the nodes of the source and destination surfaces was applied. The following condition was assumed as shown in Equation 18,

$$u_{dst} = Ru_{src}e^{-im\theta_s} \quad (18)$$

where  $u_{src}$  and  $u_{dst}$  indicate the displacement field of the source and destination boundary surfaces, respectively;  $R$  represents the rotation matrix for a given sector

angle;  $\theta_s$  represents the sector angle; and  $m$  is the mode number in the azimuthal direction. For a torsional mode,  $m$  must be set to zero, and for a flexural mode, it should be set to one. Figure 4-5 displays the mode shapes and the natural frequencies of the full and the sector model of the auxetic disk. Little difference in the natural frequencies was observed, which confirms that employing the sector disk model is appropriate to utilize the sector model instead of the full model.

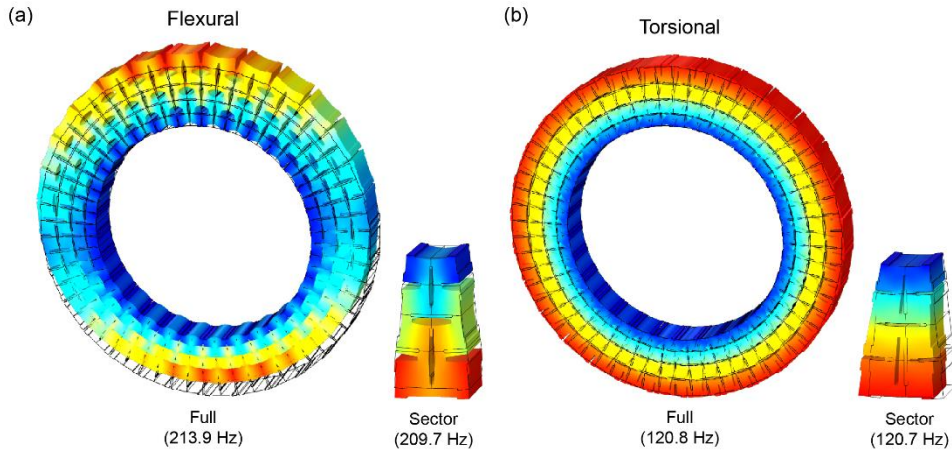


**Figure 4-5. Mode shapes and natural frequency comparison between the full disk model and the sector disk model.** The normalized total displacement distribution is plotted. The natural frequencies of the full and the sector models are almost coincident which ensures the validity of the usage of the sector model.

#### 4.3.4. Dispersion analysis

To analyze the band structures, a concentric aluminum pipe was introduced. The pipe had a thickness, length, Young's modulus, density, and Poisson's ratio of 10 mm, 254 mm, 70 GPa, 2700 kg/m<sup>3</sup>, and 0.33, respectively. Since we considered one-dimensional wave propagation, specifically flexural and torsional wave propagation in a pipe, the wave vector could be expressed as a scalar, known as the wave number. Floquet boundary conditions were imposed on the front and back surfaces of the host sector (indicated in pink in Figure 4-6), introducing a phase shift  $\phi$ . The wave number



( $k$ ) was determined by dividing the phase shift  $\phi$  by the unit pipe length ( $a$ ), which was 254 mm. The phase shift was swept from zero to  $\pi$ . For the lower wave number range, from 0 to  $0.2\pi$ , we used fine increments (40 increments) to clearly distinguish the dispersion curves, and for the left range, from  $0.2\pi$  to  $\pi$ , large increments (16 increments) were employed. The total number of increments is 57, including zero. The resulting eigen-frequencies for each increment of  $k$  constituted a band structure.

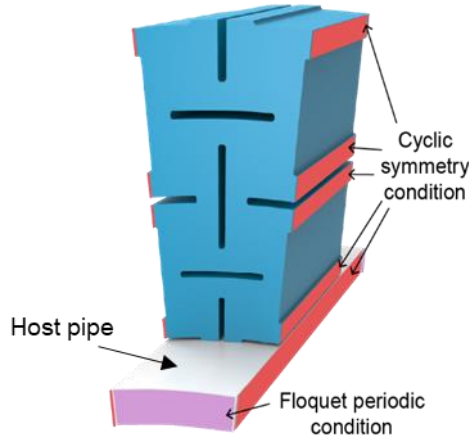


**Figure 4-6. FE model for dispersion analysis.** The sector model of auxetic meta-disk is attached on a sector host pipe. Floquet periodic boundary condition for dispersion analysis is applied at the pink-colored faces at the front and the back of the sector pipe.

Figure 4-7 represents the results of dispersion analysis for an example unit cell ( $HR = 0.3$  and  $AR = 2^0$ ) with a host sector. For an assigned wavenumber, we calculated six eigenfrequencies which were represented as points in Figure 4-7. Each point is corresponding to each mode shape. For example, for the wavenumber of  $0.2\pi$  rad/m, 3<sup>rd</sup> mode represents flexural mode and 4<sup>th</sup> mode denotes out-of-phase mode as shown in Figure 4-8. The points whose mode is the same are connected to form dispersion curves as shown in Figure 4-7b.

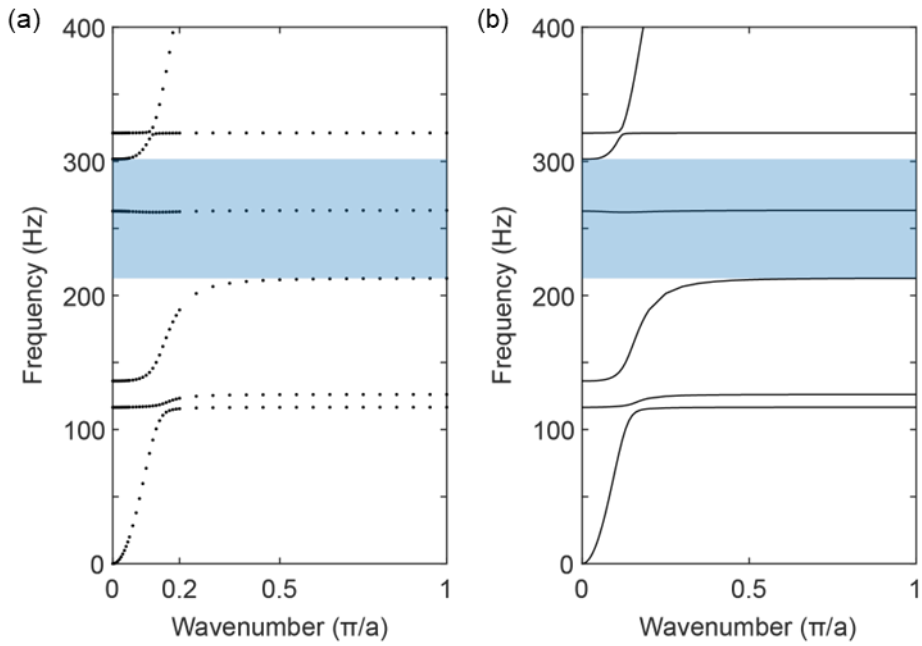


**Figure 4-7. Forming dispersion curves via dispersion analysis.** (a) The results of dispersion analysis are obtained as eigenfrequencies and corresponding mode shapes for a given wavenumber. (b) The points whose mode is the same are connected to draw dispersion curves.

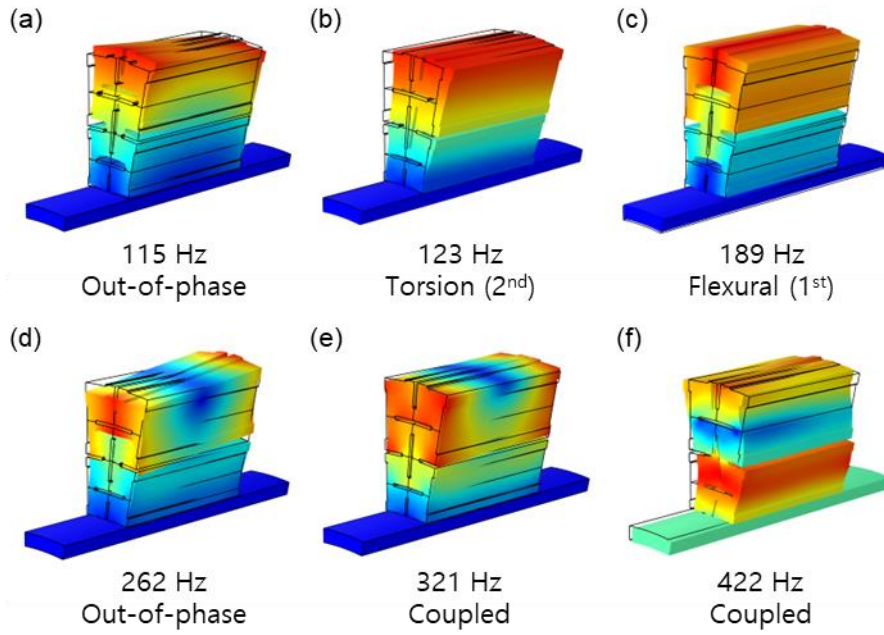


**Figure 4-8. Calculated mode shapes for an example wavenumber,  $0.2 \pi$  (rad/m).**

Each point which lies vertically is corresponding to each mode. (a) Out-of-phase mode, (b) 2nd torsional mode, (c) 1st flexural mode, (d) out-of-phase mode, (e) and (f) coupled mode. Note that the azimuthal mode number was set as one, so the mode shape of the entire disk has phase variance of  $2 \pi$  along to the circumferential direction.

#### 4.3.5. Transmission analysis

To investigate wave propagation inside or outside the bandgaps, we placed four to twelve auxetic meta-disks axially on the host pipe at intervals of unit length  $a$  (Figure 4-9) in the transmission analysis. We attached waveguides to both sides of the meta-structure and imposed perfectly matched layers (PMLs) which are artificial domains that perfectly absorb incident waves. We applied a small harmonic displacement  $w_1$  in the flexural and torsional directions at the excitation point in front of the meta-structure, and the amplitude  $w_2$  at the measurement point was obtained.

The distances of the excitation and measurement points from the meta-structure were  $a$  (254 mm) and  $2a$  (508 mm), respectively. The transmission value,  $T$ , was calculated with the equation of  $T = 20\log(w_2/w_1)$  (dB). It is defined by the amplitude at each points, so it can exceed unity without any violation in energy conservation<sup>49</sup>.

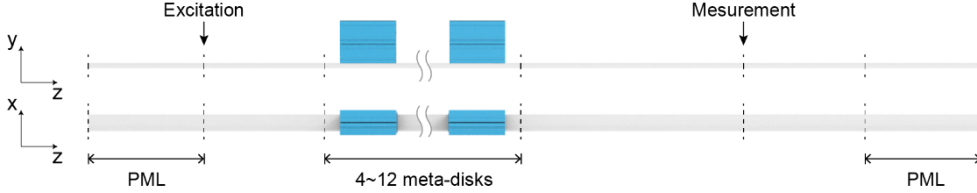


**Figure 4-9. FE model for transmission analysis.** From four to twelve auxetic meta-disks with the host pipe are arranged. Waveguides are attached at the front and back of the meta-disk array. At the end of the waveguides, perfectly matched layer (PML) was applied to inhibit reflected wave.

#### 4.3.6. Mesh convergence test

We conducted a parametric study for a minimum mesh size of a 3D auxetic disk sector model to ensure a converged solution. A static analysis was performed, where the inner surfaces of the auxetic disk model are fixed and a small displacement in the y-direction is applied at the outer surfaces of the auxetic disk. The resulting reaction forces were compared, while varying the minimum mesh size of the FE model. The smallest slit of the innermost subunit of an auxetic disk unit cell was used to set the minimum mesh size as the slit thickness multiplied by a variable  $\gamma$ . The solution variations according to the value of  $1/\gamma$  and the number of elements are plotted in Figure 4-10, indicating that  $\gamma = 1$  and 1.87 million elements are sufficient to ensure a converged solution, as marked by the unfilled circle.

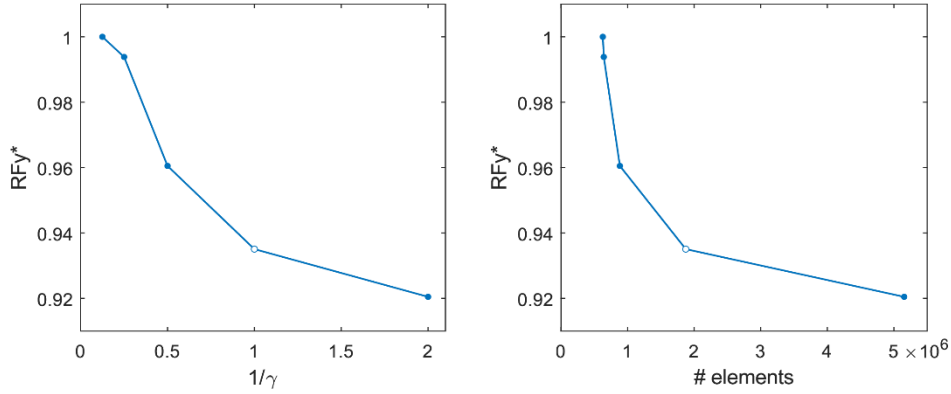


**Figure 4-10. Convergence test on the minimum mesh size.** The vertical and lateral axis represent the solution (reaction force) and  $1/\gamma$  and corresponding the number of the used elements.

#### 4.3.7. Mesh for perfectly matched layers

We applied perfectly matched layer (PML) condition to the left and right end of the entire meta-structure as shown in Figure 4-9. The perfectly matched layer is a domain to mimic an open or non-reflecting infinite domain. To achieve effective absorption of PMLs, finer mesh should be applied on those domains. It was known that at least 8 layers of mesh should be required inside PML.

We assigned rectangular mesh on the cross-section of the host pipe sector as shown in Figure 4-11a and swept them along the axial direction to form hexahedral elements. The maximum size of the rectangular mesh was set to be 0.3 mm, and the maximum swept size is 0.4 mm. The connecting part from the PMLs and the waveguide is the excitation point as shown in Figure 4-11b.

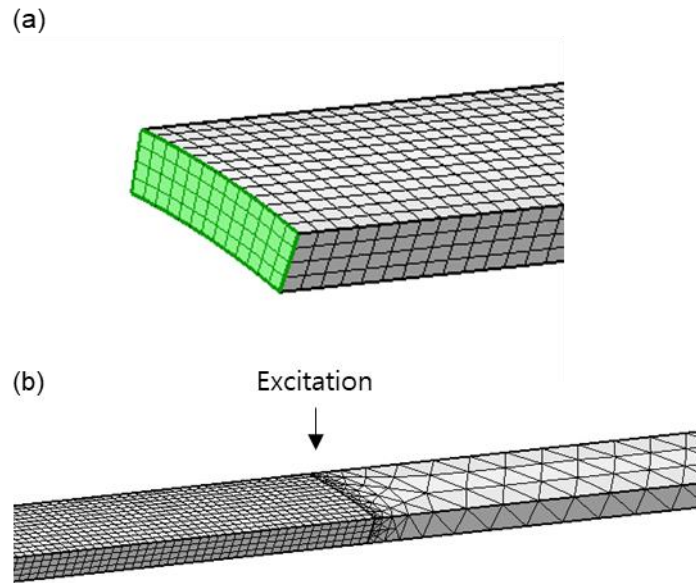


**Figure 4-11. Convergence test on the minimum mesh size.** The vertical and lateral axis represent the solution (reaction force) and  $1/\gamma$  and corresponding the number of the used elements.

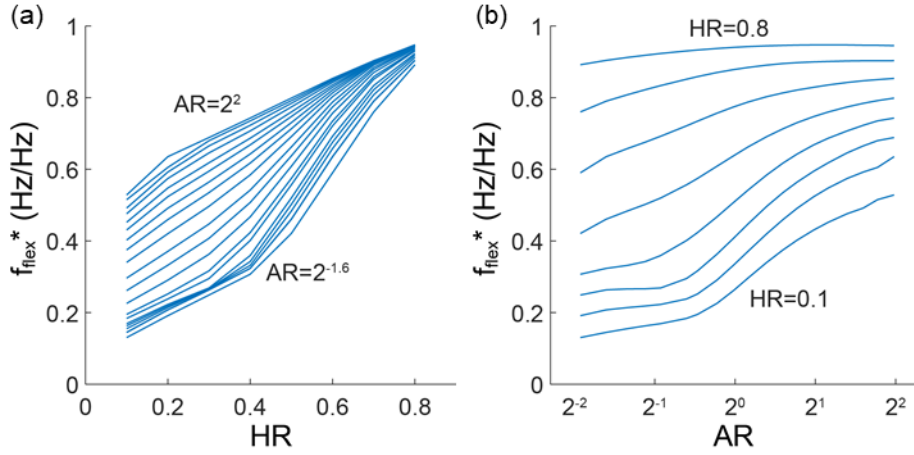
## 4.4. Design principle for simultaneous control of elastic wave propagation

Based on the result of the mechanism analysis for simultaneous adjustment of in-plane stiffness, we propose a design principle to control elastic wave propagation in the two modes, flexural and torsional modes. We performed a comprehensive parametric study whose ranges are from 0.1 to 0.8 with the interval of 0.1 for HR, and from  $2^{-1.6}$  to  $2^2$  with the interval of 0.2 in the exponent for AR. It was found that the natural frequencies of the disk could be tuned in a wide range. We confirmed that the bandgaps were opened at the corresponding natural frequencies by the dispersion analysis result.

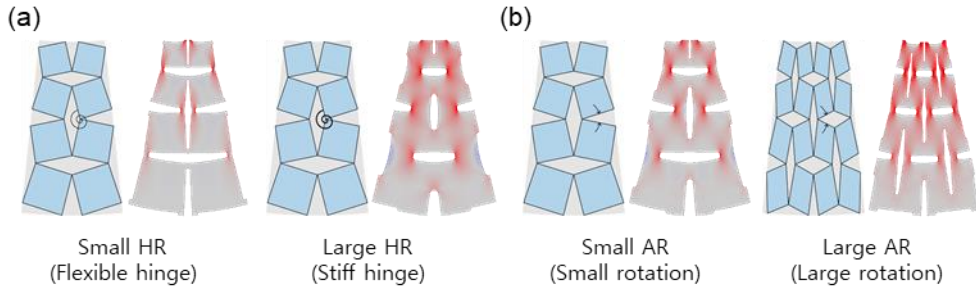
### 4.4.1. Flexural mode natural frequency control

Figure 4-12 illustrates the variations in normalized flexural natural frequencies ( $f_{\text{flex}}^*$ ) as the two design parameters change. The impact of these design parameter changes on the natural frequency was examined from a stiffness perspective, considering the mass change to be negligible, which will be discussed later. Therefore, stiffness plays a dominant role in determining the natural frequency, and an auxetic meta-disk design with higher flexural or torsional stiffness exhibits a higher natural frequency in the corresponding mode.

In the case of flexural vibration, where auxetic deformation primarily occurs in the auxetic unit cell, the flexural natural frequency increases with both HR and AR, as depicted in Figure 4-12. In this mode, the auxetic unit cell is assumed to consist of rotating rigid rectangles interconnected by rotational springs. A higher HR value corresponds to a stiffer spring, while a larger AR implies a larger number of rectangles occupying a fixed area, requiring a greater rotation angle for a given displacement. The stress distribution shown in Figure 4-13 confirms the higher stress levels observed in cases with larger HR and AR values. These effects contribute to an increased flexural natural frequency of the auxetic meta-disk.



**Figure 4-12. Adjustment of flexural natural frequency of auxetic meta-disk.** Each curve represents a constant the other design variable. (a) HR variations, and (b) AR variations. As HR and AR values increase, the flexural natural frequencies increase.



**Figure 4-13. Schematics and radial stress distribution with the change in design variables.** (a) HR variations, and (b) AR variations. Higher level of stress occurs when HR and AR increase.

#### 4.4.2. Torsional mode natural frequency control

The variation in the normalized torsional natural frequency ( $f_{\text{tor}}^*$ ) with changes in the two design parameters is presented in Figure 4-14. In the case of torsional vibration, non-auxetic deformation is predominant in the deformed configuration,



where all constituents of the unit cell deform as a continuous structure. The hinges lose their function as rotational springs and act as connectors, and the sub-rectangles are not assumed to be rigid. This mechanism is distinct from auxetic deformation. The stress fields depicted in Figure 4-15a confirm the wide distribution of shear stress in the unit cell. Increasing the HR lengthens the connector, leading to a higher torsional resonating frequency (Figure 4-15a).

However, AR affects torsional stiffness in a distinct manner, where the slenderness of the rectangles plays a crucial role in determining the natural frequency. In a partially connected unit cell, the square shape exhibits the highest stiffness, while the unit cell becomes more flexible as the shape becomes flatter or longer. Therefore, the maximum torsional frequency is achieved when AR is 1 (equal to  $2^0$ ), and it decreases as AR increases or deviates from 1, as shown in Figure 4-14b. The shear stress distribution confirms that the unit cell with a square shape (Figure 4-15b) is stiffer compared to the unit cell with higher AR values.

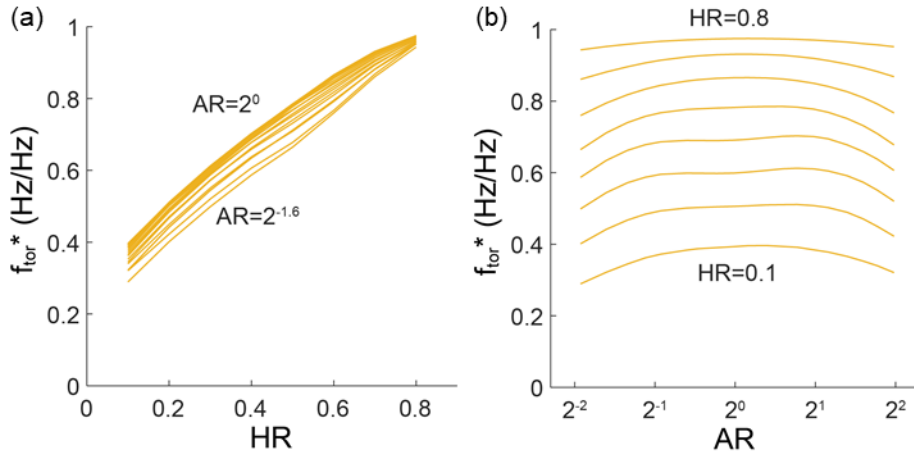


**Figure 4-14. Adjustment of torsional natural frequency of auxetic meta-disk.**

Each curve represents a constant the other design variable. (a) HR variations, and (b) AR variations. As HR increase and AR is closer to  $2^0$ , the torsional natural frequencies increase.

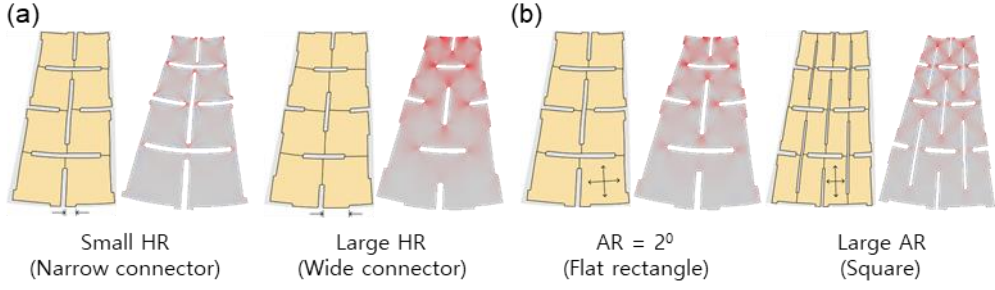


**Figure 4-15. Schematics and shear stress distribution with the change in design variables.** (a) HR variations, and (b) AR variations. Higher level of stress occurs when HR increase or AR is closer to  $2^0$ .

#### 4.4.3. Effect of mass variation of auxetic meta-disk

The mass of the auxetic disks ( $M$ ) is calculated as the planar density ( $\rho$ ) multiplied by the surface area of the auxetic disk ( $A$ ) which is determined by the porosity ( $p$ ) of the auxetic disk unit cell ( $M = \rho(1-p)A$ ). The porosity is determined by the hinge thickness ratio (HR) varying from 0.1 to 0.8 and the slit thickness ratio (SR = 0.1), so its value is arranged from 0.01 to 0.08. Therefore, the masses of the auxetic disks are from 0.92 to 0.99 times the solid disk with the same dimension, which is negligible compared to the natural frequency variation.

#### 4.4.4. Bandgap formation

To achieve simultaneous modulation of two-mode bandgaps, we took advantage of the broad tunability of natural frequencies in both flexural and torsional modes. Through dispersion analysis of various design parameter combinations, we computed the band structures of the meta-disk integrated with the host structure. The numerical results confirmed the opening of bandgaps at the natural frequencies of the auxetic meta-disks, which could be independently tuned for each mode by adjusting the design variables, HR and AR. Figure 4-16 presents the band structures of an example auxetic meta-disk with HR = 0.3 and AR =  $2^0$ . The colored regions

represent the bandgaps, which opened at 213 Hz and closed at 302 Hz for the flexural wave, and opened at 121 Hz and closed at 227 Hz for the torsional wave. The corresponding mode shapes, shown in Figure 4-17, validate that the flexural or torsional resonance of the auxetic meta-disk resulted in the bandgap formation for the corresponding mode. In the flexural bandgap, a horizontal curve was observed at 262 Hz (a-iii), indicating out-of-phase modes with opposite phases on the front and back surfaces of the meta-disk. However, this configuration had an insignificant impact on wave propagation characteristics. Within the torsional bandgap, the curves exhibited out-of-phase (b-iii, 147 Hz) and radial mode (b-iv, 208 Hz) behaviors.

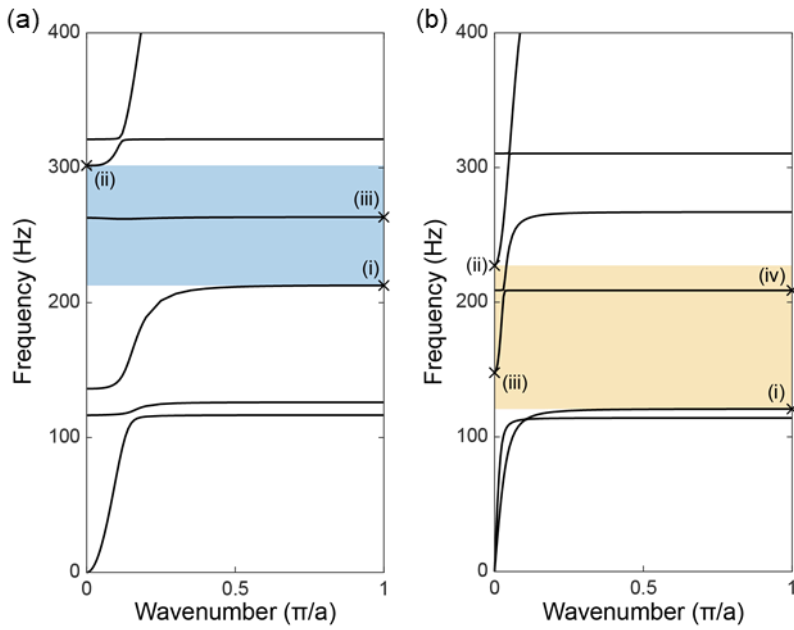


**Figure 4-16. Bandgap formation.** Band structures for (a) flexural and (b) torsional modes of an example meta-disk ( $AR=2^0$  and  $HR=0.3$ ). The blue and yellow areas correspond to the bandgaps.

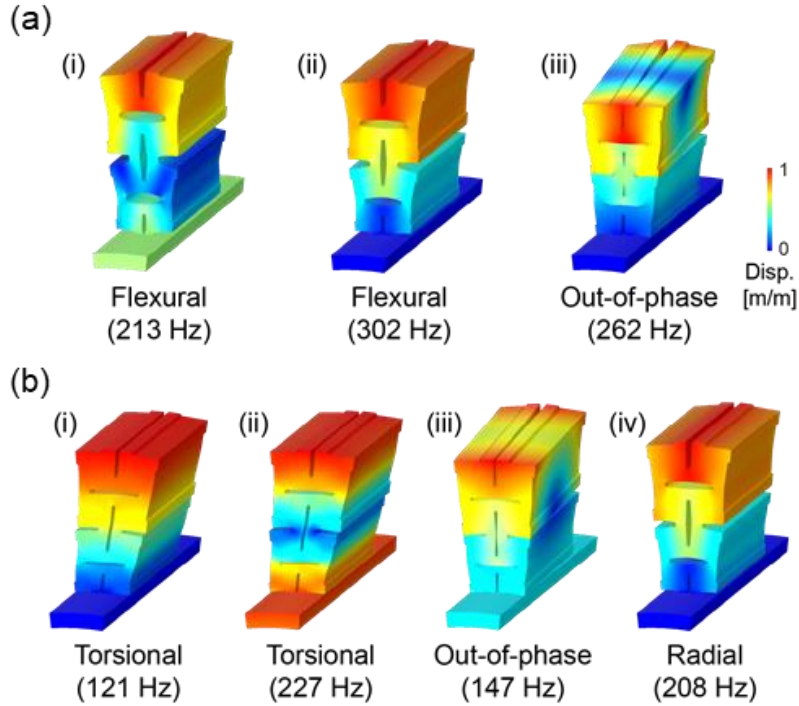


**Figure 4-17. Mode shapes for the points located in the bandgaps.** (a) Flexural, and (b) torsional modes. (iii) is the out-of-phase mode and (iv) is the radial mode which do not affect forming bandgaps.

#### 4.4.5. Designable range of bandgaps

Figure 4-18 presents a graphical representation of how the bandgap varies with different design parameters, HR and AR. The flexural and torsional bandgaps are represented by the blue and yellow bars, respectively. The bars' bottom and top edges indicate the frequencies at which the bandgap opens and closes for a specific auxetic meta-disk design. Specifically, the boxed bars in Figure 4-18 correspond to the flexural and torsional bandgaps of the model shown in Figure 4-16, with  $HR = 0.3$  and  $AR = 2^0$ . The shaded regions depict the feasible range of bandgap formation within the design variable area.

The opening frequencies of the bandgap align closely with the natural frequencies, which can be found in the tables in the Appendix. Consequently, the

bandgap frequencies follow a similar trend to the variations in natural frequencies. When HR is larger, both the flexural and torsional bandgap frequencies increase. Increasing AR results in an upward shift in the flexural bandgap, but the dependence on AR for the torsional mode is non-monotonic. The highest bandgap position occurs when the sub-rectangles have a square shape ( $AR = 2^0$ ) since it represents the stiffest shape.

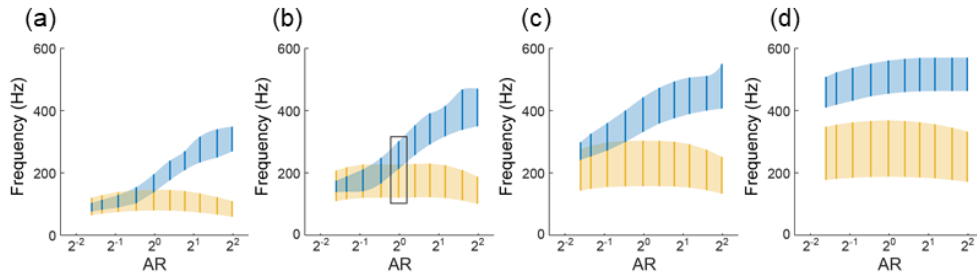


**Figure 4-18. Designable bandgap range.** The bandgaps in the two modes are denoted with blue and yellow color bar, respectively. The lower and upper frequencies of each bar represent the bandgap opening and closing frequency. The lateral axis represents the variation of AR and the values of HR are set constant in each subfigure as (a) 0.1, (b) 0.3, (c) 0.5, and (d) 0.7, respectively.

The distance between the meta-disks affects the bandgap closing frequency. It is known that the bandgap closing frequency is proportional to the mass ratio between the local resonator and the host structure. When the meta-disks are densely arranged, the mass ratio increases, leading to a wider bandgap. This was verified through dispersion analyses by varying the unit length of the pipe,  $a$ , by 1.5, 2, 4, and 8 times the thickness of the meta-disk ( $t = 127$  mm). Note that the default unit length,  $a$ , is equal to  $2t$ . In Figure 4-19, the bandgap closing frequencies decrease as the meta-disks are placed further apart. A similar effect can be observed when changing the axial thickness of a meta-disk while keeping the distances constant. For instance, a meta-disk with half the thickness produces the same bandgap as the model

with double the distance ( $4t$  in Figure 4-19), as the mass ratio of the host and the resonator remains unchanged.

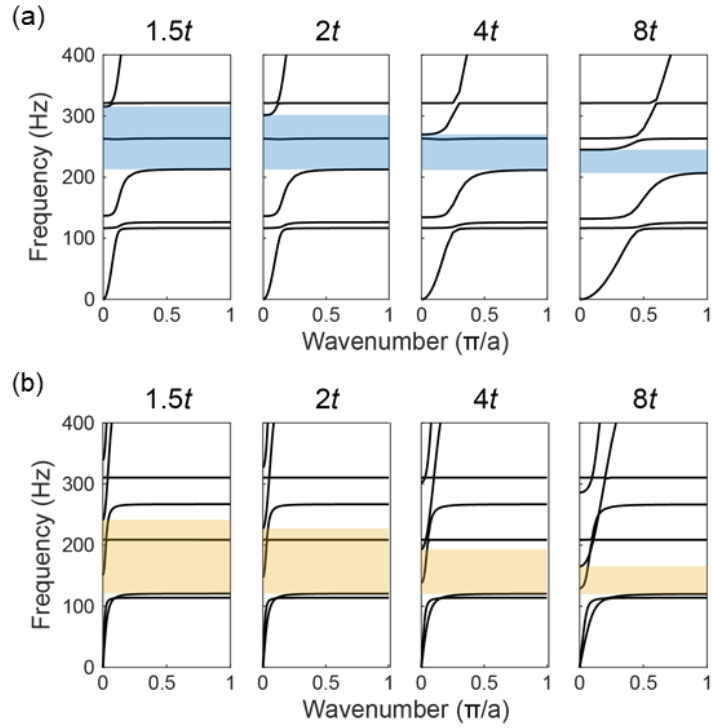


**Figure 4-19. Bandgap variation with the changes in the distance of auxetic meta-disks.** Band structures are plotted with bandgaps denoted with colored area for (a) flexural and (b) torsional mode. As the distance between the meta-disks increases, the mass ratio is reduced, resulting the bandgap closing frequency goes down.

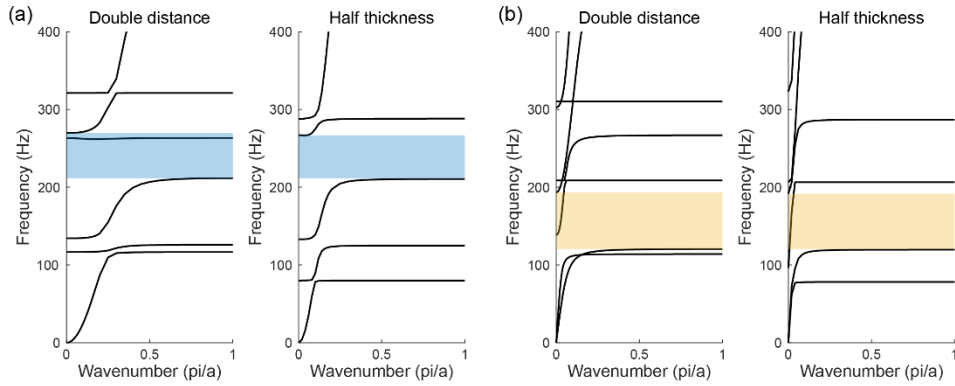


**Figure 4-20. Bandgap comparison between the double distance model and the half thickness model.** In the double distance model, the starting and ending frequency of the bandgaps are (212 Hz, 270 Hz) and (120 Hz, 193 Hz) for flexural and torsional modes, respectively, and in the half thickness model, the bandgap frequencies are (211 Hz, 267 Hz) and (120 Hz, 192 Hz) for flexural and torsional modes, respectively.

## 4.5. Numerical validation

We executed transmission analysis to confirm the wave propagation characteristics both inside and outside the bandgaps. The analysis revealed that wave propagation was effectively obstructed within the forbidden bands, while high transmission values were achieved outside the bandgap. Furthermore, we investigated the attenuation efficiency, which is influenced by the number of auxetic meta-disks used in the design.

### 4.5.1. Transmission analysis result

As demonstrated in Figure 4-21, the transmission value,  $T$ , showed a sharp decline at the bandgap opening frequency and maintained low values throughout the frequency band. The curves located within the bandgap, such as the out-of-phase or radial mode shown in Figure 4-17, exhibited little impact on the transmission values. Although a small peak appeared within the flexural bandgap in Figure 4-21a, the transmission value remained below 0 dB. The attenuation efficiency at the higher frequency within the band could be improved through a graded metamaterial design<sup>50-52</sup>, but this topic is beyond our scope. Nonetheless, the great part of the excited wave cannot propagate through the meta-structure, which proves that the auxetic meta-disks works effectively as local resonators.



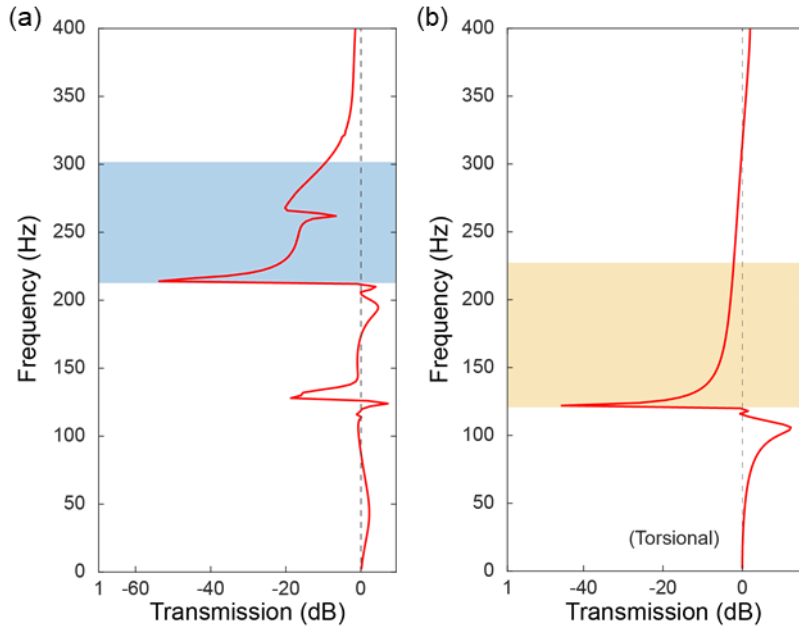


**Figure 4-21. Wave transmission in bandgaps.** (a) Flexural and (b) torsional wave. It was observed that the transmission values were sharply reduced in the bandgaps, especially near the bandgap opening frequency. The out-of-phase or radial mode existing in the bandgap do not significantly reduce the attenuation efficiency.

#### 4.5.2. Investigation of attenuation efficiency

One of the factors that affect how well attenuation occurs is the arrangement of auxetic meta-disks. The number of meta-disks in an array is connected to the attenuation effectiveness within a bandgap. Since the meta-disk acts as a local resonator, having a greater number of local resonators can enhance the attenuation effectiveness. This was confirmed through a study where the number of meta-disks was varied. The chosen design parameters for the meta-disk were  $HR = 0.3$  and  $AR = 2^0$ , and the number of meta-disks ranged from 4 to 12. It is important to note that while the location of the bandgap is a characteristic of the design of the unit cell, the number of meta-disks doesn't change the bandgap location but does affect the transmission of the meta-structure. Figure 4-22 shows the transmission results for

different numbers of meta-disks. In all cases, it was observed that as more resonators were added, a smaller portion of the wave was transmitted to the measurement point, resulting in lower transmission values. At the bandgap opening frequency, with only four meta-disks in the arrangement, the transmission values decreased to -30.4 dB for flexural waves and -30.2 dB for torsional waves. The minimum and average transmission values are presented in Table 4-2. An appropriate number of auxetic meta-disks can be chosen based on the specific requirements of an application.

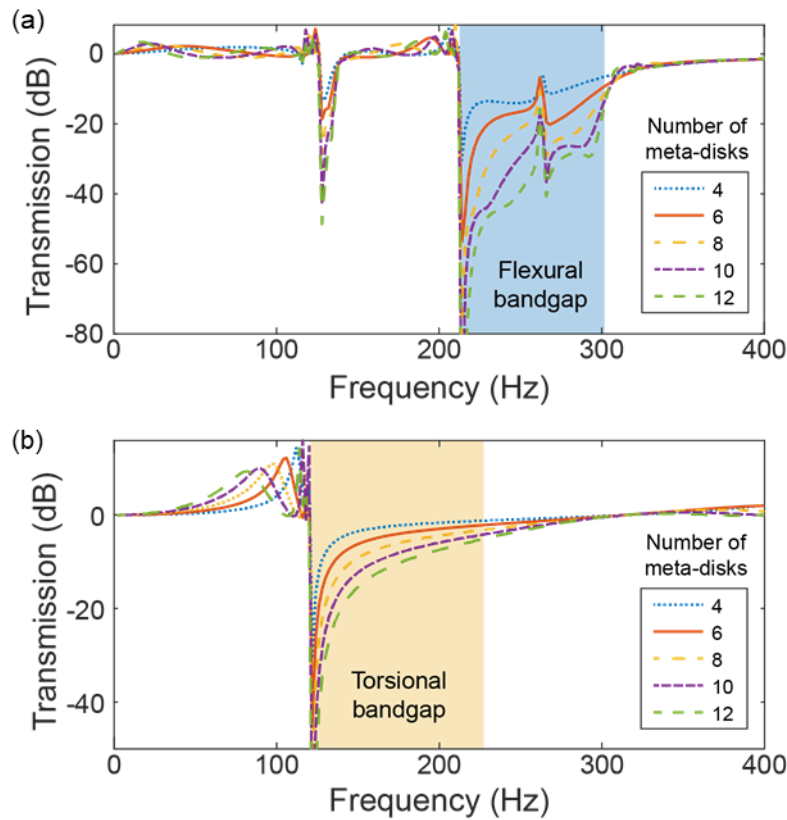


**Figure 4-22. Transmission variations with the different number of meta-disks.** Transmission value variations with the changes in the number of the meta-disks for (a) flexural and (b) torsional mode. Larger number of the meta-disks produces lower transmission values.

T (dB)	4	6	8	10	12
$T_{flex,min}$	-30.4	-53.7	-82.7	-126	-133
$T_{flex,avg}$	-12.2	-18.8	-26.7	-34.3	-40.5
$T_{tor,min}$	-30.2	-45.5	-61.0	-77.6	-92.2
$T_{tor,avg}$	-3.81	-6.44	-9.24	-12.2	-15.0

**Table 4-2. Minimum and average transmission values in the bandgap.** The design parameters are set as AR is equal to  $2^0$  and HR is 0.3.

## 4.6. Application: Elastic wave mode filter

The proposed design concept, which allows simultaneous control of two elastic wave modes, enables the selective transmission of a desired wave mode while blocking the undesired mode within a specific frequency range. To demonstrate the feasibility of this approach in mode filtering applications, several sample designs labeled as case 1-4 were considered. The unit cell design and the values of the design variables (AR, HR) are shown in Figure 4-23a. The flexural and torsional bandgaps for each case are plotted next to the unit cell. In these designs, the flexural and torsional waves were either blocked for both modes, blocked for one while allowing propagation of the other, or allowed to propagate for both at an arbitrary frequency (150 Hz) by positioning the excitation frequency inside or outside the bandgaps.

Figure 4-23b illustrates the steady-state configurations of the meta-structure, clearly demonstrating the filtering effect. The two figures for each case correspond to the excitation of flexural and torsional waves, respectively. The color bar represents the displacement magnitude. Within the bandgap, only a few local resonators exhibit significant vibration amplitude, while the right end of the host pipe has minimal oscillation. In contrast, when the excitation frequency is outside the bandgap, waves are effectively transmitted along the host structure.

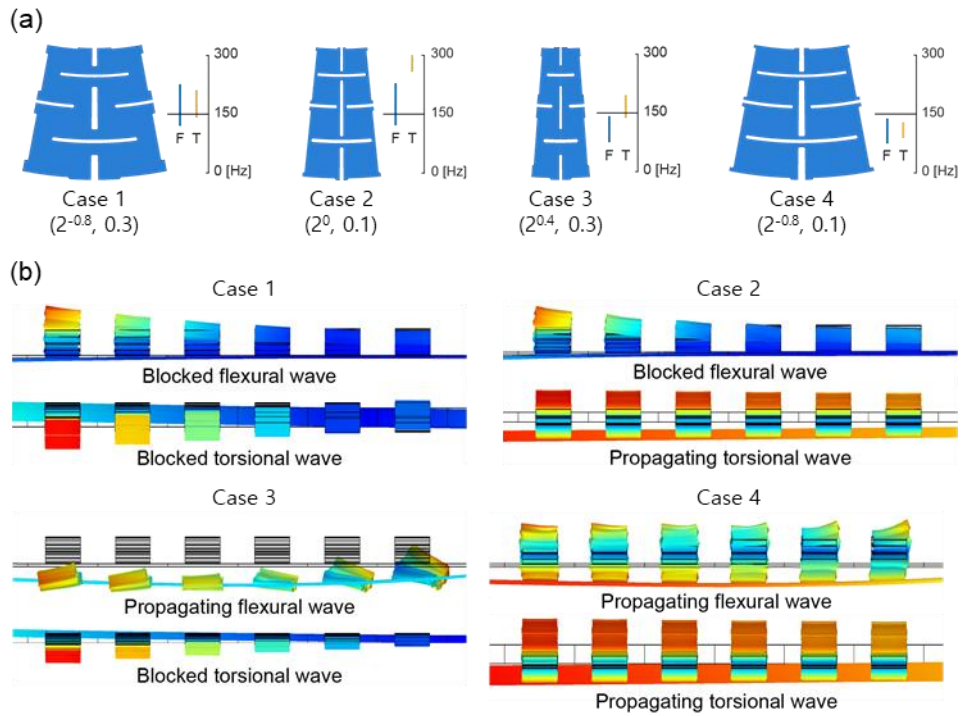


**Figure 4-23. Auxetic meta-disk application as an elastic wave mode filter. (a)** Four case designs of auxetic meta-disks with representation of the designed bandgaps. **(b)** The deformed configurations with the normalized displacement distribution are illustrated.

## 4.7. Conclusion

In this chapter, we introduced the design principles of locally resonant structures for the purpose of independently controlling the propagation of elastic waves in two different modes. By utilizing the load-dependent feature of auxetic pattern deformation, we were able to modulate the propagation of flexural and torsional waves in a pipe structure using locally resonant auxetic meta-disks. The numerical results demonstrated the feasibility of this approach within a broad frequency range and its potential applicability in elastic wave-mode filtering applications.

The main highlight of this chapter is the development of a metamaterial that allows for the simultaneous control of two distinct wave modes using a single auxetic meta-disk design. Additionally, the proposed meta-disk design does not require any modifications to the host structure for vibration attenuation, making it adaptable to various operating environments, including internal attachments. By appropriately arranging the auxetic unit cells, the design concept can be extended to other geometries, such as plates and shells, in addition to pipe structures.

The proposed idea is straightforward and has a wide-ranging impact, providing a foundation for the design of other wave modes, such as longitudinal and shear waves, in various structures.

## Chapter 5. Concluding remarks

In this work, we have presented a design principle for a rotating rigid auxetic pattern to adjust two different mechanical properties by exploiting the load-dependent deformation modes of auxetic pattern. We analyzed the deformation mechanism of each mode, specifically tension-dominant auxetic deformation mode and shear-dominant non-auxetic deformation mode. The key design variables of the auxetic unit cell are the hinge thickness ratio (HR) and the aspect ratio (AR), and their role in the two deformation modes was investigated.

Based on the design principle utilizing the load-dependent deformation modes of the auxetic pattern, we have successfully demonstrated auxetic meta-tube that can simultaneously control bending and torsional stiffness of tubular structure, as well as auxetic meta-disk which manipulates flexural and torsional wave propagation in pipe structures. Numerical and experimental results validate the versatility and effectiveness of our approach in the various applications.

The proposed design principles are straightforward and highly adaptable, making them suitable for various geometries such as plates, shells, and other various 3D structures due to their nondimensional nature. Further research on three-dimensional auxetic unit cells may facilitate applying to volumetric structures. Using additive patterns rather than perforation or different materials like hyperelastic materials can also be considered for novel characteristics of metamaterials. We hope that our approach provides a robust foundation for future work in the field of auxetic patterns, opening the door to new possibilities in the design and control of mechanical properties for a broad range of structures.

## Appendix.

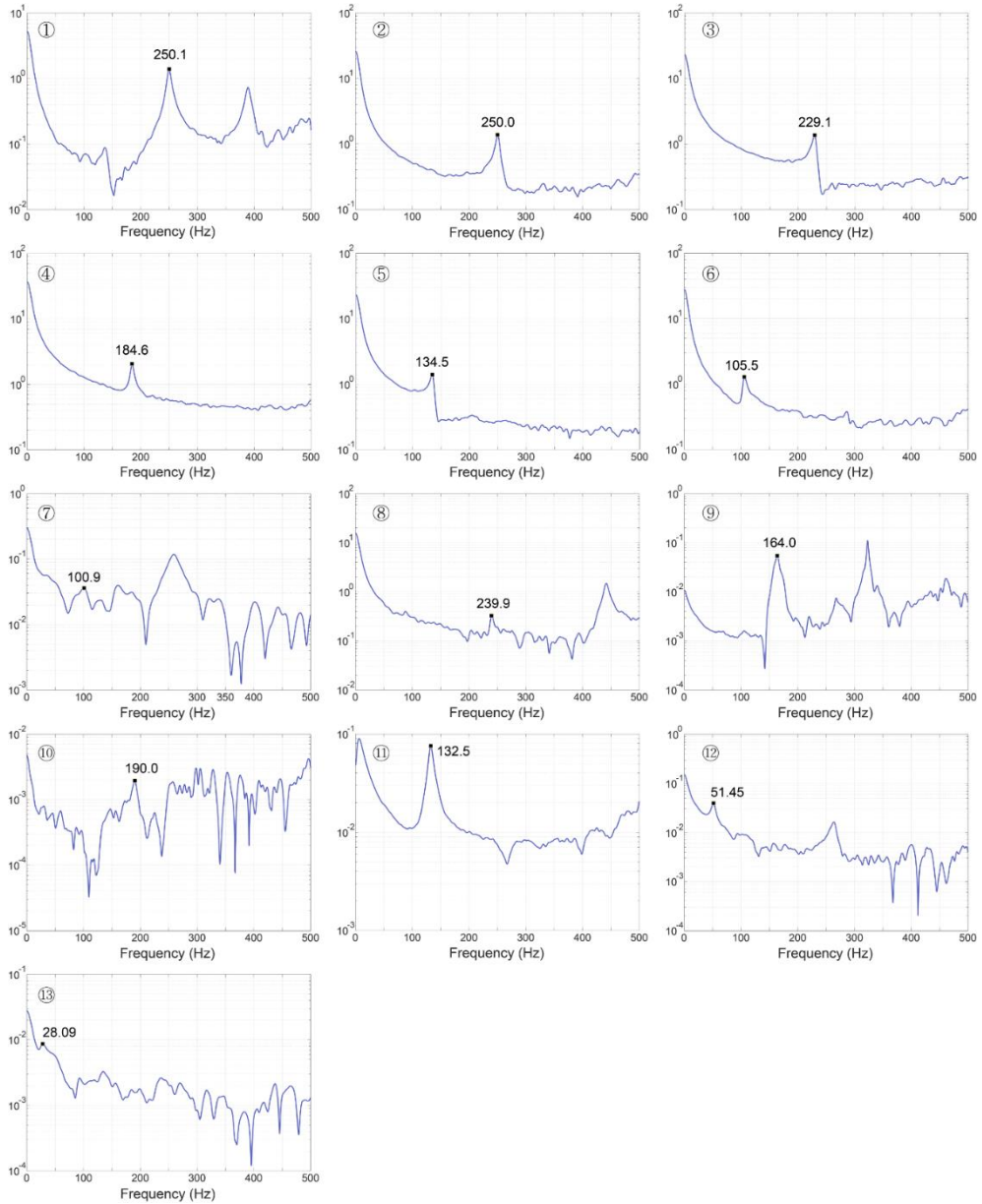


**Figure A-1. Frequency Response Functions (FRFs) of the auxetic tubes imposed an impact force.** The marked frequencies indicate the first mode bending natural frequencies of the tubes. The vertical axis refers magnitude in decibel unit.





**Figure A-2. Frequency Response Functions (FRFs) of the auxetic tubes imposed a torsional impact force. The marked frequencies indicate the first mode torsional natural frequencies of the tubes.**

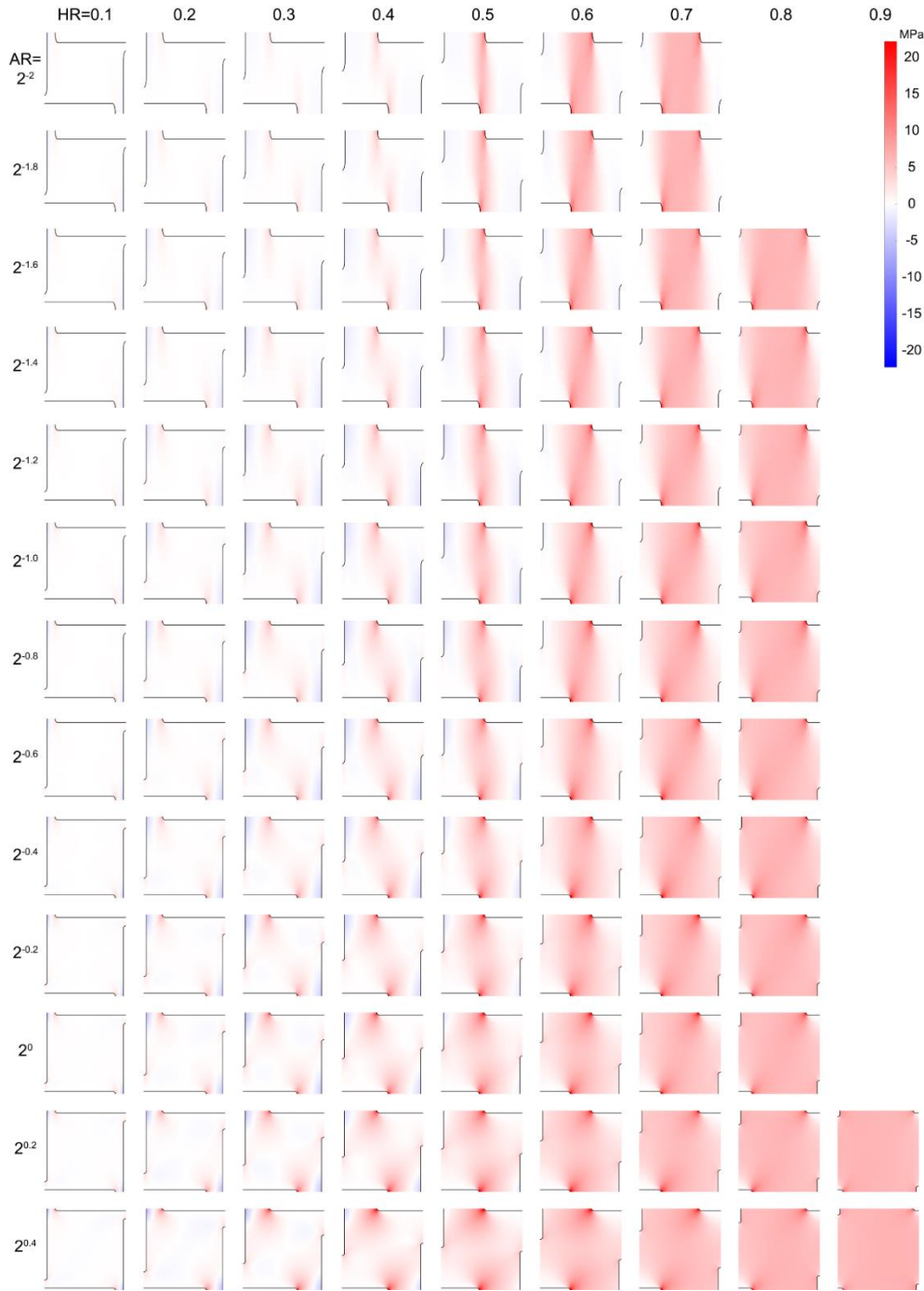


**Figure A-3. Normal stress distribution in auxetic tube unit cell under bending load.** The sizes of the unit cells are normalized to be the same to the unit cell with  $AR = 2^0$ .

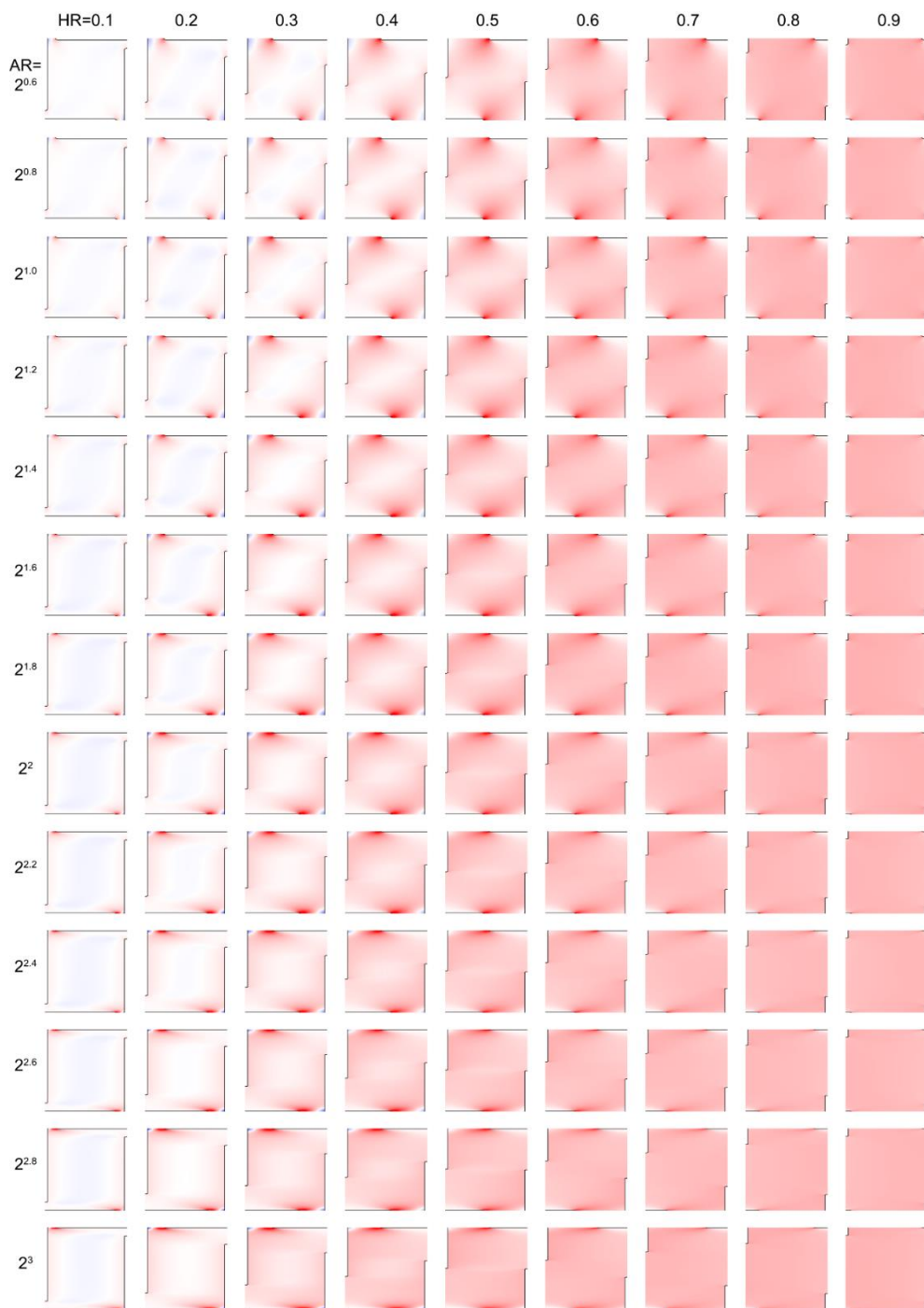


**Figure A-4. Normal stress distribution in auxetic tube unit cell under bending load (continued).**

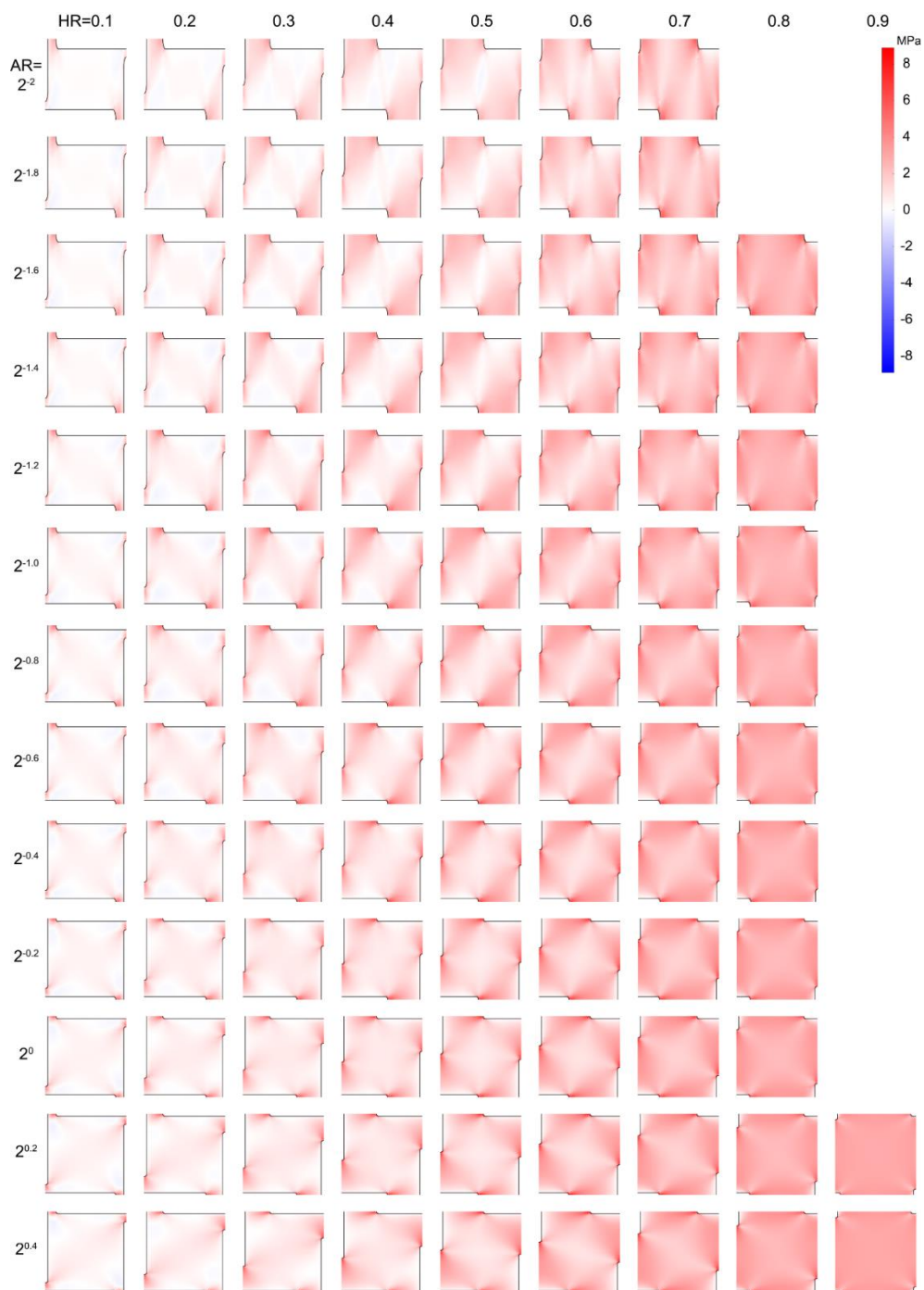


**Figure A-5. Shear stress distribution in auxetic tube unit cell under torsional load.**

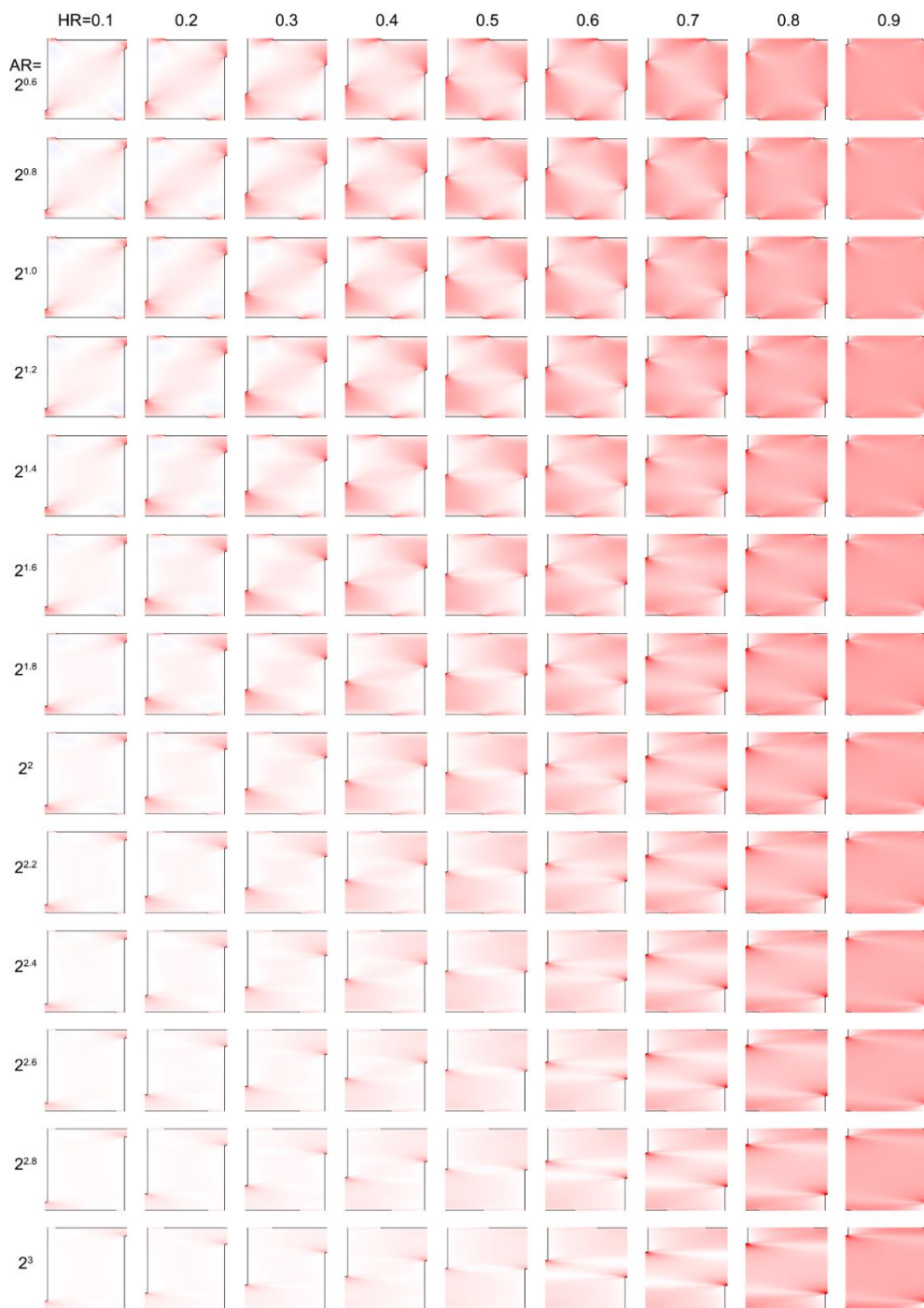


**Figure A-6 Shear stress distribution in auxetic tube unit cell under torsional load (continued).**

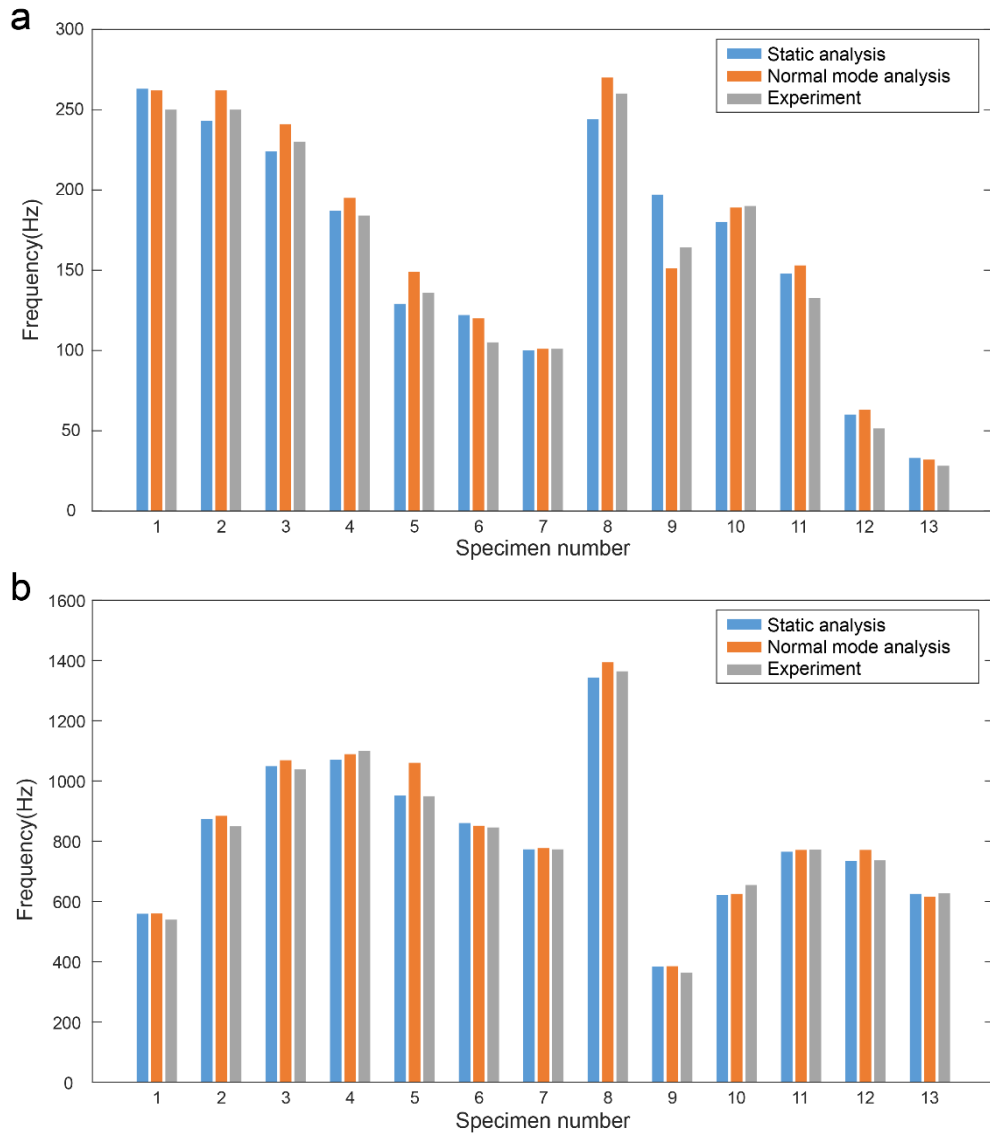


**Figure A-7. Frequency comparison between FE static, normal mode analysis and experiment. a) 1<sup>st</sup> bending mode frequencies, and b) 1<sup>st</sup> torsional mode frequencies.**



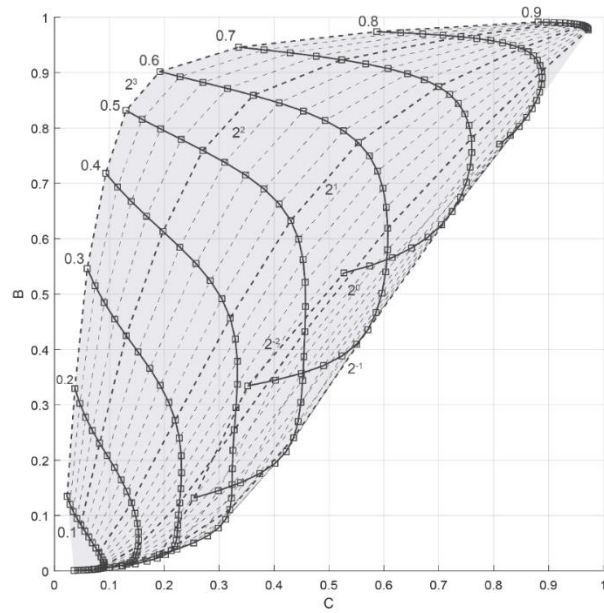


**Figure A-8. Feasible stiffness region of rectangular unit auxetic tube.** The solid and dashed lines indicate constant AR, and HR respectively.

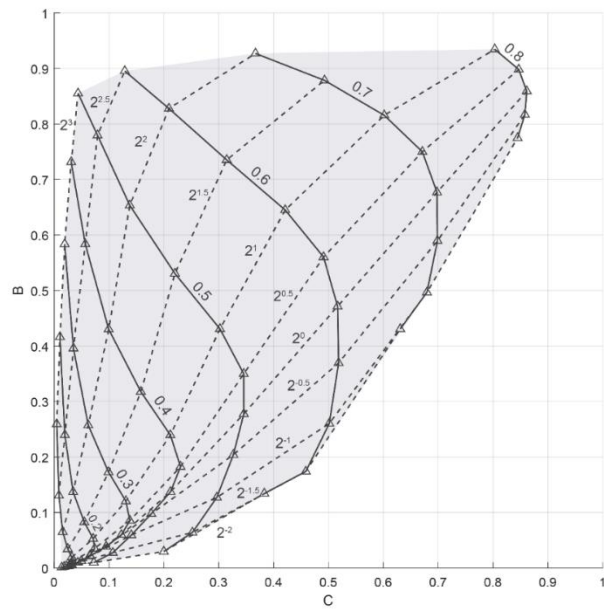


**Figure A-9. Feasible stiffness region of triangular unit auxetic tube.**

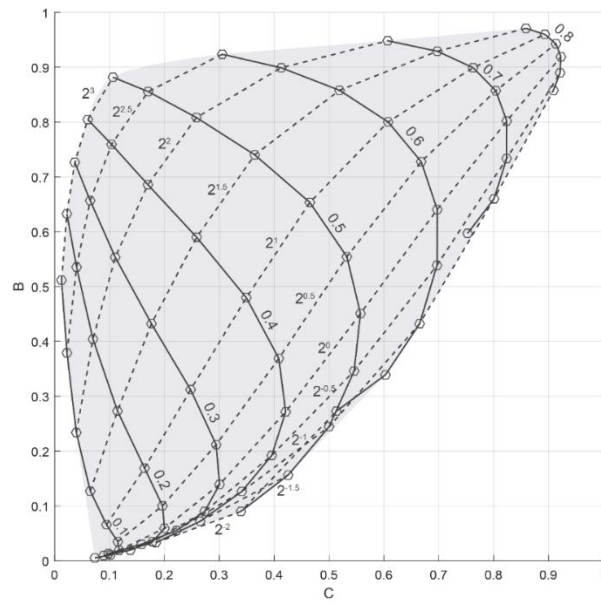


**Figure A-10. Feasible stiffness region of hexa-triangular unit auxetic tube.**



B*	0.1	0.2	0.3	0.4	0.5	0.6	0.7	0.8	0.9
2 <sup>-2</sup>	0.001	0.003	0.009	0.029	0.132	0.334	0.538	-	-
2 <sup>-1.8</sup>	0.001	0.005	0.013	0.039	0.145	0.345	0.551	-	-
2 <sup>-1.6</sup>	0.001	0.006	0.017	0.050	0.159	0.357	0.566	0.771	-
2 <sup>-1.4</sup>	0.002	0.008	0.023	0.063	0.176	0.371	0.583	0.787	-
2 <sup>-1.2</sup>	0.002	0.010	0.029	0.077	0.194	0.388	0.603	0.803	-
2 <sup>-1</sup>	0.002	0.012	0.037	0.093	0.215	0.410	0.625	0.819	-
2 <sup>-0.8</sup>	0.003	0.015	0.045	0.111	0.240	0.436	0.649	0.835	-
2 <sup>-0.6</sup>	0.003	0.018	0.055	0.131	0.270	0.466	0.675	0.850	-
2 <sup>-0.4</sup>	0.004	0.023	0.068	0.156	0.304	0.502	0.702	0.865	-
2 <sup>-0.2</sup>	0.005	0.028	0.083	0.185	0.344	0.540	0.729	0.878	-
2 <sup>0</sup>	0.007	0.036	0.101	0.218	0.387	0.580	0.756	0.891	-
2 <sup>0.2</sup>	0.009	0.045	0.123	0.255	0.432	0.619	0.781	0.903	0.977
2 <sup>0.4</sup>	0.011	0.056	0.148	0.295	0.477	0.657	0.805	0.913	0.979
2 <sup>0.6</sup>	0.015	0.070	0.177	0.337	0.521	0.691	0.826	0.922	0.981
2 <sup>0.8</sup>	0.020	0.086	0.208	0.379	0.562	0.722	0.844	0.930	0.983
2 <sup>1</sup>	0.026	0.104	0.240	0.419	0.599	0.750	0.861	0.938	0.984
2 <sup>1.2</sup>	0.033	0.123	0.272	0.457	0.633	0.774	0.875	0.944	0.985
2 <sup>1.4</sup>	0.041	0.144	0.304	0.492	0.663	0.795	0.887	0.949	0.986
2 <sup>1.6</sup>	0.051	0.165	0.335	0.524	0.690	0.814	0.898	0.954	0.987
2 <sup>1.8</sup>	0.061	0.187	0.366	0.555	0.715	0.830	0.907	0.958	0.988
2 <sup>2</sup>	0.072	0.208	0.396	0.585	0.738	0.845	0.916	0.962	0.989
2 <sup>2.2</sup>	0.083	0.231	0.425	0.613	0.759	0.859	0.923	0.965	0.990
2 <sup>2.4</sup>	0.095	0.254	0.455	0.641	0.780	0.871	0.930	0.967	0.990
2 <sup>2.6</sup>	0.107	0.278	0.485	0.667	0.798	0.882	0.936	0.970	0.991
2 <sup>2.8</sup>	0.120	0.303	0.515	0.693	0.816	0.893	0.941	0.972	0.991
2 <sup>3</sup>	0.135	0.329	0.546	0.718	0.832	0.902	0.946	0.974	0.991

**Table A-1. Normalized bending stiffness of rectangular pattern.**

C*	0.1	0.2	0.3	0.4	0.5	0.6	0.7	0.8	0.9
2 <sup>-2</sup>	0.036	0.072	0.124	0.191	0.254	0.352	0.527	-	-
2 <sup>-1.8</sup>	0.042	0.086	0.147	0.223	0.298	0.403	0.574	-	-
2 <sup>-1.6</sup>	0.049	0.100	0.169	0.253	0.339	0.450	0.615	0.811	-
2 <sup>-1.4</sup>	0.056	0.112	0.187	0.279	0.374	0.490	0.650	0.830	-
2 <sup>-1.2</sup>	0.063	0.123	0.202	0.298	0.402	0.524	0.680	0.847	-
2 <sup>-1</sup>	0.069	0.131	0.213	0.312	0.422	0.550	0.705	0.860	-
2 <sup>-0.8</sup>	0.074	0.138	0.219	0.319	0.436	0.571	0.724	0.870	-
2 <sup>-0.6</sup>	0.079	0.143	0.222	0.323	0.444	0.586	0.739	0.878	-
2 <sup>-0.4</sup>	0.083	0.146	0.224	0.323	0.449	0.596	0.750	0.884	-
2 <sup>-0.2</sup>	0.086	0.149	0.225	0.324	0.452	0.603	0.757	0.887	-
2 <sup>0</sup>	0.088	0.151	0.226	0.325	0.454	0.607	0.760	0.888	-
2 <sup>0.2</sup>	0.090	0.152	0.228	0.328	0.456	0.607	0.759	0.887	0.972
2 <sup>0.4</sup>	0.091	0.153	0.230	0.331	0.457	0.604	0.755	0.885	0.971
2 <sup>0.6</sup>	0.090	0.153	0.232	0.333	0.457	0.598	0.747	0.880	0.970
2 <sup>0.8</sup>	0.088	0.151	0.231	0.333	0.453	0.588	0.736	0.872	0.968
2 <sup>1</sup>	0.085	0.147	0.227	0.329	0.445	0.574	0.720	0.863	0.965
2 <sup>1.2</sup>	0.081	0.141	0.220	0.320	0.430	0.553	0.700	0.850	0.961
2 <sup>1.4</sup>	0.075	0.132	0.208	0.305	0.409	0.527	0.674	0.835	0.957
2 <sup>1.6</sup>	0.069	0.122	0.193	0.284	0.382	0.493	0.643	0.816	0.952
2 <sup>1.8</sup>	0.063	0.109	0.173	0.258	0.348	0.453	0.608	0.795	0.946
2 <sup>2</sup>	0.055	0.096	0.152	0.228	0.310	0.409	0.567	0.769	0.939
2 <sup>2.2</sup>	0.048	0.082	0.131	0.198	0.270	0.362	0.523	0.740	0.931
2 <sup>2.4</sup>	0.041	0.069	0.110	0.168	0.231	0.315	0.477	0.707	0.921
2 <sup>2.6</sup>	0.034	0.057	0.091	0.140	0.193	0.270	0.429	0.671	0.909
2 <sup>2.8</sup>	0.028	0.046	0.074	0.115	0.160	0.229	0.382	0.630	0.896
2 <sup>3</sup>	0.023	0.037	0.060	0.093	0.130	0.192	0.335	0.587	0.881

**Table A-2. Normalized torsional stiffness of rectangular pattern.**

B*	0.1	0.2	0.3	0.4	0.5	0.6	0.7	0.8
2 <sup>-2</sup>	-	-	0.003	0.010	0.030	0.134	-	-
2 <sup>-1.5</sup>	-	0.002	0.010	0.028	0.064	0.174	0.431	-
2 <sup>-1</sup>	0.001	0.006	0.021	0.059	0.127	0.260	0.497	0.775
2 <sup>-0.5</sup>	0.003	0.013	0.039	0.098	0.204	0.369	0.590	0.817
2 <sup>0</sup>	0.007	0.023	0.060	0.137	0.278	0.471	0.677	0.859
2 <sup>0.5</sup>	0.011	0.035	0.085	0.182	0.350	0.560	0.750	0.898
2 <sup>1</sup>	0.019	0.053	0.120	0.240	0.431	0.645	0.816	0.935
2 <sup>1.5</sup>	0.034	0.083	0.173	0.318	0.531	0.735	0.878	-
2 <sup>2</sup>	0.065	0.137	0.257	0.430	0.653	0.828	0.927	-
2 <sup>2.5</sup>	0.131	0.240	0.396	0.584	0.780	0.895	-	-
2 <sup>3</sup>	0.259	0.416	0.584	0.731	0.855	-	-	-

**Table A-3. Normalized bending stiffness of triangular pattern.**

C*	0.1	0.2	0.3	0.4	0.5	0.6	0.7	0.8
2 <sup>-2</sup>	-	-	0.026	0.072	0.200	0.383	-	-
2 <sup>-1.5</sup>	-	0.018	0.043	0.107	0.252	0.459	0.631	-
2 <sup>-1</sup>	0.014	0.032	0.065	0.141	0.296	0.501	0.680	0.845
2 <sup>-0.5</sup>	0.022	0.049	0.095	0.177	0.327	0.518	0.699	0.858
2 <sup>0</sup>	0.029	0.065	0.122	0.212	0.346	0.517	0.698	0.861
2 <sup>0.5</sup>	0.033	0.074	0.138	0.230	0.346	0.491	0.671	0.847
2 <sup>1</sup>	0.032	0.071	0.131	0.212	0.302	0.421	0.602	0.803
2 <sup>1.5</sup>	0.025	0.055	0.099	0.158	0.220	0.314	0.493	-
2 <sup>2</sup>	0.016	0.035	0.062	0.099	0.138	0.209	0.367	-
2 <sup>2.5</sup>	0.009	0.019	0.035	0.057	0.079	0.129	-	-
2 <sup>3</sup>	0.005	0.010	0.019	0.031	0.043	-	-	-

**Table A-4. Normalized torsional stiffness of triangular pattern.**

B*	0.1	0.2	0.3	0.4	0.5	0.6	0.7	0.8
$2^{-2}$	-	-	0.013	0.033	0.090	0.273	-	-
$2^{-1.5}$	-	0.010	0.030	0.072	0.156	0.339	0.597	-
$2^{-1}$	0.005	0.019	0.055	0.126	0.245	0.432	0.660	0.858
$2^{-0.5}$	0.010	0.035	0.090	0.192	0.346	0.539	0.733	0.890
$2^0$	0.019	0.059	0.139	0.272	0.451	0.640	0.802	0.919
$2^{0.5}$	0.035	0.100	0.212	0.369	0.554	0.728	0.857	0.943
$2^1$	0.066	0.169	0.312	0.480	0.653	0.800	0.899	0.960
$2^{1.5}$	0.127	0.273	0.432	0.590	0.740	0.858	0.929	0.971
$2^2$	0.234	0.404	0.553	0.686	0.808	0.899	0.948	-
$2^{2.5}$	0.379	0.535	0.657	0.759	0.856	0.924	-	-
$2^3$	0.512	0.633	0.726	0.805	0.882	-	-	-

**Table A-5. Normalized bending stiffness of hexa-triangular pattern.**

C*	0.1	0.2	0.3	0.4	0.5	0.6	0.7	0.8
$2^{-2}$	-	-	0.098	0.184	0.339	0.513	-	-
$2^{-1.5}$	-	0.090	0.158	0.265	0.425	0.603	0.753	-
$2^{-1}$	0.073	0.138	0.222	0.341	0.500	0.665	0.801	0.909
$2^{-0.5}$	0.101	0.178	0.273	0.396	0.546	0.697	0.824	0.921
$2^0$	0.117	0.200	0.300	0.421	0.557	0.697	0.824	0.923
$2^{0.5}$	0.115	0.196	0.294	0.408	0.532	0.668	0.804	0.914
$2^1$	0.094	0.164	0.248	0.349	0.465	0.608	0.763	0.893
$2^{1.5}$	0.065	0.114	0.176	0.259	0.365	0.519	0.697	0.859
$2^2$	0.039	0.070	0.110	0.170	0.258	0.413	0.607	-
$2^{2.5}$	0.022	0.040	0.065	0.104	0.170	0.305	-	-
$2^3$	0.012	0.022	0.037	0.060	0.106	-	-	-

**Table A-6. Normalized torsional stiffness of hexa-triangular pattern.**

HR=0.1	Flexural			Torsional		
AR	f	opening	closing	f	opening	closing
$2^{-1.6}$	76.1	76.1	104.0	64.9	64.9	120.2
$2^{-1.2}$	81.4	81.4	113.5	69.5	69.5	128.5
$2^{-0.8}$	88.8	88.8	128.9	75.0	75.0	138.5
$2^{-0.4}$	102.4	102.4	154.1	78.1	78.1	143.8
$2^0$	137.5	137.5	195.8	79.4	79.4	146.1
$2^{0.4}$	178.8	177.1	239.4	78.8	78.8	145.0
$2^{0.8}$	211.4	208.9	269.9	77.0	77.0	141.8
$2^{1.2}$	237.5	233.4	326.8	72.9	72.9	134.1
$2^{1.6}$	258.3	249.7	340.0	66.4	66.4	122.3
$2^2$	277.5	269.0	348.5	59.3	59.3	109.4

**Table A-7. Natural frequency and bandgap frequencies of the auxetic disk. HR is constant as 0.1.**

HR=0.3	Flexural			Torsional		
AR	f	opening	closing	f	opening	closing
$2^{-1.6}$	138.4	138.3	175.2	109.8	109.8	207.6
$2^{-1.2}$	139.7	139.7	188.4	115.3	115.3	218.1
$2^{-0.8}$	141.1	141.1	211.1	120.1	120.1	226.6
$2^{-0.4}$	166.2	166.2	248.1	120.7	120.7	227.4
$2^0$	213.8	212.7	301.7	120.7	120.7	227.2
$2^{0.4}$	260.9	257.4	353.1	121.6	121.6	228.8
$2^{0.8}$	296.3	291.5	391.1	122.1	122.1	229.7
$2^{1.2}$	324.8	317.5	415.1	119.7	119.7	224.7
$2^{1.6}$	349.3	338.3	468.0	111.8	111.8	209.2
$2^2$	361.6	349.8	470.7	100.8	100.8	187.9

**Table A-8. Natural frequency and bandgap frequencies of the auxetic disk. HR is constant as 0.3.**

HR=0.5	Flexural			Torsional		
AR	f	opening	closing	f	opening	closing
$2^{-1.6}$	242.0	242.0	298.4	143.5	143.5	275.8
$2^{-1.2}$	253.9	253.0	325.8	149.2	149.2	287.5
$2^{-0.8}$	273.1	271.7	359.9	154.8	154.8	298.4
$2^{-0.4}$	301.7	299.3	400.3	156.9	156.9	302.2
$2^0$	334.8	331.4	442.3	157.7	157.7	303.4
$2^{0.4}$	363.1	358.9	473.2	157.6	157.6	302.7
$2^{0.8}$	383.4	375.4	493.3	156.7	156.7	300.2
$2^{1.2}$	399.1	389.4	506.0	153.1	153.1	292.1
$2^{1.6}$	411.8	400.4	511.4	144.6	144.6	274.4
$2^2$	419.4	406.5	549.9	133.2	133.2	251.2

**Table A-9. Natural frequency and bandgap frequencies of the auxetic disk. HR is constant as 0.5.**

HR=0.7	flexural			torsional		
AR	f	opening	closing	f	opening	closing
$2^{-1.6}$	414.9	409.9	508.2	177.7	177.7	348.1
$2^{-1.2}$	424.3	419.1	522.9	180.7	180.7	354.4
$2^{-0.8}$	437.7	431.9	537.6	184.4	184.4	362.2
$2^{-0.4}$	450.8	446.2	550.8	186.8	186.8	366.8
$2^0$	461.2	454.5	560.7	187.8	187.8	368.6
$2^{0.4}$	467.7	459.6	566.2	187.0	187.0	366.7
$2^{0.8}$	471.4	462.2	569.3	185.4	185.4	362.9
$2^{1.2}$	473.0	463.0	570.1	182.4	182.4	356.0
$2^{1.6}$	474.1	463.1	570.1	177.4	177.4	345.2
$2^2$	474.2	463.1	570.4	171.6	171.6	332.7

**Table A-10. Natural frequency and bandgap frequencies of the auxetic disk.**

HR is constant as 0.7.

# Bibliography

- 1 Evans, K. & Caddock, B. Microporous materials with negative Poisson's ratios. II. Mechanisms and interpretation. *Journal of Physics D: Applied Physics* **22**, 1883 (1989).
- 2 Lakes, R. Foam Structures with a Negative Poisson's Ratio. *Science*. **235**, 1038-1040, doi:10.1126/science.235.4792.1038 (1987).
- 3 Evans, K. E., Nkansah, M., Hutchinson, I. & Rogers, S. Molecular network design. *Nature* **353**, 124-124 (1991).
- 4 Chan, N. & Evans, K. Fabrication methods for auxetic foams. *Journal of Materials Science* **32**, 5945-5953 (1997).
- 5 Yeganeh-Haeri, A., Weidner, D. J. & Parise, J. B. Elasticity of  $\alpha$ -Cristobalite: A Silicon Dioxide with a Negative Poisson's Ratio. *Science*. **257**, 650-652, doi:10.1126/science.257.5070.650 (1992).
- 6 Grima, J. N., Jackson, R., Alderson, A. & Evans, K. E. Do Zeolites Have Negative Poisson's Ratios? *Advanced Materials* **12**, 1912-1918, doi:[https://doi.org/10.1002/1521-4095\(200012\)12:24<1912::AID-ADMA1912>3.0.CO;2-7](https://doi.org/10.1002/1521-4095(200012)12:24<1912::AID-ADMA1912>3.0.CO;2-7) (2000).
- 7 Alderson, K. & Evans, K. The fabrication of microporous polyethylene having a negative Poisson's ratio. *Polymer* **33**, 4435-4438 (1992).
- 8 Alderson, K. *et al.* How to make auxetic fibre reinforced composites. *physica status solidi (b)* **242**, 509-518 (2005).
- 9 Grima, J. N., Gatt, R., Ravirala, N., Alderson, A. & Evans, K. E. Negative Poisson's ratios in cellular foam materials. *Materials Science and Engineering: A* **423**, 214-218 (2006).
- 10 Alderson, A., Davies, P., Evans, K., Alderson, K. & Grima, J. Modelling of the mechanical and mass transport properties of auxetic molecular sieves: an idealised inorganic (zeolitic) host-guest system. *Molecular Simulation* **31**, 889-896 (2005).
- 11 Masters, I. & Evans, K. Models for the elastic deformation of honeycombs. *Composite structures* **35**, 403-422 (1996).
- 12 Theocaris, P., Stavroulakis, G. & Panagiotopoulos, P. Negative Poisson's ratios in composites with star-shaped inclusions: a numerical homogenization approach. *Archive of applied mechanics* **67**, 274-286 (1997).
- 13 Smith, C. W., Grima, J. & Evans, K. A novel mechanism for generating auxetic behaviour in reticulated foams: missing rib foam model. *Acta materialia* **48**, 4349-4356 (2000).
- 14 Grima, J. N. & Evans, K. E. Auxetic behavior from rotating squares. *Journal of Materials Science Letters* **19**, 1563-1565 (2000).
- 15 Grima, J. N., Gatt, R., Alderson, A. & Evans, K. E. On the auxetic properties of 'rotating rectangles' with different connectivity. *Journal of the Physical Society of Japan* **74**, 2866-2867 (2005).
- 16 Grima, J. N. & Evans, K. E. Auxetic behavior from rotating triangles. *Journal of materials science* **41**, 3193-3196 (2006).
- 17 Grima, J. N., Zammit, V., Gatt, R., Alderson, A. & Evans, K. Auxetic behaviour from rotating semi-rigid units. *physica status solidi (b)* **244**, 866-882 (2007).
- 18 Prall, D. & Lakes, R. Properties of a chiral honeycomb with a Poisson's ratio of—1. *International Journal of Mechanical Sciences* **39**, 305-314 (1997).
- 19 Grima, J. N., Gatt, R. & Farrugia, P. S. On the properties of auxetic meta-tetrachiral structures. *physica status solidi (b)* **245**, 511-520 (2008).
- 20 Spadoni, A. & Ruzzene, M. Elasto-static micropolar behavior of a chiral auxetic lattice. *Journal of the Mechanics and Physics of Solids* **60**, 156-171 (2012).

- 21 Scarpa, F., Smith, C., Ruzzene, M. & Wade, M. Mechanical properties of auxetic tubular truss-like structures. *physica status solidi (b)* **245**, 584-590 (2008).
- 22 Fu, M.-H., Chen, Y. & Hu, L.-L. A novel auxetic honeycomb with enhanced in-plane stiffness and buckling strength. *Composite Structures* **160**, 574-585, doi:<https://doi.org/10.1016/j.compstruct.2016.10.090> (2017).
- 23 Ren, X., Shen, J., Ghaedizadeh, A., Tian, H. & Xie, Y. M. A simple auxetic tubular structure with tuneable mechanical properties. *Smart Materials and Structures* **25**, 065012 (2016).
- 24 Rossiter, J., Takashima, K., Scarpa, F., Walters, P. & Mukai, T. Shape memory polymer hexachiral auxetic structures with tunable stiffness. *Smart Materials and Structures* **23**, 045007 (2014).
- 25 Zhu, H., Fan, T. & Zhang, D. Composite materials with enhanced dimensionless Young's modulus and desired Poisson's ratio. *Scientific reports* **5**, 14103 (2015).
- 26 Rayneau-Kirkhope, D. Stiff auxetics: Hierarchy as a route to stiff, strong lattice based auxetic meta-materials. *Scientific reports* **8**, 12437 (2018).
- 27 Javid, F., Wang, P., Shanian, A. & Bertoldi, K. Architected Materials with Ultra-Low Porosity for Vibration Control. *Advanced Materials* **28**, 5943-5948 (2016).
- 28 Imbalzano, G., Tran, P., Ngo, T. D. & Lee, P. V. A numerical study of auxetic composite panels under blast loadings. *Composite Structures* **135**, 339-352 (2016).
- 29 Scarpa, F. & Tomlinson, G. Theoretical characteristics of the vibration of sandwich plates with in-plane negative Poisson's ratio values. *Journal of Sound and Vibration* **230**, 45-67 (2000).
- 30 Liu, X., Hu, G., Sun, C. & Huang, G. Wave propagation characterization and design of two-dimensional elastic chiral metacomposite. *Journal of Sound and Vibration* **330**, 2536-2553 (2011).
- 31 Deng, B., Raney, J., Tournat, V. & Bertoldi, K. Elastic Vector Solitons in Soft Architected Materials. *Physical review letters* **118**, 204102 (2017).
- 32 Tee, K., Spadoni, A., Scarpa, F. & Ruzzene, M. Wave propagation in auxetic tetrachiral honeycombs. *Journal of Vibration and Acoustics* **132**, 031007 (2010).
- 33 Hou, F., Xiao, S. & Wang, H. Mechanical properties characterization and zero Poisson's ratio design for perforated auxetic metamaterial by computational homogenized method. *Mechanics of Advanced Materials and Structures*, 1-12 (2021).
- 34 Wang, H., Zhang, Y., Lin, W. & Qin, Q.-H. A novel two-dimensional mechanical metamaterial with negative Poisson's ratio. *Computational Materials Science* **171**, 109232 (2020).
- 35 Lee, D.-Y. *et al.* Anisotropic patterning to reduce instability of concentric-tube robots. *IEEE Transactions on Robotics* **31**, 1311-1323 (2015).
- 36 Liu, Z. *et al.* Locally resonant sonic materials. *science* **289**, 1734-1736 (2000).
- 37 Qiao, H., Li, Q. & Li, G. Vibratory characteristics of flexural non-uniform Euler-Bernoulli beams carrying an arbitrary number of spring-mass systems. *International Journal of Mechanical Sciences* **44**, 725-743 (2002).
- 38 Yu, D., Liu, Y., Zhao, H., Wang, G. & Qiu, J. Flexural vibration band gaps in Euler-Bernoulli beams with locally resonant structures with two degrees of freedom. *Physical Review B* **73**, 064301 (2006).
- 39 Yu, D., Wen, J., Zhao, H., Liu, Y. & Wen, X. Vibration reduction by using the idea of phononic crystals in a pipe-conveying fluid. *Journal of Sound and vibration* **318**, 193-205 (2008).
- 40 Yu, D., Liu, Y., Wang, G., Zhao, H. & Qiu, J. Flexural vibration band gaps in Timoshenko beams with locally resonant structures. *Journal of applied physics* **100**, 124901 (2006).
- 41 Wang, Z., Zhang, P. & Zhang, Y. Locally resonant band gaps in flexural vibrations of a Timoshenko beam with periodically attached multioscillators. *Mathematical*



- Problems in Engineering* **2013** (2013).
- 42 Tang, D., Pang, F., Zhang, Z. & Li, L. Flexural wave propagation and attenuation through Timoshenko beam coupled with periodic resonators by the method of reverberation-ray matrix. *European Journal of Mechanics-A/Solids* **86**, 104153 (2021).
- 43 Yu, D., Liu, Y., Wang, G., Cai, L. & Qiu, J. Low frequency torsional vibration gaps in the shaft with locally resonant structures. *Physics Letters A* **348**, 410-415 (2006).
- 44 Xiao, Y. & Wen, J. Closed-form formulas for bandgap estimation and design of metastructures undergoing longitudinal or torsional vibration. *Journal of Sound and Vibration* **485**, 115578 (2020).
- 45 Wu, Z., Liu, W., Li, F. & Zhang, C. Band-gap property of a novel elastic metamaterial beam with X-shaped local resonators. *Mechanical Systems and Signal Processing* **134**, 106357 (2019).
- 46 Cai, C. *et al.* Flexural wave attenuation by metamaterial beam with compliant quasi-zero-stiffness resonators. *Mechanical Systems and Signal Processing* **174**, 109119 (2022).
- 47 Wen, S., Xiong, Y., Hao, S., Li, F. & Zhang, C. Enhanced band-gap properties of an acoustic metamaterial beam with periodically variable cross-sections. *International Journal of Mechanical Sciences* **166**, 105229, doi:<https://doi.org/10.1016/j.ijmecsci.2019.105229> (2020).
- 48 Xu, Z.-L., Wang, Y.-Q., Zhu, R. & Chuang, K.-C. Torsional bandgap switching in metamaterials with compression–torsion interacted origami resonators. *Journal of Applied Physics* **130**, 045105 (2021).
- 49 Wang, Y.-F., Wang, Y.-S. & Laude, V. Wave propagation in two-dimensional viscoelastic metamaterials. *Physical Review B* **92**, 104110 (2015).
- 50 Abdeljaber, O., Avci, O. & Inman, D. J. Optimization of chiral lattice based metastructures for broadband vibration suppression using genetic algorithms. *Journal of Sound and Vibration* **369**, 50-62 (2016).
- 51 Hu, G., Austin, A. C., Sorokin, V. & Tang, L. Metamaterial beam with graded local resonators for broadband vibration suppression. *Mechanical Systems and Signal Processing* **146**, 106982 (2021).
- 52 Banerjee, A. Flexural waves in graded metabeam lattice. *Physics Letters A* **388**, 127057 (2021).

## Abstract in Korean

오그제틱 물질은 음의 푸아송비를 보이는 메타물질의 일종으로, 인장 시 물질의 옆면이 함께 팽창하는 독특한 특성을 보인다. 이러한 특성은 인장 하중에 의해 오그제틱 단위체의 내부 빈 공간이 팽창하는 오그제틱 변형 모드에 의해 발생한다. 그러나 오그제틱 물질이 전단력을 받을 때에는 일반적인 연속체와 유사한 비오그제틱 변형 모드로 변형하게 된다. 우리는 오그제틱 물질의 이러한 하중 의존적 변형 모드에 주목하여 두 기계적 물성을 동시에 조절하기 위한 설계 원리를 제안하였다.

본 연구는 먼저 인장, 전단 강성을 동시에 조절할 수 있는 평면 오그제틱 단위체의 설계 원리를 제시한다. 회전 강체 오그제틱 패턴을 기본 단위체로 설정하여 각각의 변형 모드에서의 강성 조절 메커니즘을 확인하고 이를 설계하기 위한 두 가지 핵심 설계 변수인 힌지두께비 (HR), 세장비 (AR)를 제시하고 조절 원리를 고찰하였다.

평면 상의 강성 조절 설계 원리를 확장하여, 3차원 메타 구조인 오그제틱 메타 튜브, 오그제틱 메타 디스크의 설계 원리를 추가적으로 제시하였다. 오그제틱 메타 튜브는 튜브 구조의 굽힘, 비틀림 강성을 동시에 설계할 수 있는 메타 구조로, 시뮬레이션과 실험을 통해 최소침습수술 기법 중 하나인 동심형 튜브 로봇의 안정성과 성능을 향상시킬 수 있음을 확인하였다. 오그제틱 메타 디스크는 디스크의 굽힘 모드, 비틀림 모드의 고유진동수를 동시에 설계할 수 있는 구조로, 두 종류의 탄성과 전파를 조절하기 위해 설계되었다. 다양한 유한요소 해석 기법을 활용하여 파이프에서의 굽힘, 비틀림 파의 전파를 동시에 조절할 수 있음을 확인하였고, 적용 분야로 탄성과 모드 필터의 예시를 통해 비파괴검사에서의 응용 가능성을 확인하였다.

제안된 설계 원리는 직관적이고 다양한 분야에 적용 가능하다는 데에 의의가 있다. 본 설계 원리는 다양한 기계 특성과 형상에 대한 적용으로 확장될 수 있으며, 이를 통해 새로운 특성과 장치에 대한 설계가 가능해지기를 기대한다.

**주요어:** 메타물질, 오그제틱, 강성, 파동 전파

**학번:** 2015-22727